UNIVERSITY OF SOUTHAMPTON

Phenomenology of Z' bosons and their searches at the LHC Run-II

by

Juri Fiaschi

A thesis submitted in partial fulfilment for the
degree of Doctor of Philosophy

in the
Faculty of Physical Sciences and Engineering
Department of Physics and Astronomy

October 2017

UNIVERSITY OF SOUTHAMPTON

Abstract

Faculty of Physical Sciences and Engineering
Department of Physics and Astronomy

Doctor of Philosophy

by Juri Fiaschi

This thesis investigates the phenomenology of massive neutral spin-1 heavy resonances (Z'-bosons) and their searches at the Large Hadron Collider. In particular the focus here is on the detection of their decay into di-lepton pairs using the ATLAS and CMS detectors in their upgraded setup for the 13 TeV centre of mass energy run (Run-II).

Theoretically motivated models with an extended Electro-Weak sector are introduced and taken as benchmark to test the experimental sensitivity on different observables like the differential cross section, the Forward-Backward Asymmetry and the transverse momentum distribution, and in various phenomenological scenarios, covering the cases of narrow, wide and multiple resonances.

The role of PDF and statistical uncertainties on both signal and background is discussed extensively, including the contribution of photon initiated processes.

“Speech has allowed the communication of ideas
enabling human beings to work together to build the impossible.
Mankind’s greatest achievements have come about by talking.
Our greatest hopes could become reality in the future
with the technology at our disposal, the possibilities are unbounded.
All we need to do is make sure we keep talking.”

Pink Floyd & Stephen W. Hawking

Contents

Abbreviations

SM	**S**tandard **M**odel
GUT	**G**rand **U**nified **T**heory
DM	**D**ark **M**atter
LHC	**L**arge **H**adron **C**ollider
EWSB	**E**lectro-**W**eak **S**ymmetry **B**reaking
EW	**E**lectcro-**W**eak
BSM	**B**eyond **S**tandard **M**odel
DY	**D**rell-**Y**an
BW	**B**reit-**W**igner
(N)NLO	(**N**ext-to-)**N**ext-to-**L**eading **O**rder
QCD	**Q**uantum **C**hromo **D**ynamics
PDF	**P**arton **D**istribution **F**unction
EWPT	**E**lectro-**W**eak **P**recision **T**est
LEP	**L**arge **E**lectron-**P**ositron collider
NWA	**N**arrow **W**idth **A**pproximation
FW	**F**inite **W**idth
CL	**C**onfidence **L**evel
MC	**M**onte-**C**arlo
PI	**P**hoton-**I**nitiated
EPA	**E**quivalent **P**hoton **A**pproximation
DIS	**D**eep **I**nelastic **S**cattering
ED	**E**xtra **D**imension
VEV	**V**acuum **E**xpectation **V**alue
NGB	**N**anbu-**G**oldstone **B**oson
BR	**B**ranching **R**atio

Declaration of Authorship

I, JURI FIASCHI, declare that this thesis titled, 'Phenomenology of Z' bosons and their searches at the LHC Run-II' and the work presented in it are my own. I confirm that:

- This work was done wholly or mainly while in candidature for a research degree at this University.
- Where any part of this thesis has previously been submitted for a degree or any other qualification at this University or any other institution, this has been clearly stated.
- Where I have consulted the published work of others, this is always clearly attributed.
- Where I have quoted from the work of others, the source is always given. With the exception of such quotations, this thesis is entirely my own work.
- I have acknowledged all main sources of help.
- Where the thesis is based on work done by myself jointly with others, I have made clear exactly what was done by others and what I have contributed myself.
- parts of this work have been published as: [1], [2], [3] and [4].

Signed: ________________________________

Date: ________________________________

Acknowledgements

First, I would like to thank my supervisors, Stefano Moretti for the professional growth he has inspired me with and for guiding my doctorate to a fruitful end; and Claire Shepherd-Themistocleous for sharing her expertise and for the enlightening hints she has provided along the years.

A heartfelt thank to Elena Accomando for her dedication she has putted in following all my projects and the invaluable knowledge she has transmitted to me. Many thanks to Francesco Hautmann for the precious comments and advises provided in our collaborations. I am also very grateful to Alexander Belyaev for the many proficuous discussions, and to all the SHEP group for the welcome they have given me and for making me always feel at home.

I am very fortunate to have found a special group of colleagues, in particular Daniele Barducci, Marc Thomas, Declan Millar, Peter Jones, Zoë Slade, Fredrik Björkeroth, Emine Yildirim, Hugo Prager, Dermot O'Brien, who have shared this journey and memorable experiences with me.

A really special mention is for two most awesome mates I could ever find, Miguel Romao and Georgios Dimitriadis, who have who gained my eternal respect as brilliant colleagues and my true friendship as incredible persons.

Finally, I would like to thank my family and all my friends for the unconditioned love and support I have always received. Thanks to them my life could not have been any better.

Chapter 1

Introduction

1.1 The Standard Model and beyond

The great success of particle physics is the unified description of three fundamental forces of Nature: the electromagnetic, the weak and the strong interactions between elementary particles. The fermions, elementary particles that compose the matter, and the bosons, the mediators of the three interactions, are well organized in a very elegant picture that is the Standard Model (SM). Within the SM framework it is possible to compute predictions for any observable that can be measured in an experiment. Exploiting the perturbative expansion technique, in principle it is possible to reach any desired level of accuracy. Practically as the perturbative expansion order grows, the technical difficulty of the calculations rapidly diverges, such that at the current state of art in high order calculations, it is generally not possible to go beyond 2-loop expansion (only for a very limited class of processes it is possible to calculate a 3-loops expansion). Nevertheless, the accordance between theoretical calculations and experimental measurements is impressive and spans a very large variety of elementary processes and several orders of energy scale magnitude.

The challenge of modern physics is to expand further our knowledge of the fundamental laws of nature, toward the direction of a Grand Unified Theory (GUT) that will provide an unified description of all the forces in nature, thus including gravity with the electroweak and strong interactions, which will be valid at any energy scale. There are indeed many experimental and theoretical reasons that lead physicists to think that there is something lying beyond the SM. From the theoretical point of view, the naturalness argument suggest that the SM is actually an effective theory valid up to a certain scale. Even more solid experimental evidences, such as neutrino oscillations and Dark Matter (DM), that cannot be accommodated in the SM, require an extension of the SM picture.

The Large Hadron Collider (LHC) is the most powerful machine ever built in the history of mankind with the purpose of probing the fundamental laws of nature at very high energy scale. The hope of the scientific community is that the proton-proton collisions occurring at unprecedented rate and centre of mass (c.o.m.) energies will produce signals of new physics, that will be detected in one or more of the experiments installed across the machine.

The Run-I of the LHC, performed at 7 and 8 TeV of c.o.m. energy, concluded with the discovery of the last missing piece of the SM, that is the elusive Higgs boson. Detecting the existence of this unique component of the SM was indeed crucial. On top of being the sole fundamental spin-0 particle, its importance lies on its key role in the spontaneous Electro-Weak Symmetry Breaking (EWSB) mechanism, that is at the base of the Electro-Weak (EW) theory.

After a short shut down, the LHC has restarted its program with an upgraded c.o.m. energy of 13 TeV. The ongoing Run-II has the potential to surpass the barrier of our knowledge represented by the SM description of elementary physics. The CMS and ATLAS experiments in particular have been designed to reach the maximum possible level of sensitivity to high energy processes, and are currently probing the few TeV invariant mass region. The aforementioned arguments and evidences have inspired several Beyond Standard Model (BSM) theories that indeed indicate the TeV threshold as the energy scale where new physics might naturally appear.

In this picture the Run-II era has been long awaited as the probable next turning point in the quest for BSM physics. For this reason the preliminary phenomenological study of possible signatures of new physics is mandatory and will ideally contribute to an eventual experimental discovery.

1.2 New physics in the di-lepton channel

A very common prediction appearing in several BSM theories is the existence of new heavy spin-1 neutral resonances, usually called Z's. The enlarged symmetry groups of GUT theories indeed generally allow new neutral resonances [5]. This is the case of string theory motivated E6 and Left-Right (GLR) symmetric models, where the Z' is associated to an extra $U(1)'$ gauge symmetry which can be broken at the TeV scale. Multiple heavy Z's also arise from Kaluza-Klein compactifications in ED inspired models [6, 7], or from composite constructions in strong interacting models [8–10]. Also in these two approaches if the compactification or the compositeness scales respectively are at the TeV scale, the associated Z' boson can be observed at the LHC.

The data collected during the Run-I and Run-II by the ATLAS and CMS collaborations is used to set constrains on the parameter space of these popular models, and consequently to raise the Z' lower mass bounds. In this prospective, the forthcoming data from the LHC might contain the first signal of BSM physics. An accurate analysis of any deviation from the SM predictions is mandatory to disentangle a new physics signal.

Being a neutral colourless boson, a Z' can be produced only though a quark-antiquark interaction, thus there is no dependence on the CKM matrix entries in the relative matrix element. The most sensitive experimental searches are performed looking at its decay in the di-lepton channel. This pattern of production and decay is the Drell-Yan (DY) process and is the golden channel for probing new physics in the neutral sector.

The detectors of ATLAS and CMS indeed show extremely good performances in the detection and measurements of charged leptons kinematic quantities. The fiducial cross sections measured by the experimental collaborations, usually covers the leptons parameter space with $|\eta| < 2.5$ and $p_T > 20$ GeV [11]. More recent measurements analysis done from the CSM collaboration, have extended the coverage in the high rapidity region $2.5 < |\eta| < 5$, even if just in the electron channel [12].

As mentioned, the efficiencies of the lepton channels are very well understood. CMS provides precise values for the efficiencies of both electron and muon channels as function of the di-lepton invariant mass [11]. Those values have been released for the Run-I at 8 TeV, but since no sensible variations are expected for the Run-II, in the results obtained in this work, these factors have been adopted independently on the c.o.m. energy. The muon channel presents a slight better efficiency then the electron channel, thus in general it is important to accumulate statistics for the off-line analysis. The electron channel instead features a better resolution than the muon channel ($\sim 1.2\%$ and $\sim 3\%$ of the invariant mass respectively). This will be a very important feature for the interpretation of the signal shape in likelihood fits. However for some phenomenological scenarios might require extra caution with this respect. In some cases, i.e. when in presence of very narrow resonances or very strong interference effects, the finite experimental resolution and the related Gaussian smearing of the signal, might have important consequences in the interpretation of a experimental analysis. Some of these issues will be discussed more in details in Chapter 5.

The presence of a Z' signal in the invariant mass spectrum is expected to assume the shape of a Breit-Wigner (BW) distribution on a flat smooth background. Experimental searches for these heavy objects are performed in the very high invariant mass region, where generally no SM events are expected. The distribution of di-lepton events generated by a Z' decay would appear as a “bump” in the tail of the invariant mass spectrum. This kind of signal is associated to narrow Z' resonances, which is the most common scenario that is expected to appear. Experimental analysis indeed have been optimised to have the best sensitivity to this kind of signal. As will be discussed in Chapter 2, specific procedures have been developed to perform model independent interpretation of the experimental exclusions, such that for a given BSM model predicting a narrow resonance it is often straightforward to extract bounds on the hypothetical Z' mass [13, 14]. In this context of few signal events in almost null background, statistical arguments suggest the use of Poisson statistics to compute the significance of a BSM signal [15, 16]. Under these hypothesis, the following approximated formula for the computation of the significance α of signals arising from narrow resonances will be adopted:

$$\alpha_P = 2\left(\sqrt{S+B} - \sqrt{B}\right) \tag{1.1}$$

where S and B represent the number of BSM signal and SM background expected events at a given luminosity respectively.

The other scenario that will be discussed in this work, concerns the possibility of dealing with broad resonances. There are many theoretically motivated frameworks (strong interacting models, contact interactions etc.) where a BSM signal in the di-lepton channel displays a non-resonant structure. The experimental detection of these objects is more challenging and they often require dedicated analysis. They would indeed appear not anymore as a visible "bump", but instead as a shoulder or a departure from the SM smooth falling curve. A model-independent approach for revealing the BSM signal relies on the "counting" strategy. This procedure is performed applying a variable low invariant mass cut on the data sample and moving this cut along the spectrum, in order to detect an excess of events with respect to the SM expectations. The tail of the SM spectrum in the high invariant mass region, where no events are experimentally detected, is obtained fitting a specific functional form for masses above 400 GeV in the so called "control region", which is supposed to be new physics free [17]. This assumption is not always immune of caveats, such that some caution is required when interpreting this kind of experimental analysis.

The case of broad resonances, which reproduces also the effectively non-resonant case, will be discussed more in details in Chapter 2, and the significance associated to the excess in "counting" analysis will be assumed to follow the Gaussian statistics:

$$\alpha_G = \frac{S}{\sqrt{S+B}} \tag{1.2}$$

where again S and B represent the number of BSM signal and SM background expected events as a given luminosity respectively. The significances obtained using the number of events collected in the di-electron and di-muon channels can be combined together to improve the overall sensitivity to new physics. Being independent events, their significances can be combined using:

$$\alpha_{tot} = \frac{\alpha_{P(G),e} + \alpha_{P(G),\mu}}{\sqrt{2}} \tag{1.3}$$

Another necessary ingredient for calculating correctly SM and BSM predictions are the higher order radiative corrections. The DY channel has been studied in details and currently perturbative corrections are available up to Next-to-Next-to-Leading Order (NNLO) in the Quantum Chromo Dynamics (QCD) strong coupling (α_S) expansion [18]. In the following of this work, when calculating the significances and the predictions for the expected number of events, it has been used a k-factor obtained with the WZPROD code evaluating the QCD NNLO corrections at different invariant mass points [19, 20]. At this level of precision, first order EW corrections should as well be included. The effects of the EW interactions in DY processes at the LHC will be discussed more in details in Chapter 3.

The sensitivity of high invariant mass searches is generally determined by the accumulated statistics. In this mass region, where only few background events are expected, the detection of an excess is interpreted evaluating the significance of that signal as described above. A signal with a significance $\alpha_{tot} \sim 5$ (corresponding to a 5σ deviation from the background expectations) is considered in all respect a strong evidence of new physics: this is the required level of accuracy to claim the discovery of a new particle. On the other hand, in order to exclude a particular realisation of a neutral resonance decaying into two leptons, it is sufficient to estimate a significance below $\alpha_{tot} \sim 2$ (i.e. a 2σ deviation from the expected background): any signal below this threshold is indeed classified as a statistical fluctuation. The LHC programme is aiming to collect as much data as possible in the next years. The increase of integrated luminosity ($\mathcal{L}$) along this period is directly related to the expected number of events by $N = \mathcal{L}\,\sigma(p\bar{p} \to \ell^+\ell^- + X)$. Following the approach described above, it is possible to estimate exclusion and discovery limits as function of the collected integrated luminosity, and this is one of the final goal of any phenomenological study.

As the integrated luminosity grows, also the sensitivity to possible new physics signals increases consequently to the reduction of the statistical uncertainty of the data. In the high luminosity stage, when diagnostic analysis and precision measurements are performed, systematic effects are also to be included since they can be sizeable. The main source of systematic uncertainty in hadron collisions (proton-proton collisions in this case) is represented by the determination of the behaviour of their fundamental components. The kinematic properties of the partons inside the protons are described by the Parton Distribution Functions (PDFs), which parametrise the partons strong dynamics effects below the factorisation scale, that are not computable due to the breakdown of perturbation theory. A more extensive discussion on the parton PDFs and on the procedures to extract their systematic uncertainties will be given in Chapter 2 for the usual DY di-lepton final state, following the work presented in [1, 21–23], and in Chapter 3 for the photon initiated di-lepton production, following the work presented in [3, 4, 24, 25].

The great sensitivity on possible new physics signals that is achieved in the di-lepton channel reflects the remarkable work that has been done by the experimental groups in collaboration with the theory departments. From the theory side, new ideas are continuously emerging and require new phenomenological studies. The experimental analysis are steadily challenged in this evolving scenario and often the formalisation of new procedures is required to improve the sensitivity of those analysis. This work will discuss some non traditional scenarios, which depart from the usual single narrow Z' resonance framework. In Chapter 2 will be considered the phenomenology of wide resonances and will be discussed the potential of the AFB observable in this context. In Chapter 4 a new observable will be introduced, the AFP, to improve the discovery and interpretative potential on broad resonances through leptons transverse momentum measurements, following the work presented in [26]. In Chapter 5 will be explored the phenomenology of two benchmarks models that feature a multiple resonant spectrum in their neutral sector, following the work presented in [2, 27]. They will be the NUED model and the 4DCHM and the phenomenological scenarios obtained spanning their parameter space will cover a large variety of possibilities and will offer several experimental challenges.

Chapter 2

Single Z'-bosons

2.1 Model Independent parametrization

Following the formalism of [5], single Z' models can be described simply adding an extra $U(1)'$ symmetry to the SM gauge group:

$$SU(3)_C \times SU(2)_L \times U(1)_Y \times U(1)' \tag{2.1}$$

The new gauge group is broken at the TeV scale, in order to generate a mass to the associated Z'-boson. The specific symmetry breaking pattern defines the specific Z' interactions (couplings) with the SM matter. Being as general as possible, the Lagrangian is parametrised using a minimal set of parameters. The effective interactions can be written in the general form:

$$\mathcal{L}_{NC} = \frac{g'}{2} Z'_\mu \bar{f} \gamma^\mu \left(g_V^f - g_A^f \gamma^5 \right) f \tag{2.2}$$

where $g_{V,A}^f$ are the vector and axial couplings between the Z' and the fermions, after an overall gauge coupling g' is factorised out. They are related to the left and right couplings $\epsilon_{L,R}$ by the relation: $g_{V,A}^f = \epsilon_L^f \pm \epsilon_R^f$. Assuming universality amongst the three families of quarks and leptons ($g_{V,A}^u = g_{V,A}^c = g_{V,A}^t$; $g_{V,A}^d = g_{V,A}^s = g_{V,A}^b$; $g_{V,A}^e = g_{V,A}^\mu = g_{V,A}^\tau$; $g_{V,A}^{\nu_e} = g_{V,A}^{\nu_\mu} = g_{V,A}^{\nu_\tau}$), and assuming possible right handed neutrinos to be heavier than the Z' boson, the interaction is specified by eight model dependent couplings. Those parameters are not completely independent since the left-handed fermions are represented by a doublet of $SU(2)$, thus they have the same charge ($\epsilon_L^u = \epsilon_L^d$; $\epsilon_L^\ell = \epsilon_L^\nu$), leaving just five independent couplings.

The symmetry breaking occurring to give mass to the associated Z' is responsible for the specific values of the couplings. An exhaustive description of the couplings structure and parametrisation of the single Z' models that will be used in the following is available in [28]; some details are reported in Appendix A.

It is possible that the Z' mixes with the SM neutral mass eigenstate represented by the Z-boson. However there are strong constrains on this mixing coming from the analysis of high precision measurements performed at the Large Electron-Positron collider (LEP) [29, 30]. Electro-Weak Precision Tests (EWPTs) set an upper bound of the mixing angle between the neutral bosons mass eigenstates: $\alpha \lesssim 10^{-3}$ [31, 32]. For the present, corrections to the couplings of this order will be considered small and not included in the first place.

In this minimal description, there is no extra matter to the SM content, thus the width of the Z' resonance is fixed by its couplings to the fermions which will be assumed massless, following the relation:

$$\Gamma_{Z'} = \frac{g'}{48\pi} M_{Z'} \left[9({g_V^u}^2 + {g_A^u}^2) + 9({g_V^d}^2 + {g_A^d}^2) + 3({g_V^e}^2 + {g_A^e}^2) + 3({g_V^\nu}^2 + {g_A^\nu}^2) \right] \tag{2.3}$$

Each one of the single Z' models is characterised by his natural value for the width, obtained following the above formula and plugging in the specific Z' couplings. Natural values for the resonances width over mass ratios are given in table A.2 at the end of Appendix A, and they are generally of the order of few percent of the Z' mass ($\Gamma_{Z'}/M_{Z'} \sim 0.5 - 4\%$), except for the GSM-Q model where the resonance can be as large as $\Gamma_{Z'}/M_{Z'} \simeq 12\%$.

Resonances with this profile are to be considered narrow, and model independent approaches can be used to interpret the data. Using the Narrow Width Approximation (NWA) the experimental excluded cross section can be interpreted directly as lower exclusion bounds for the corresponding Z' masses within each model [1, 21–23]. Another approach that maximise the sensitivity to the signal is described in [13, 14] and consist on fixing an invariant mass window around the Z' peak to integrate the signal. This "optimal" cut in the invariant mass of the di-lepton pair is taken to be $|M_{l\bar{l}} - M_{Z'}| \leq 0.05 \times E_{\text{coll}}$ where E_{coll} is the collider energy. This cut was designed so that the error in neglecting the (model-dependent) Finite Width (FW) and interference effects (between γ, Z, Z') is kept below $O(10\%)$ for all models and for the full range of allowed Z' masses under study, following the recommendations of [13, 14]. CMS has adopted this prescription to interface experimentally excluded cross sections and model independent mass limits on single Z' models [11].

The experimental limits have been reproduced here for the thirteen benchmark models predicting a Z'-boson characterized by a narrow width ($\Gamma_{Z'}/M_{Z'} \leq 5\%$) summarized in Appendix A, and the limits on $M_{Z'}$ have been extracted by making use of the 95% Confidence Level (CL) upper bound on the Z'-boson production cross section in DY, $\sigma(pp \to Z' \to e^+e^-, \mu^+\mu^-)$. In order to reduce systematic uncertainties, the experimental analysis normalizes the Z'-boson production cross section in DY to the SM Z-boson cross section on peak. As shown in Fig. 2.1, the 95% CL upper bound is indeed given on the ratio $R_\sigma = \sigma(pp \to Z' \to e^+e^-, \mu^+\mu^-)/\sigma(pp \to Z, \gamma \to e^+e^-, \mu^+\mu^-)$. The use of this ratio R_σ in fact cancels the uncertainty in the integrated luminosity and reduces the dependence on the experimental acceptance and trigger efficiency.

The ratio R_σ is calculated at the NNLO in QCD using the WZPROD program [19, 33] (which has been adapted for Z' models and new PDF sets [28]) and the CTEQ6 package [34]. Similar computations have been performed in Ref. [35], albeit within a different kinematical setup. There, the R_σ ratio is evaluated at NLO+NLL using RESUMMINO. The NNLO QCD contributions give rise to a K-factor which depends on the energy scale; this dependence is here fully taken into account. The NNLO prediction for the SM Z, γ production cross section, $\sigma(pp \to Z, \gamma \to l^+l^-)$ with $l = e, \mu$, in the mass window of 60 to 120 GeV is 1.117 nb. Using all these ingredients at hand, the R_σ ratio is computed as a function of the mass of the new heavy Z'-boson, $M_{Z'}$, and the corresponding limits are derived for all benchmark models, combining the significances obtained in the di-electron and di-muon channels. Fig. 2.1(a) shows the bounds on all E6 models, while Fig. 2.1(b) displays the results for the remaining two classes of models, GLR and GSM. As previously mentioned, traditional experimental analyses work under the hypothesis that the signal has a BW line shape and that the analysis is performed in a restricted search window around the hypothetical mass of the Z'-boson. This approach is theoretically motivated by the benchmark models, all predicting a narrow width Z'-boson, and by the will to define a model independent procedure.

In order to extract limits on the mass of extra Z'-bosons, the total theoretical cross section is computed in the di-lepton invariant mass interval around the peak given by the "optimal" cut and then crossed with the 95% CL upper bound on the BSM cross section derived from the experimental data analysis.

The first characterising element of this analysis is that it assumes a generic shape for the signal, that is a BW convoluted with a Gaussian resolution function.

Low mass tails, due to PDF's and model dependent effects like FW and interference of the extra Z' boson with the SM γ and Z, are not considered. The analysis is, by design, not sensitive to potential tails of the signal and the magnitude of such tails is much less than the SM background. Attempting to make the experiment sensitive to the tails would render the analysis model dependent, thereby automatically restricting the coverage of theoretical models where one could extract mass bounds in a consistent way. The CMS approach consists thus in modelling the signal via a function which is common to a large class of models predicting a single, rather narrow, Z'-boson. This generic signal-shape (a BW normalized to the total cross section computed in NWA) closely resembles the exact result where both FW and interference effects are accounted for. This result is common to a large class of narrow single Z'-boson scenarios, as extensively discussed in Ref. [13]. As to the SM background, the CMS collaboration represents its shape by a functional form whose parameters are fixed via a fit to the Monte-Carlo (MC) SM background estimate, and its rate is normalised to the data. The normalization of the SM background is performed in a window of the di-lepton spectrum taken around the hypothetical Z'-boson pole mass.

Having the functional forms for the Z'-boson signal and the SM background, an extended unbinned likelihood function for the spectrum of di-lepton invariant masses is then constructed. If no evidence for BSM physics is observed, the 95% CL upper bound on the cross section is derived. This result can then be used to extract limits on the Z' boson parameters, i.e., mass and possibly couplings, from a number of new physics models. However, a key point is that, in order to perform a consistent interpretation of the data, the theoretical cross section within any given model must be computed by minimising the model-dependent effects as well. This is indeed the role of the integration range $|M_{l\bar{l}} - M_{Z'}| \leq 0.05 \times E_{\text{coll}}$ advocated in Ref. [13] for computing the total cross section in any given model, keeping FW and interference effects below $O(10\%)$.

The notable outcome of this procedure is that the theoretical cross sections of the Z' bosons predicted within a variety of models belonging to the E6, GLR and GSM classes of theories can all directly be compared with the 95% CL upper bound on the Z'-boson cross section resulting from the experimental analysis performed by the CMS collaboration. In definitive it allows the extraction of exclusion bounds on the mass of the various Z' bosons at once, without requiring dedicated analyses.

Fully exploiting the data set collected at the LHC during the 8 TeV run (roughly 20 fb^{-1} of integrated luminosity), the single-Z' model masses are thus constrained to be heavier than 2.5 TeV, as visible in Fig. 2.1, and as reported explicitly in Table 2.1.

Adopting the same prescription, it is possible to evaluate the significance of the Z' signal, as function of the Z' mass and the experiment luminosity. Limits for the Run-II energy at 13 TeV as function of the luminosity can be extrapolated for exclusion and discovery bounds, requiring respectively a significance of 2σ or 5σ. The resulting mass limits are set between 5 and 7 TeV for the exclusion, and between 4.5 and 6 TeV for a discovery, assuming an integrated luminosity of 300 fb^{-1}, as visible in Fig. 2.2 and

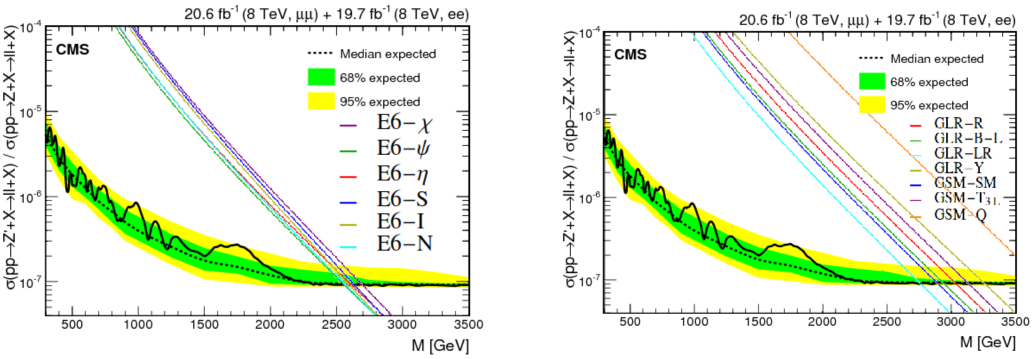

(a) (b)

FIGURE 2.1: (Colour online) (a) 95% CL upper bound on the Z'-boson production cross section in DY normalized to the SM cross section on the Z-boson peak: $R_\sigma = \sigma(pp \to Z' \to l^+l^-)/\sigma(pp \to Z, \gamma \to l^+l^-)$ with $l = e, \mu$. The combined analysis of the di-muon and di-electron channels has been produced by the CMS collaboration with a data sample collected at the 8 TeV LHC, corresponding to an integrated luminosity of 20.6 and 19.7 fb^{-1} respectively [11]. Theoretical predictions for the class of the E6 models are superimposed to extract the corresponding Z'-boson mass limits. As described in the text, in order to match theoretical predictions and experimental results, the optimal cut on the invariant mass of the di-lepton pairs has been implemented: $\Delta M = |M_{ll} - M_{Z'}| \leq 0.05 \ \ E_{\text{coll}}$ for $E_{\text{coll}} = 8$ TeV. (b) Same as (a) for the other two classes of GSM and GLR models.

Class	E6					
$U'(1)$ Models	χ	ϕ	η	S	I	N
$M_{Z'}$ [GeV]	2700	2560	2620	2640	2600	2570

Class	GLR				GSM		
$U'(1)$ Models	R	B-L	LR	Y	SSM	T_{3L}	Q
$M_{Z'}$ [GeV]	3040	2950	2765	3260	2900	3135	3720

TABLE 2.1: Bounds on the Z'-boson mass derived from the latest direct searches performed by CMS at the 8 TeV LHC with integrated luminosity $\mathcal{L} = 20$ fb^{-1}. Here are considered thirteen different models with an extra $U'(1)$ gauge group predicting a new heavy neutral boson characterized by a narrow width. From left to right, the columns indicate the $M_{Z'}$ limit in GeV within the E6, GLR and GSM class of models.

Fig. 2.3. The explicit values for both discovery and exclusion mass limits within each model are reported in Table 2.2.

Up to date experimental bounds on narrow (i.e., where $\Gamma_{Z'}/M_{Z'} \sim 1\%$) Z' resonances have been released from CMS [36] and ATLAS [37] with the Run-II energy of 13 TeV and an integrated luminosity of 13 fb^{-1} and 36.1 fb^{-1} respectively. The most stringent bounds set the limit for the masses of these objects $M_{Z'} > 4$ TeV. The exclusion projections shown in Fig. 2.2 closely follow the recent experimental results, confirming that the procedure described above for computing the aforementioned bounds closely follows the experimental analysis.

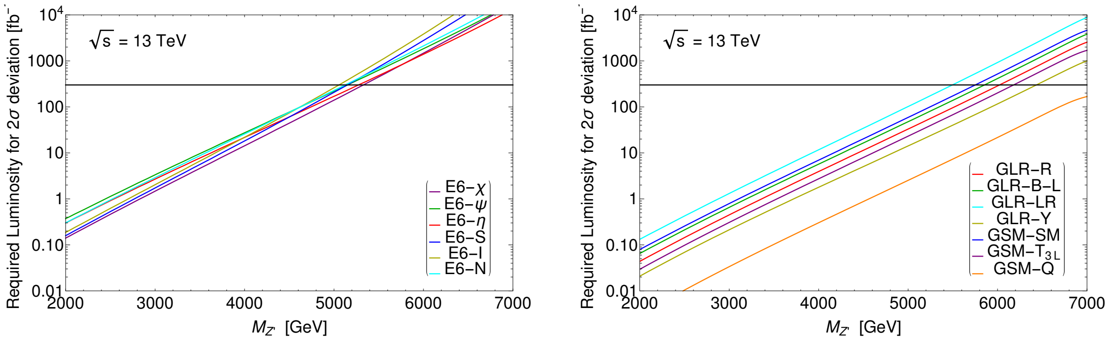

(a) (b)

FIGURE 2.2: (Colour online) (a) Exclusion potential of the 13 TeV LHC for the E6 class of models. The 2σ contours are plotted as a function of Z'-boson mass and luminosity. A combined analysis is performed over e^+e^- and $\mu^+\mu^-$ pairs and the $A \times \epsilon$ factor given by CMS [11] at the 8 TeV LHC are assumed. (b) Same for the GSM and GLR classes of models.

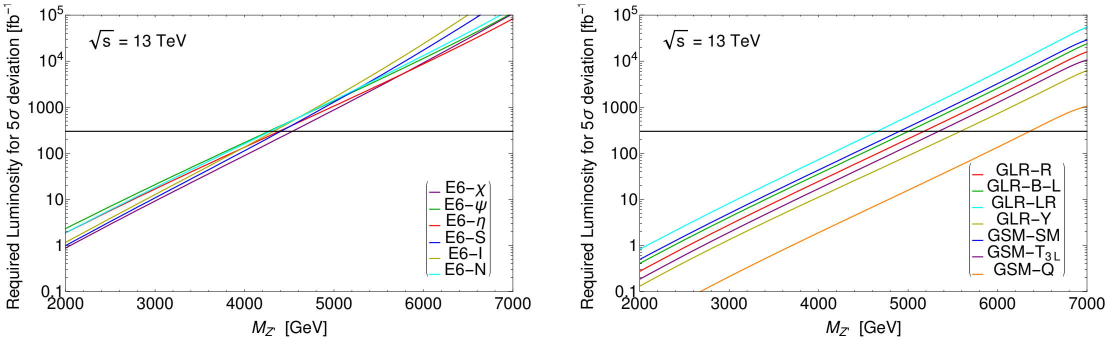

(a) (b)

FIGURE 2.3: (Colour online) (a) Discovery potential of the 13 TeV LHC for the E6 class of models. The 5σ contours are plotted as a function of Z'-boson mass and luminosity. A combined analysis is performed over e^+e^- and $\mu^+\mu^-$ pairs and the $A \times \epsilon$ factor given by CMS [11] at the 8 TeV LHC are assumed. (b) Same for the GSM and GLR classes of models.

2.2 The Forward-Backward Asymmetry

In this section, the Forward-Backward Asymmetry ($A_{\rm FB}$) is defined and its role in Z'-boson searches and in the interpretation of an observed resonance is discussed. In the literature, the $A_{\rm FB}$ has been long exploited to help disentangle the various theories predicting an extra heavy neutral boson and tracing back the Lagrangian parameters (see, for example, [38–40] and references therein). This is not an easy task and the sensitivity of $A_{\rm FB}$ measurements to new physics like additional Z'-bosons has therefore received a lot of attention in the past years. For DY processes, $A_{\rm FB}$ is defined from the angular distribution:

Class	E6					
$U'(1)$ Models	χ	ϕ	η	S	I	N
$M_{Z'}$ [GeV]	4535	4270	4385	4405	4325	4290
$M_{Z'}$ [GeV]	5330	5150	5275	5150	5055	5125

Class	GLR				GSM		
$U'(1)$ Models	R	B-L	LR	Y	SSM	T_{3L}	Q
$M_{Z'}$ [GeV]	5175	5005	4655	5585	4950	5340	6360
$M_{Z'}$ [GeV]	6020	5855	5495	6435	5750	6180	8835

TABLE 2.2: Projection of discovery limits (first row) and exclusion limits (second row) on the Z'-boson mass from direct searches at the forthcoming Run-II of the LHC at 13 TeV. The designed value for the integrated luminosity is assumed: $\mathcal{L} = 300$ fb^{-1}. Here are considered thirteen different models with an extra $U'(1)$ gauge group predicting a new heavy neutral boson characterized by a narrow width. From left to right, the columns indicate the $M_{Z'}$ limit in GeV within the E6, GLR and GSM class of models.

$$\frac{d\sigma}{d\cos\theta_l} \propto \frac{1}{4\cdot 3} \sum_{\text{spin, col}} \left| \sum_i \mathcal{M}_i \right|^2 = \frac{\hat{s}^2}{12} \sum_{i,j} P_i^* P_j [(1+\cos^2\theta_l) C_S^{ij} + 2\cos\theta_l C_A^{ij}] \tag{2.4}$$

where θ_l is the lepton angle with respect to the quark direction in the di-lepton centre-of-mass frame, which can be derived from the measured four-momenta of the di-lepton system in the laboratory frame. The A_{FB} is indeed given by the coefficient of the contribution to the angular distribution linear in $\cos\theta_l$. In Eq. (2.4), $\sqrt{\hat{s}}$ is the invariant mass of the di-lepton system, and P_i and P_j are the propagators of the gauge bosons involved in the process. At tree-level, the DY production of charged lepton pairs is mediated by three gauge bosons: the SM photon and Z-boson and the hypothetical Z'-boson. These three vector boson exchanges all participate in the matrix element squared:

$$P_{ij} \equiv \text{Re}[P_i^* P_j] = \frac{(\hat{s}-M_i^2)(\hat{s}-M_j^2) + M_i\Gamma_i M_j\Gamma_j}{\left((\hat{s}-M_i^2)^2 + M_i^2\Gamma_i^2\right)\left((\hat{s}-M_j^2)^2 + M_j^2\Gamma_j^2\right)} \tag{2.5}$$

where M_i and Γ_i are the mass and width of the gauge bosons involved and $i,j = \{\gamma, Z, Z'\}$. Finally, the factors C_S^{ij} and C_A^{ij} in the angular distribution given in Eq. (2.4) are coefficients which are functions of the chiral quark and lepton couplings, $q^i_{L/R}$ and $e^i_{L/R}$, to the i-boson with $i = \{\gamma, Z, Z'\}$:

$$C_S^{ij} = (q_L^i q_L^j + q_R^i q_R^j)(e_L^i e_L^j + e_R^i e_R^j), \tag{2.6}$$
$$C_A^{ij} = (q_L^i q_L^j - q_R^i q_R^j)(e_L^i e_L^j - e_R^i e_R^j). \tag{2.7}$$

One can conveniently compute the forward (F) and backward (B) contributions to the total cross section integrating over opposite halves of the angular phase space:

$$d\hat{\sigma}_F = \int_0^1 \frac{d\hat{\sigma}}{d\cos\theta_l} d\cos\theta_l = \frac{\hat{s}}{192\pi} \sum_{i,j\geq i} \frac{P_{ij}}{1+\delta_{ij}} \left(\frac{4}{3} C_S^{ij} + C_A^{ij}\right), \tag{2.8}$$
$$d\hat{\sigma}_B = \int_{-1}^0 \frac{d\hat{\sigma}}{d\cos\theta_l} d\cos\theta_l = \frac{\hat{s}}{192\pi} \sum_{i,j\geq i} \frac{P_{ij}}{1+\delta_{ij}} \left(\frac{4}{3} C_S^{ij} - C_A^{ij}\right), \tag{2.9}$$

where i and j sum over the mediating resonances, $\{\gamma, Z, Z'\}$.

From the above expressions one can immediately see that the total cross section, $\sigma = \sigma_F + \sigma_B$, depends uniquely on the parity symmetric coefficient C_S. Conversely, the difference between forward and backward cross sections, $\sigma_F - \sigma_B$, preserves only the contribution proportional to the parity antisymmetric coefficient C_A. This is the term which is related to the A_{FB}. One can thus define the A_{FB} as the difference between forward and backward cross sections normalized to the total cross section:

$$\begin{gathered} \hat{\sigma} = d\hat{\sigma}_F + d\hat{\sigma}_B = \frac{\hat{s}}{72\pi} \sum_{i,j\geq i} \frac{P_{ij}}{1+\delta_{ij}} C_S^{ij}, \\ A_{FB} = \frac{d\hat{\sigma}_F - d\hat{\sigma}_B}{d\hat{\sigma}_F + d\hat{\sigma}_B} = \frac{\hat{s}}{96\pi\hat{\sigma}} \sum_{i,j\geq i} \frac{P_{ij}}{1+\delta_{ij}} C_A^{ij}. \end{gathered} \tag{2.10}$$

with the SM background corresponding to $ij = \gamma\gamma, ZZ, \gamma Z$ and the new physics given by $ij = \gamma Z', ZZ', Z'Z'$. In the light of the above discussion, the total cross section and A_{FB} depend on different combinations of Z'-boson couplings to ordinary matter. For that reason, the A_{FB} can give complementary information about the structure of such couplings when compared to the total cross section. This feature has motivated several authors to study the potential of the A_{FB} observable in interpreting a possible Z'-boson discovery obtained in the usual resonance hunt as in Ref. [38, 39, 41, 42]. On top of interpretation purposes, the A_{FB} can also be a powerful tool to search for new physics.

2.2.1 The reconstructed A_{FB}

The A_{FB} is obtained by integrating the lepton angular distribution forward and backward with respect to the quark direction. As in *pp* collisions the original quark direction is not known, one has to extract it from the kinematics of the di-lepton system. This analysis follows the criteria of Ref. [43] where the quark direction is inferred from the boost of the di-lepton system with respect to the beam axis (z-axis). This strategy is motivated by the fact that at the *pp* LHC the di-lepton events at high invariant mass come from the annihilation of either valence quarks with sea antiquarks or sea quarks with sea antiquarks. As the valence quarks carry away, on average, a much larger fraction of the proton momentum than the sea antiquarks, the boost direction of the di-lepton system should give a good approximation of the quark direction. A leptonic Forward-Backward asymmetry can thus be defined with respect to the boost direction. In contrast, the subleading number of di-lepton events which originate from the annihilation of quark-antiquark pairs from the sea must be symmetric.

A measure of the boost is define through the di-lepton rapidity:

$$y_{l\bar{l}} = \frac{1}{2}\ln\left[\frac{\mathrm{E}+\mathrm{P_z}}{\mathrm{E}-\mathrm{P_z}}\right] \tag{2.11}$$

where E and P_z are the energy and the longitudinal momentum of the di-lepton system, respectively. The quark direction is identified by the sign of $y_{l\bar{l}}$. In this way, one can define the reconstructed forward-backward asymmetry, from now on called A^*_{FB}. Namely the A^*_{FB} is defined using the θ^*_l reconstructed angle, which is the angle between the final state lepton and the incoming quark direction in the centre-of-mass of the di-lepton system. As the A_{FB} reconstruction procedure relies on the correlation between the boost variable, $y_{l\bar{l}}$, and the direction of the incoming valence quark, it is therefore more likely to pick up the true direction of the quark for higher values of $y_{l\bar{l}}$. Increasing the probability of identifying the direction of the quark would lead to an observed value of A^*_{FB} that is closer to the ‘true’ value of A_{FB} if one were able to access the partonic CM frame. The trade-off occurs in the reduction of statistics which impacts the significances the other way. The general definition of significance S between predictions of an observable O with uncertainty δO from two hypotheses is

$$S = \frac{|O_1 - O_2|}{\sqrt{\delta O_1^2 + \delta O_2^2}} \tag{2.12}$$

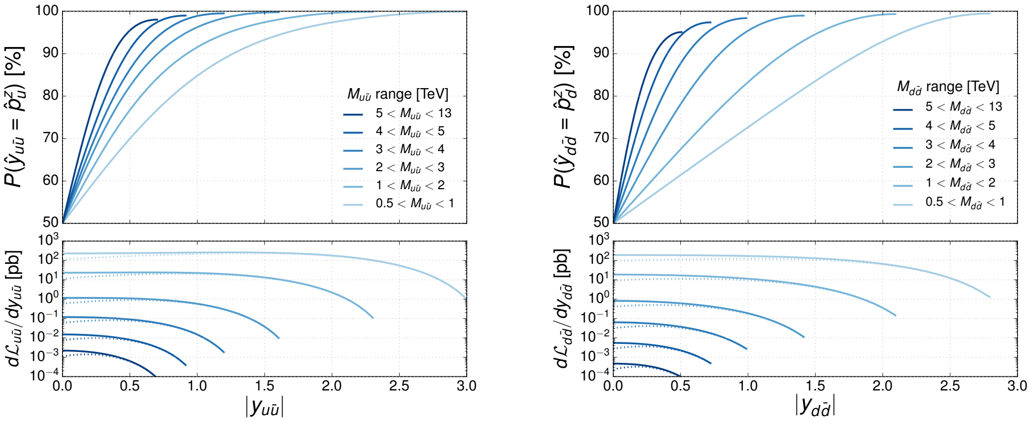

(a) (b)

FIGURE 2.4: (Colour online) (a)Upper plot: Probability of getting the correct direction of the valence up-quark at the 13 TeV LHC via the boost direction of the di-lepton system, given by the sign of the di-lepton rapidity $y_{l\bar{l}}$, as a function of the modulus $|y_{l\bar{l}}| = |y_{u\bar{u}}|$ for six different invariant mass windows scanning from 500 GeV to 5000 GeV and beyond. Lower plot: Differential luminosity as a function of $|y_{l\bar{l}}|$ for the correctly assigned quark pair (dashed-line) and for the full sample (solid line). (b) Same as (a) for valence down-quarks.

The statistical uncertainty on the $A_{\rm FB}$ is given by:

$$\delta A_{\rm FB} = \sqrt{\frac{4}{\mathcal{L}}\frac{\sigma_F\sigma_B}{(\sigma_F+\sigma_B)^3}} = \sqrt{\frac{(1-A_{FB}^2)}{\sigma\mathcal{L}}} = \sqrt{\frac{(1-A_{FB}^2)}{N}}, \tag{2.13}$$

where $\mathcal{L}$ is the integrated luminosity and N the total number of events. One can thus see that the significance is proportional to the root of the total number of events. Imposing a stringent cut on the boost variable, $y_{l\bar{l}}$, would then improve the reconstructed $A_{\rm FB}$ guiding it towards its true line shape, but it will decrease the statistics. In the next subsection, the subtle balance between line shape gain and statistics loss in maximizing the significance via the di-lepton rapidity cut will be discussed in detail.

2.2.2 On the di-lepton rapidity cut

As discussed above, since the true quark direction is not known in pp collisions, at the LHC one has to extract it from the kinematics of the di-lepton system. The valence quark direction here is approximated by the boost direction of the l^+l^- pairs with respect to the beam axis, that is given by the sign of the di-lepton rapidity $y_{l\bar{l}}$ defined in Eq. (2.11). The correctness of this assignment as a function of $y_{l\bar{l}}$ has been studied in Ref. [43] for di-lepton events with invariant masses above 400 GeV. Here this issue is analysed by investigating the energy scale dependence of the probability of getting

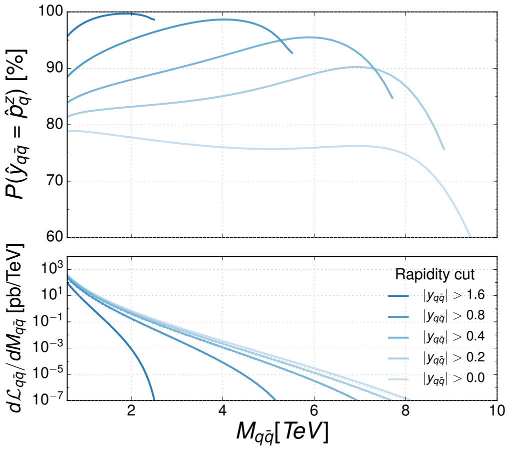

FIGURE 2.5: (Colour online) Upper plot: Probability of getting the correct direction of the valence quarks at the 13 TeV LHC via the boost direction of the di-lepton system, given by the sign of the di-lepton rapidity $y_{l\bar{l}}$, as a function of the di-quark (or di-lepton) invariant mass for five different cuts on the di-lepton rapidity. Lower plot: Differential luminosity as a function of the di-lepton invariant mass for the correctly assigned quark pair (dashed-line) and for the full sample (solid line). Here it is shown the average on both up and down-quarks.

the true quark direction via the sign of $y_{l\bar{l}}$. In Fig. 2.4, the fraction of events with the correctly assigned direction for up-quarks and down-quarks is shown, respectively, as a function of $|y_{l\bar{l}}|$ for different invariant mass windows of the di-lepton system. The fraction of correctly assigned events increases with the rapidity, confirming the results presented in literature [43].

The additional information contained in Fig. 2.4 is that such an increase depends on the energy scale. For di-lepton invariant masses of TeV order the probability of getting the true quark direction becomes more than 80% for a rapidity cut $|y_{l\bar{l}}| \geq 0.8$. For higher invariant masses, beyond the present Z'-boson limits of $O(3 \text{ TeV})$, the same probability can be obtained by imposing a lower rapidity cut: $|y_{l\bar{l}}| \geq 0.35$. Moreover, up-quarks and down-quarks respond differently to the $|y_{l\bar{l}}|$ cut. The probability of getting the correct direction is higher for up-quarks than for down-quarks, at fixed $|y_{l\bar{l}}|$ value. In Fig. 2.5, the fraction of correctly assigned events is shown as a function of the invariant mass for five different cuts on the magnitude of the di-lepton rapidity, $|y_{l\bar{l}}|$. This time, the average over up and down-quarks is considered. From here, one can see that, in searching for extra Z'-bosons with masses larger than $O(3 \text{ TeV})$ the $|y_{l\bar{l}}|$ cut is not mandatory. The true direction of the quark is indeed correctly guessed more than 70% of the times, even if no cut is applied on the di-lepton rapidity. This means that, at high di-lepton invariant masses, a lepton asymmetry with a well approximated shape should be visible even without imposing ad hoc cuts. As will be discussed in the next two pages, the advantage of not imposing a $|y_{l\bar{l}}|$-cut would be twofold: preserving a small statistical

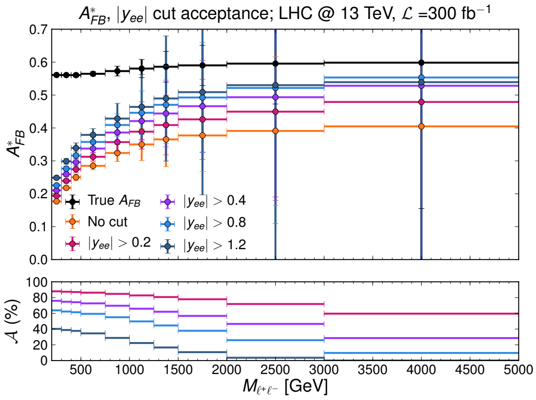

FIGURE 2.6: (Colour online) Upper plot: Reconstructed forward-backward asymmetry as a function of the di-lepton invariant mass within the SM at the 13 TeV LHC with a total integrated luminosity $\mathcal{L} = 300$ fb^{-1} for a set of different rapidity cuts on the di-lepton system. In the legend, $|y_{ee}|$ corresponds to $|y_{l\bar{l}}|$ defined in the text. The black line represents the true $A_{\rm FB}$ for comparison. Lower plot: Acceptance as a function of the di-lepton invariant mass for the same set of di-lepton rapidity cuts as above.

error on that shape, owing to the much larger acceptance one should have in absence of the $|y_{l\bar{l}}|$ cut (see Figs. 2.6 - 2.7), and working with an event sample flavour independent up to a large extent (see Fig. 2.7). This latter feature would guarantee a more model independent procedure, as the different Z' models have obviously different couplings of the extra gauge boson to up and down-quarks.

Let us start to clarify these two points. In order to quantify the delicate balance between $A_{\rm FB}$ line shape and statistical error, the upper plot of Fig. 2.6 shows the shape of the reconstructed lepton asymmetry, $A^*_{\rm FB}$, within the SM as a function of the di-lepton invariant mass for a set of different cuts on $|y_{l\bar{l}}|$. The results are compared to the true $A_{\rm FB}$, where the direction of the valence quark is taken directly from the MC event generator. The lower plot of Fig. 2.6 displays the acceptance as a function of the same variable $M_{l\bar{l}}$ for the same set of $|y_{l\bar{l}}|$ cuts. Comparing the two plots, one can see that $A^*_{\rm FB}$ tends to the true $A_{\rm FB}$ with increasing the $|y_{l\bar{l}}|$ cut, but at the same time the acceptance heavily decreases. In particular, for masses above 2.5 TeV, applying the stringent cut $|y_{l\bar{l}}| \geq 0.8$ used in literature, the number of events goes down by a factor of 3 while the gain in shape is only about 20% of the true $A_{\rm FB}$ value. With increasing mass, the acceptance decreases indeed more rapidly with the $|y_{l\bar{l}}|$ cut.

To visualize how the above features impact the $A_{\rm FB}$ sensitivity to new physics, in Fig. 2.7 the reconstructed $A^*_{\rm FB}$ observable predicted by three representative Z'-models (E6-χ, E6-I and GLR-LR) is compared with the SM expectation at the 13 TeV LHC, assuming a total integrated luminosity $\mathcal{L} = 100$ fb^{-1}. As a new physics signal, an hypothetical Z'-boson with mass $M_{Z'} = 3$ TeV is considered. The following results were derived during the early stage of the LHC Run-II [11], when the chosen benchmarks with this

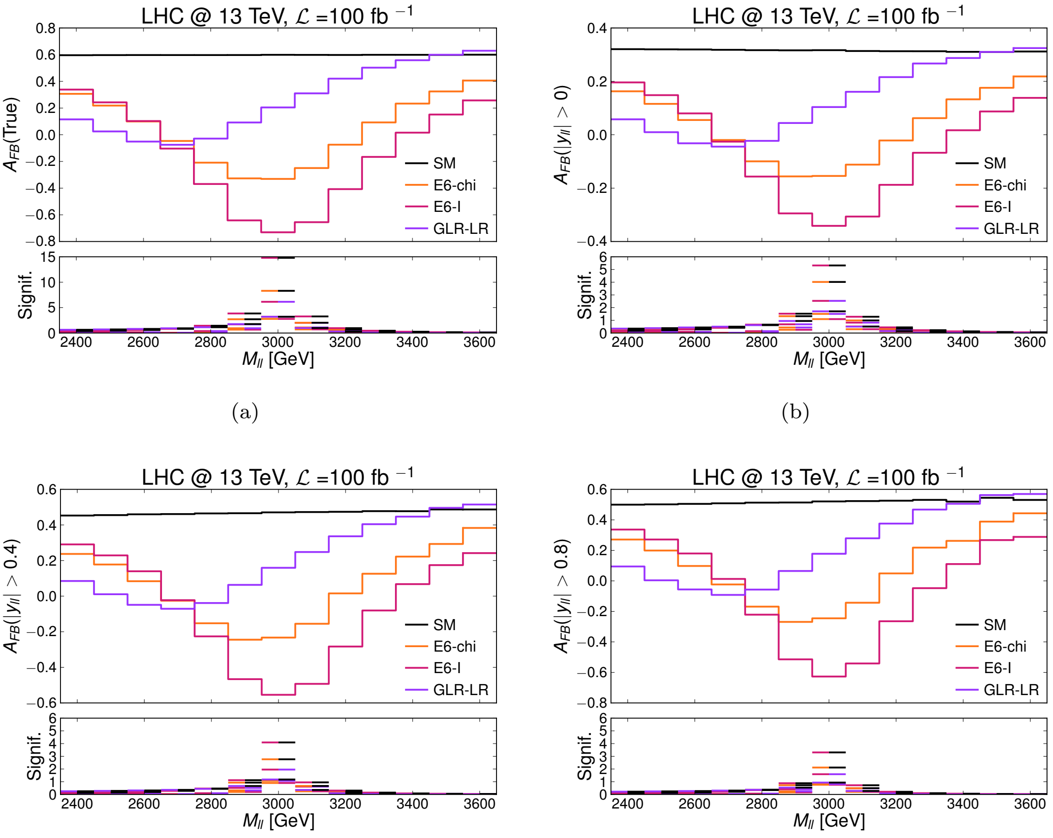

(a) (b)

(c) (d)

FIGURE 2.7: (Colour online) (a) True $A_{\rm FB}$ as a function of the di-lepton invariant mass as predicted by the SM (black), the E6-χ (orange), the E6-I (magenta) and the GLR-LR (purple) models for a Z'-boson with mass $M_{Z'} = 3$ TeV. The results are for the LHC at $\sqrt{s} = 13$ TeV and $\mathcal{L} = 100$ fb^{-1}. Lower plot: the significance in distinguishing models is displayed. The double colour in each bin visualizes the two compared models. (b) Reconstructed forward-backward asymmetry as a function of the di-lepton invariant mass as predicted by the SM (black), the E6-χ (orange), the E6-I (magenta) and the GLR-LR (purple) models for a Z'-boson with mass $M_{Z'} = 3$ TeV. The results are for the LHC at $\sqrt{s} = 13$ TeV and $\mathcal{L} = 100$ fb^{-1}. No cut on the di-lepton rapidity is imposed: $|y_{l\bar{l}}| \geq 0$. Lower plot: the significance in distinguishing models is displayed. (c) Same as plot (b) with $|y_{l\bar{l}}| \geq 0.4$. (d) Same as plot (b) with $|y_{l\bar{l}}| \geq 0.8$.

value for the Z'-boson mass were still allowed. However the same conclusions hold for benchmarks with $M_{Z'} \geq 4$ TeV, which is the current limit [36, 37].

To quantify the effect of the di-lepton rapidity cut on the significance either in searching for new physics via $A_{\rm FB}$ or in distinguishing between different Z' models, results for the commonly used $|y_{l\bar{l}}| \geq 0.8$ setup (Fig. 2.7(d)) are shown in comparison with the $|y_{l\bar{l}}| \geq 0.4$ (Fig. 2.7(c)) and with the no cut (Fig. 2.7(b)) scenarios. Furthermore in Fig. 2.7(a) the ideal situation represented by the true forward-backward asymmetry, A_{FB} is shown. As one can see, imposing a strong di-lepton rapidity cut helps in recovering the true shape and magnitude of the forward-backward asymmetry. However, the consequent decrease of the number of events is so substantial that the significance diminishes drastically with increasing the $|y_{l\bar{l}}|$ cut.

In addition, as previously anticipated, the implementation of the $|y_{l\bar{l}}|$ cut accentuates the flavour dependence of the results or, in other words, the model dependence of the analysis. As the probability of guessing the correct direction of the quark in the reconstruction procedure of the A_{FB} as a function of the $|y_{l\bar{l}}|$ cut depends on the type of quark (up and down-quarks react differently to the cut as shown in Fig. 2.4), the reconstructed A_{FB} shows an increased model dependence in its response to the $|y_{l\bar{l}}|$ cut. To exemplify this concept, consider for instance the third bin from the left in Fig. 2.7. There (Fig. 2.7(a)), the E6-χ and E6-I models are degenerate as far as the true asymmetry is considered. When comparing the reconstructed asymmetry, once can see that the two models are not degenerate any more in that bin. The splitting increases with the $|y_{l\bar{l}}|$ cut, as the two models react differently to such a cut, having different couplings of the corresponding Z'-boson to up- and down-quarks. In order to minimize the presence of model dependent elements in the analysis, it is thus advisable not to include the di-lepton rapidity cut. Hence, in the following such a restriction will not be imposed.

2.3 The role of A_{FB} in Z' searches: narrow heavy resonances

The A_{FB} is the observable where the effects of the interference between new physics and SM background are maximal. In the DY processes, these effects are of course present also in the total cross section. They are readily seen in both cases in the di-lepton invariant mass. As mentioned repeatedly, constraining the search window for new physics within the interval $|M_{l\bar{l}} - M_{Z'}| \leq 0.05 \times E_{\text{coll}}$ guarantees that FW and interference effects are below the $O(10\%)$ level when compared to the complete new physics signal. Such effects are instead an intrinsic part of the A_{FB} and dominate its dynamics. For such a reason, the A_{FB} is an intrinsically model dependent variable and in literature has therefore been traditionally considered for disentangling different models predicting a spin-1 heavy neutral particle. Its role has therefore been cornered so far to the interpretation of a possible Z'-boson discovery obtained via the default bump search.

This part focuses on showing that A_{FB} can also be used for searches, directly, as a primary variable alongside the cross section itself. Firstly, Z'-bosons characterized by a narrow width are considered. This is the most common kind of particle predicted by theories with an extra $U'(1)$ gauge group. This is also the scenario mostly studied in

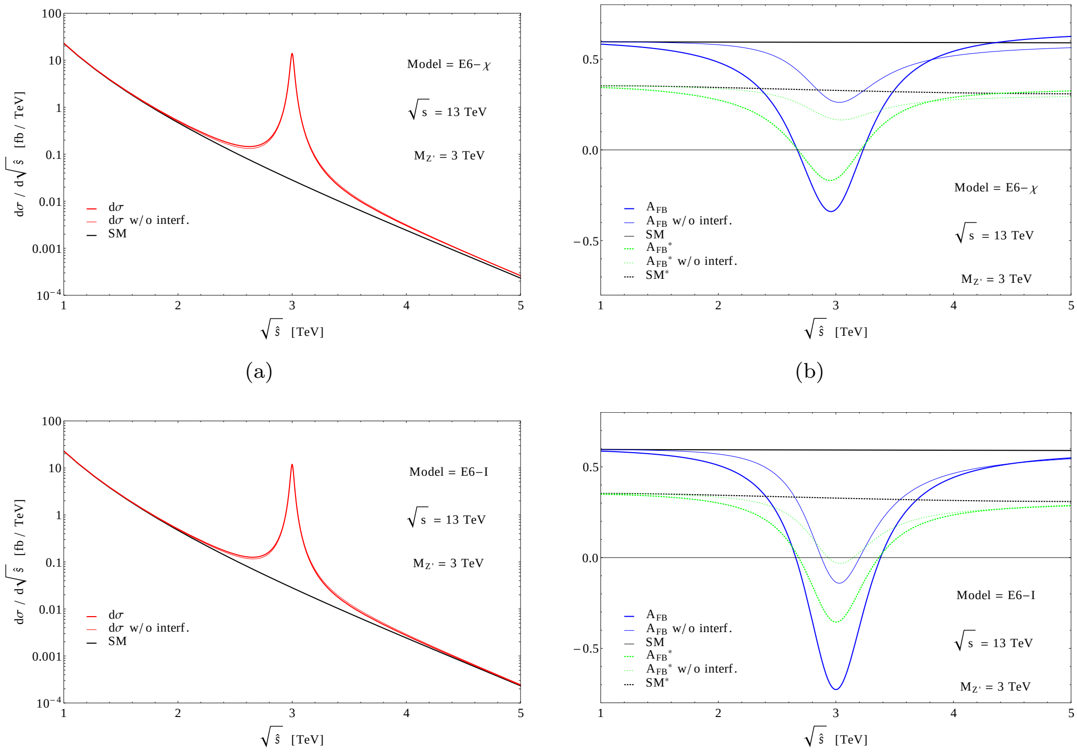

(a) (b)

(c) (d)

FIGURE 2.8: (Colour online) (a) Differential cross section as a function of the di-lepton invariant mass as predicted by the E6-χ model for a Z'-boson with mass $M_{Z'} = 3$ TeV. The results are for the LHC at $\sqrt{s} = 13$ TeV. (b) Reconstructed forward-backward asymmetry as a function of the di-lepton invariant mass as predicted by the E6-χ model for a Z'-boson with mass $M_{Z'} = 3$ TeV. The results are for the LHC at $\sqrt{s} =$ 13 TeV. No cut on the di-lepton rapidity is imposed: $|y_{l\bar{l}}| \geq 0$. (c) Same as plot (a) within the E6-I model. (d) Same as plot (b) within the E6-I model.

literature. The experimental searches for such an object are tailored on this expectation and the corresponding results coming from the data collected at the 8 TeV LHC have been summarized in Section 2.1. With respect to the 'A_{FB} search', the Z' models can be divided into two categories: Z' models with A_{FB} centred on the Z'-boson mass and Z' models with shifted A_{FB}. The next two subsections describe their properties in turn.

2.3.1 Z' models with A_{FB} centred on peak

In this subsection, models where the A_{FB} is peaked on the Z'-boson mass are described. These models belong to the E6 class of theories which predict new narrow width spin-1 resonances. In the literature, it is known that such models contain one extra neutral gauge boson whose width cannot exceed a few percent of its mass: $\Gamma_{Z'}/M_{Z'} \leq 5\%$. Even the inclusion of new Z'-boson decay channels into exotic states would not change this estimate.

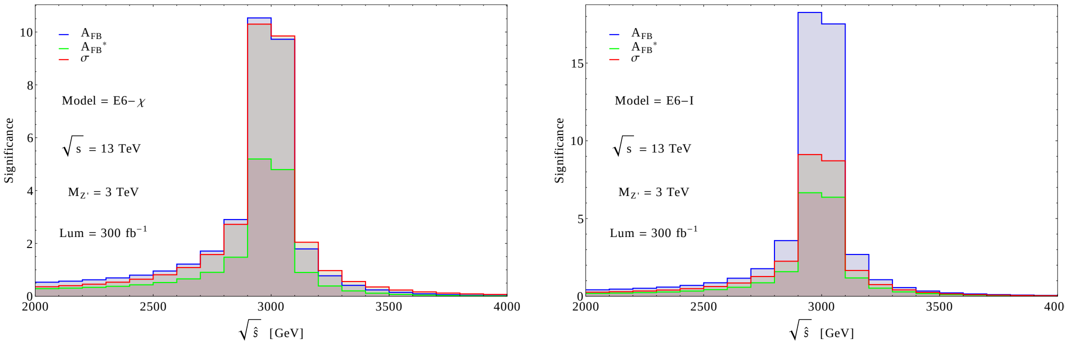

(a)

(b)

FIGURE 2.9: (Colour online) (a) Binned significance as a function of the di-lepton invariant mass as predicted by the E6-χ model for a Z'-boson with mass $M_{Z'} = 3$ TeV. The red line represents the significance corresponding to the invariant mass distribution. The blue and green lines show the significance extracted by an ideal measurement of true and reconstructed $A_{\rm FB}$, respectively. The results are for the LHC at $\sqrt{s} = 13$ TeV and $\mathcal{L} = 300$ fb^{-1}. (b) Same as (a) for the E6-I model.

In Fig. 2.8 the shape of the $A_{\rm FB}$ distribution as a function of the di-lepton invariant mass, $M_{l\bar{l}}$, is compared with the differential cross section in the same variable. In the plots is pictured the case of a hypothetical Z'-boson with mass $M_{Z'} = 3$ TeV in two representative E6 models: E6-χ and E6-I. The true and the reconstructed $A_{\rm FB}$ are displayed in Figs. 2.8(b) and 2.8(d) for the two chosen E6 models with and without taking into account the interference between the extra Z'-boson and the SM background. As one can see, the role played by the interference is extremely important. The $A_{\rm FB}$ shape is drastically modified by getting its peak heavily accentuated. In contrast, the invariant mass distribution is almost interference free if the $|M_{l\bar{l}} - M_{Z'}| \leq 0.05 \times E_{\rm coll}$ cut is imposed, as shown in Figs. 2.8(a) and 2.8(c) for the two representative E6 models. In interpreting the experimental data coming from $A_{\rm FB}$ measurements it is then mandatory to include the interference, no matter what kinematical cut is applied.

In terms of significance, the search for narrow width Z'-bosons with $A_{\rm FB}$ centred on the Z' mass is summarized in Fig. 2.9 for the two representative models E6-χ and E6-I. Within the E_χ model, the true $A_{\rm FB}$ would give rise to a significance slightly lower than that one coming from the usual bump search, as shown in Fig. 2.9(a). The reconstruction procedure of the $A_{\rm FB}$ depletes this result but still the two significances from cross section and $A^*_{\rm FB}$ are comparable over the full di-lepton invariant mass range. Fig. 2.9(b) shows that the E6-I model is more accessible through the $A_{\rm FB}$ than the cross section. There, indeed, the significance from the true $A_{\rm FB}$ is a factor two bigger than the significance coming from the bump search. Once again, the $A_{\rm FB}$ reconstruction pollutes the ideal result. The significance from the reconstructed $A_{\rm FB}$ gets reduced, but its value remains anyhow only slightly lower than that one coming from the resonance search. The E6-I model is not unique in this respect, also the E6-S model shares the same property.

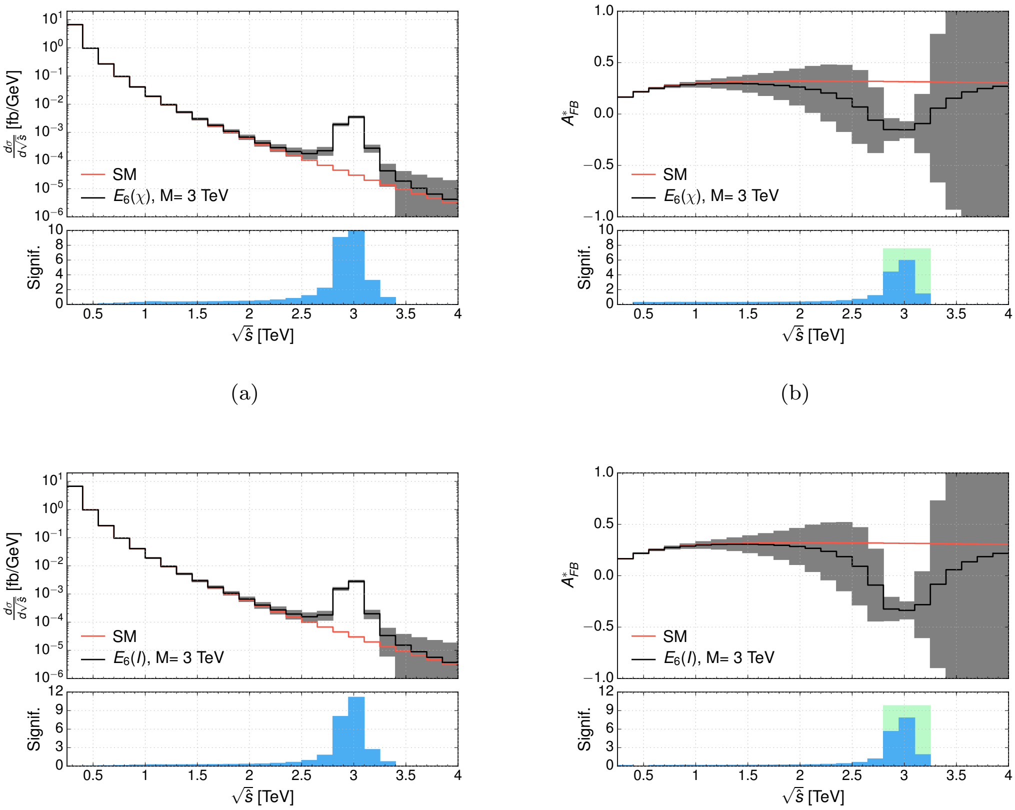

(a) (b)

(c) (d)

Figure 2.10: (Colour online) (a) Binned differential cross section as a function of the di-lepton invariant mass within the E6-χ model for a Z'-boson with mass $M_{Z'} = 3$ TeV. Error bars are included. The results are for the LHC at $\sqrt{s} = 13$ TeV and $\mathcal{L} = 300$ fb^{-1}. Acceptance cuts are imposed (see text). The lower plot shows the significance. (b) Binned $A^*_{\rm FB}$ as a function of the di-lepton invariant mass within the E6-χ model for a Z'-boson with mass $M_{Z'} = 3$ TeV. Error bars are included. The results are for the LHC at $\sqrt{s} = 13$ TeV and $\mathcal{L} = 300$ fb^{-1}. Acceptance cuts are imposed (see text). In the lower plot, the blue histogram shows the binned significance while the green area indicates the total significance integrated over that invariant mass region. (c) Same as (a) for the E6-I model. (d) Same as (b) for the E6-I model.

Similar trends are shown by all models belonging to the E6 class of theories and do not change when a more realistic setup is considered. Implementing the acceptance cuts extracted by the CMS analysis at the 8 TeV LHC ($|\eta_l| < 2.5$ and $p_T^l > 20$ GeV with $l = e, \mu$), the shape of the reconstructed $A_{\rm FB}$, $A^*_{\rm FB}$, including error bars would in fact appear as in Fig. 2.10. The significances coming from the $A_{\rm FB}$ and the cross section are indeed equivalent in magnitude, if only the statistical error is included. In this context the use of the $A^*_{\rm FB}$ observable, when associated to the default resonance search, could improve the discovery potential of new narrow width Z'-bosons. Further, being a ratio of differential cross sections, the reconstructed $A^*_{\rm FB}$ could help in minimizing the systematic errors thus rendering the measurement much more accurate.

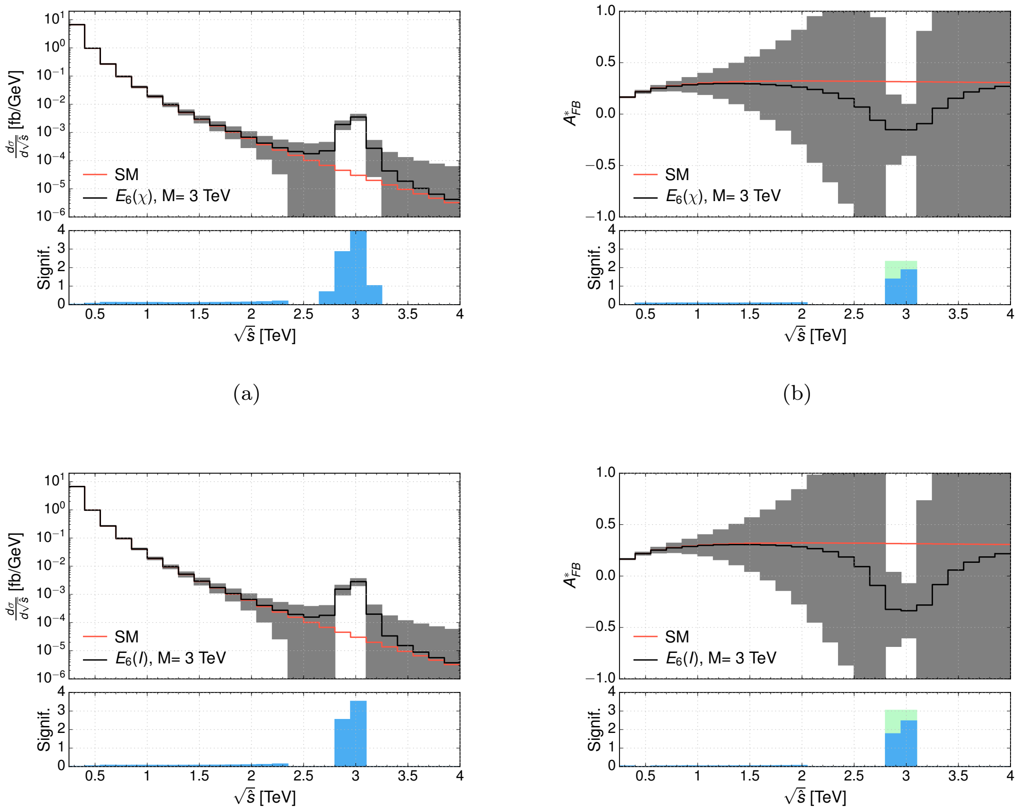

(a) (b)

(c) (d)

FIGURE 2.11: (Colour online) (a) Binned differential cross section as a function of the di-lepton invariant mass as predicted by the E6-χ model for a Z'-boson with mass $M_{Z'} = 3$ TeV. Error bars are included. The results are for the LHC at $\sqrt{s} = 13$ TeV and $\mathcal{L} = 30$ fb^{-1}. Acceptance cuts are imposed (see text). The lower plot shows the significance. (b) Binned $A^*_{\rm FB}$ as a function of the di-lepton invariant mass as predicted by the E6-χ model for a Z'-boson with mass $M_{Z'} = 3$ TeV. Error bars are included. The results are for the LHC at $\sqrt{s} = 13$ TeV and $\mathcal{L} = 30$ fb^{-1}. Acceptance cuts are imposed (see text). In the lower plot, the blue histogram shows the significance bin by bin while the green area indicate the total significance integrated over that invariant mass region. (c) Same as (a) for the E6-I model. (d) Same as (b) for the E6-I model.

This is in particular the case when in presence of an evidence for a new Z'-boson in the resonance search at the 3-4σ level. In these conditions, one could not claim the discovery of a new gauge boson just looking at the resonant peak in the di-lepton invariant mass distribution. However, if a signal of similar strength were to be discovered in an independent observable, the suggestion of the possible presence of new physics would turn into a robust claim. This is the role that the $A_{\rm FB}$ would play. The differential cross section and the $A^*_{\rm FB}$ are plotted in Fig. 2.11 as a function of the di-lepton invariant mass, $M_{l\bar{l}} = \sqrt{\hat{s}}$, within the E6-$\chi$ and E6-I models, at the 13 TeV energy of the LHC Run-II with $\mathcal{L} = 30$ fb^{-1}. There, a new physics evidence at barely 4σ in the bump search could be reinforced by the simultaneous measurement of the reconstructed $A_{\rm FB}$, showing a signal at the 2σ level.

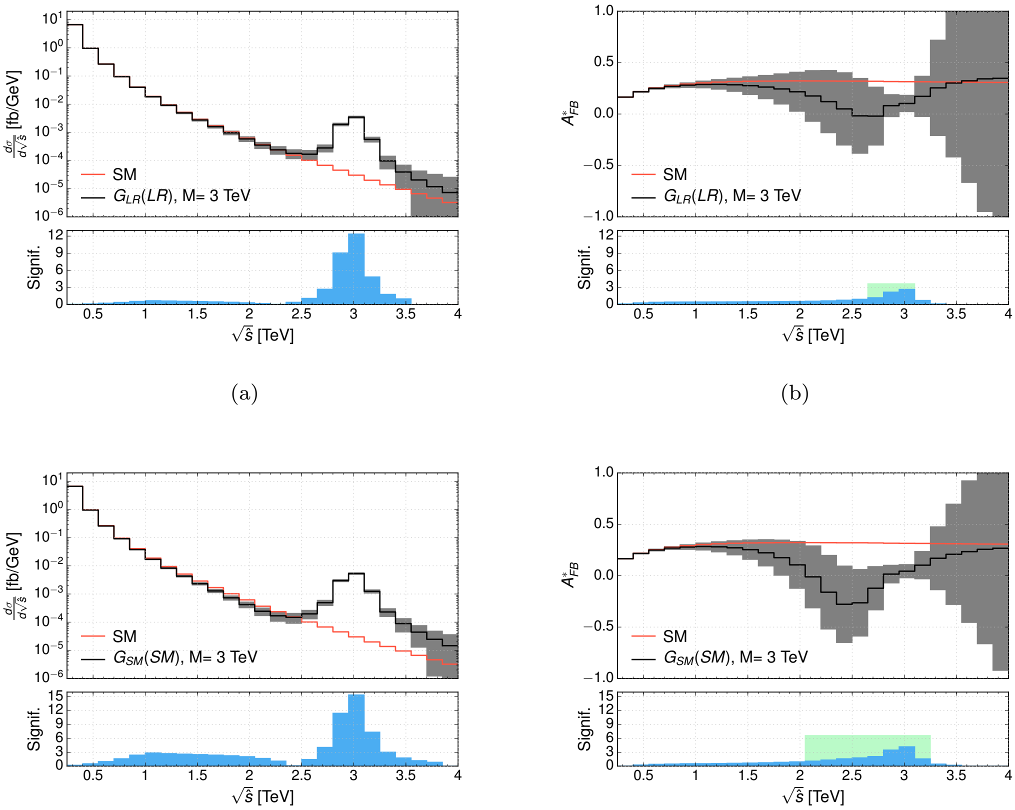

(a) (b)

(c) (d)

FIGURE 2.12: (Colour online) (a) Binned differential cross section as a function of the di-lepton invariant mass as predicted by the GLR-LR model for a Z'-boson with mass $M_{Z'} = 3$ TeV. Error bars are included. The results are for the LHC at $\sqrt{s} = 13$ TeV and $\mathcal{L} = 300$ fb^{-1}. Acceptance cuts are included (see text). (b) Binned $A^*_{\rm FB}$ as a function of the di-lepton invariant mass as predicted by the GLR-LR model for a Z'-boson with mass $M_{Z'} = 3$ TeV. Error bars are included. The results are for the LHC at $\sqrt{s} = 13$ TeV and $\mathcal{L} = 300$ fb^{-1}. Acceptance cuts are included (see text). (c) Same as (a) for the GSM-SSM model. (d) Same as (b) for the GSM-SSM model.

2.3.2 Z' models with shifted $A_{\rm FB}$

This section discusses the case of narrow width Z' models where the $A_{\rm FB}$ has a shifted peak, that is, not centred on the Z'-boson mass. These models belong to the GLR class. The same behaviour is also displayed by the SSM scenario taken as benchmark model by the LHC experimental collaborations.

In principle, the reconstructed $A^*_{\rm FB}$ could reveal the presence of a new spin-1 particle at energy scales lower than its mass, as the shape of this observable as a function of the di-lepton invariant mass is accentuated at mass scales smaller than $M_{Z'}$. This behaviour is shown in Fig. 2.12(b) where is plotted the reconstructed $A_{\rm FB}$ versus $M_{l\bar{l}} = \sqrt{\hat{s}}$ for the representative model GLR-LR. Again is assumed a Z'-boson mass $M_{Z'} = 3$ TeV. As one can see, the peak of $A^*_{\rm FB}$ is shifted on the left-hand side of the physical Z'-boson mass and it appears at around 2.6 TeV. However, the significance is quite low as shown in Fig. 2.12(b), owing to the poor statistics in that region. For $M_{l\bar{l}}$ values around the physical mass of the Z'-boson, which are statistically relevant, the significance coming from $A_{\rm FB}$ is always much smaller than the significance obtained via the measurement of the differential cross section, displayed in Fig. 2.12(a). For these kind of models, the $A^*_{\rm FB}$ observable is therefore not particularly appropriate for Z' searches. The same conclusion holds for the SSM (see Figs. 2.12(c) and 2.12(d)). Hence, this benchmark model is not an advisable playground for studying the benefits of using the $A_{\rm FB}$ in searching for new Z'-bosons.

2.4 The role of $A_{\rm FB}$ in Z' searches: wide heavy resonances

This section describes the role of the $A^*_{\rm FB}$ in searches for a new Z'-boson characterized by a large width. Such a heavy and wide particle is predicted by different models. A benchmark scenario for experimental analyses is the wide version of the SSM described in Ref. [44]. The proposal is to have a heavy copy of the SM neutral gauge boson, Z, with same couplings to ordinary matter and SM gauge bosons. Owing to the Z'-boson decay into SM charged gauge bosons, whose rate grows with the third power of the Z'-boson mass, the total width of the new heavy particle can be in principle quite large: $\Gamma_{Z'}/M_{Z'} \simeq 50\%$ and above. In reality, a word of caution should be spent at this point. The triple $Z'WW$ coupling is governed by the mixing of the extra Z' with the SM Z-boson. The actual size of this $Z - Z'$ mixing is strongly constrained by the EWPT, see Ref. [45] for a review on these bounds. In this context, in order to simulate phenomenological possible scenarios the Z' width can be considered as a free parameter.

Under this assumption and for a $\Gamma_{Z'}/M_{Z'}$ ratio of several tens of percent, the invariant mass distribution of the two final state leptons does not show in the cross section a resonant (or peaking) structure around the physical mass of the Z'-boson standing sharply over a smooth background.

For wide Z's, the experimental collaborations look for both resonances and effectively very wide resonances in non-resonant searches. In the first case, ATLAS has provided us with acceptance curves that can be used to rescale the limits obtained for narrow resonances, for widths up to 5–10% of the mass at the most [37]. In the second ('effectively' non-resonant case, where the width-to-mass region can be over 10%), the experimental analyses are essentially counting experiments. This consists in imposing a lower cut on the di-lepton invariant mass and in integrating from there over the whole di-lepton spectrum, searching for an excess of events. Such an excess could appear as a shoulder over the expected SM background in case of wide resonances or as a plateau standing over

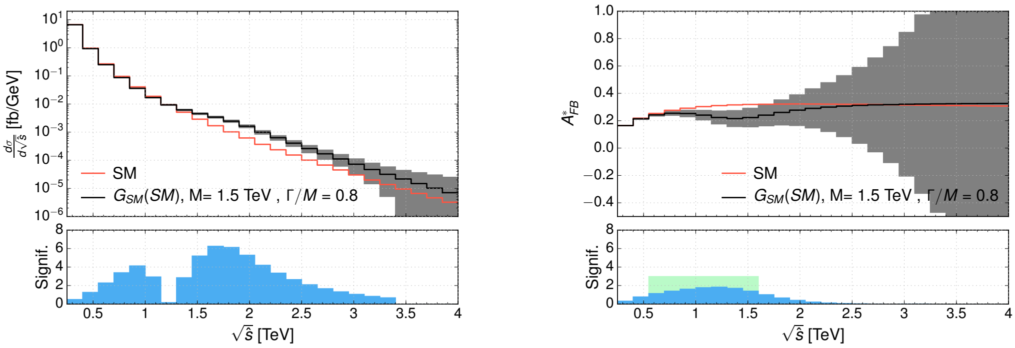

(a)

(b)

FIGURE 2.13: (Colour online) (a) Binned differential cross section as a function of the di-lepton invariant mass as predicted by the GSM-SM model for a Z'-boson with mass $M_{Z'} = 1.5$ TeV and $\Gamma_{Z'}/M_{Z'} = 80$ %. Error bars are included. The results are for the LHC at $\sqrt{s} = 13$ TeV and $\mathcal{L} = 300$ fb^{-1}. Acceptance cuts are included (see text). (b) Binned A^{*}_{FB} as a function of the di-lepton invariant mass as predicted by the GSM-SM model for a Z'-boson with mass $M_{Z'} = 1.5$ TeV and $\Gamma_{Z'}/M_{Z'} = 80$ %. Error bars are included. The results are for the LHC at $\sqrt{s} = 13$ TeV and $\mathcal{L} = 300$ fb^{-1}. Acceptance cuts are imposed (see text).

the SM background in case of contact like BSM interactions. These last searches optimize selection criteria in the context of particular specific models order to maximise the discovery/exclusion potential at the LHC. However the experimental results obtained following this approach heavily rely on the good understanding and control of the SM background.

The typical shape of a non-resonant structure is plotted in Fig. 2.13(a), where is considered a Z'-boson with mass $M_{Z'} = 1.5$ TeV and width $\Gamma_{Z'}/M_{Z'} = 80$ %. As the line shape of the resonance is not well defined and these parton level results could be worsened by detector smearing effects giving rise to an even broader spectrum, the A^{*}_{FB} observable could help to interpret a possible excess of events. The results are shown in Fig. 2.13(b) which shows that the A^{*}_{FB} shape could be visible at the 2σ level.

A framework, theoretically more grounded than the wide SSM, which predicts a heavy and broad Z'-boson is the so-called non-universal $SU(2)$ model (NU SM) [46, 47]. In this theory, the third generation of fermions is subjected to a new $SU(2)$ dynamics different from the usual weak interaction advocated by the SM. On the contrary, the first two families of fermions only feel the SM weak interaction. Owing to the non universality of the gauge interactions, different consequences appear in this model. The CKM matrix is not unitary anymore, although the unitarity violation is suppressed by the heavy scale of the new physics. Also, Flavour Changing Neutral Currents (FCNCs) can generally show up. In addition and of primary interest for this paper, a new spectrum of gauge bosons emerges in the model. These new vector bosons can be either narrow or wide.

The only constraint on the model parameters comes from the EWPTs which bound the Z'-boson to have a mass $M_{Z'} \geq 1.7$ TeV. The constraints on mass and couplings of the heavy Z' boson are actually correlated. Usually, they are presented as a two-dimensional contour plot. For the details of the analysis of direct and indirect limits on this model see [47] and references therein.

Within this framework, a wide Z'-boson case with $M_{Z'} = 5.5$ TeV and $\Gamma_{Z'}/M_{Z'} = 20\%$ is considered. This setup fulfils both the limits quoted in Ref. [47] and the direct limits coming from direct searches at the 8 TeV LHC [11]. The latter analysis performed at the LHC has been optimized for searches of new physics with no resonant peaking structure. The outcome is that there are no events for di-lepton invariant masses above 1.8 TeV, and this limit has been taken into account when evaluating the Z'-boson mass and width.

This model is a very good playground to test whether the A_{FB} can be used as a primary variable in searches for wide objects. In this case, in fact, the new physics signal appears as an excess of events spread over the SM background. Almost no line shape is present in the di-lepton invariant mass distribution usually measured. Searches are performed relying on a pure counting strategy, a procedure which does not allow much interpretation of the hypothetical signal. The exploitation of the reconstructed A^*_{FB} could help in this respect.

Fig. 2.13 shows the Z'-boson spectrum (2.14(a)) and the reconstructed A^*_{FB} (2.14(b)) as functions of the di-lepton invariant mass. As one can see in Fig. 2.14(a), the signal cross section slope might be lost or mistaken in the SM background normalization. Even if, in the best case, a plateau would be visible over the SM background, its interpretation would be very difficult. The same degree of difficulty would appear in interpreting the depletion of events in the low invariant mass region. In principle such a depletion, due to the negative interference between the extra Z'-boson and the SM background, could give rise to a huge significance as shown in Fig. 2.14(a) (lower plot). However, the experimental fitting procedure for this kind of scenarios is not fully settled yet. Severe uncertainties could affect the functional form chosen to simulate the SM background in the data-driven approach, as the new physics effects might invade the low mass spectrum that is instead commonly assumed to be new physics free. The same would happen for the alternative procedure based on the MC estimate of the SM background, as this approach relies on the normalization of the MC prediction to the data around the peak of the SM Z-boson and on the existence of a new physics free control region at low invariant masses. Moreover, even in the ideal case in which all errors were under control, the interpretation of such evidence would be quite complicated, having no defined shape at all. In this context, the A_{FB} can be of some help. Fig. 2.14(b) shows that the A^*_{FB}

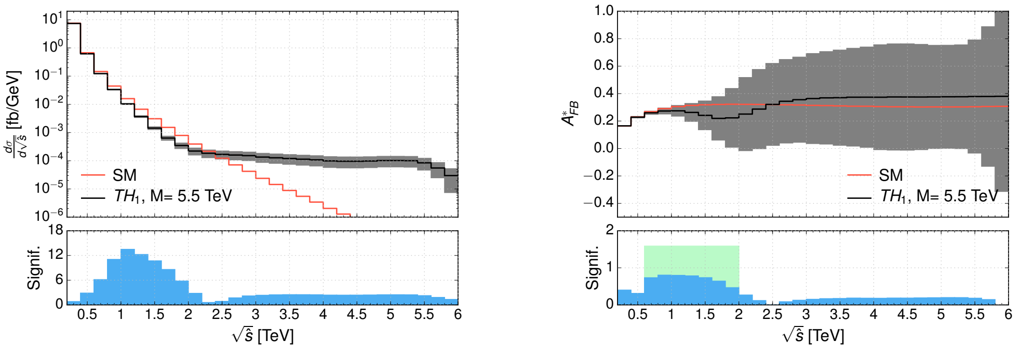

(a) (b)

FIGURE 2.14: (Colour online) (a) Binned differential cross section as a function of the di-lepton invariant mass as predicted by the non-universal SM (NU SM) for a Z'-boson with mass $M_{Z'} = 5.5$ TeV and $\Gamma_{Z'}/M_{Z'} \simeq 20$ %. Error bars are included. The results are for the LHC at $\sqrt{s} = 13$ TeV and $\mathcal{L} = 300$ fb^{-1}. Acceptance cuts are imposed (see text). (b) Binned $A^*_{\rm FB}$ as a function of the di-lepton invariant mass as predicted by the NU SM for a Z'-boson with mass $M_{Z'} = 5.5$ TeV and $\Gamma_{Z'}/M_{Z'} \simeq 20$ %. Error bars are included. The results are for the LHC at $\sqrt{s} = 13$ TeV and $\mathcal{L} = 300$ fb^{-1}. Acceptance cuts are imposed (see text).

observable has a sharper line-shape which can reveal the presence of a spin-1 particle beyond error bars. Such a shape is quite shifted at low energy scales though, compared to the Z'-boson mass. Hence, its extraction should enable one to help the discovery of a new vector boson with very high mass. In short, here, the $A_{\rm FB}$ measurement could become particularly useful at the edge of the LHC discovery limits, when new particles can be too heavy and broad to be easily detected via a standard resonant peak search.

The aforementioned scenarios are in fact particularly challenging for experimentalists. The non-resonant analyses of wide objects have been performed by searching for a smooth deviation from the SM background. The number of events above a given lower cut on the di-lepton invariant mass is compared with the total number of expected background events. An optimal minimum mass threshold is chosen to maximize the sensitivity to new physics. Clearly, such an analysis depends quite strongly on the SM background estimate. Usually, the simulated background is normalized to the event number in a mass window of ± 30 GeV around the Z-boson mass. A control region is then selected at higher di-lepton invariant masses in order to perform a data driven modelling of the SM background and recast it in a functional form easy to implement in the likelihood used for extracting the limit on the Z'-boson mass. The method is based on the assumption that the control region is new physics free. But, this is not the case for wide Z'-bosons. In these scenarios, the interference between the extra Z'-boson and the SM γ, Z is so sizeable that it can invade the control region. Being absolutely model-dependent, it can be either constructive or destructive. In any case, it would change accordingly the shape of the di-lepton spectrum. If the interference is negative, it would led to a depletion of events at low mass scales on the left-hand side of the Z'-boson resonance. This is exactly the example shown in Figs. 2.13 and 2.14 corresponding to the SSM and NU SM scenarios, respectively. If not correctly interpreted, these interference effects could induce one to underestimate the SM background with the consequence of overestimating the extracted mass bounds. Having all these uncertainties to deal with, the support of a second observable like the A_{FB} is strongly recommended for the non-resonant analyses.

2.5 On the robustness of A_{FB} against PDF uncertainties

This section discusses how robust the shape of the forward-backward asymmetry is against the theoretical uncertainties on the PDFs. The systematic error induced by the PDF uncertainty on the differential cross section and on the reconstructed A_{FB} is compared with the statistical one.

The determination of the PDF uncertainty is obtained following [48, 49] and references therein. Just some highlight of the key points of the procedure are given here. The Hessian PDF uncertainty is computed for our two observables: di-lepton invariant mass distribution and reconstructed A_{FB}. For Hessian PDF sets, both a central set and error sets are given. The number of error sets is twice the number of eigenvectors. For the CTEQ6 PDF that are being used, the number of error sets is equal to 40. For a given observable X, the $X_i^{\pm}$ are defined to be the value of the observable using the PDF error set corresponding to the "±" direction for the eigenvector i. The symmetric error on the observable X is then given by:

$$\Delta X = \frac{1}{2}\sqrt{\sum_{i=1}^{N} |X_i^+ - X_i^-|^2}. \tag{2.14}$$

With this definition, one can compute the PDF uncertainty on any observable X or any function $f(X)$. For the differential cross section, $X = \sigma$, Eq. 2.14 is directly applied. For the A_{FB}, the computation is slightly more involved since the observable is a ratio of (differential) cross sections. In this case, the forward and backward (differential) cross sections, σ_F and σ_B, are considered as independent variables so as the observable $A^*_{\mathrm{FB}} = f(\sigma_F, \sigma_B)$. According to Eq. (2.14), the PDF uncertainty on σ_F and σ_B is given by:

$$\Delta\sigma_F = \frac{1}{2}\sqrt{\sum_{i=1}^{N} |\sigma_F{}_i^+ - \sigma_F{}_i^-|^2} \qquad ; \Delta\sigma_B = \frac{1}{2}\sqrt{\sum_{i=1}^{N} |\sigma_B{}_i^+ - \sigma_B{}_i^-|^2}. \tag{2.15}$$

In the Hessian approach, the correlation of the PDF degrees of freedom of any two independent observables, X and Y, is expressed by the quantity $\cos\phi$ given in Ref. [49] and reported here below:

$$\cos\phi = \frac{1}{4\Delta X \Delta Y} \sum_{i=1}^{N} (X_i^+ - X_i^-)(Y_i^+ - Y_i^-). \tag{2.16}$$

The quantity $\cos\phi$ characterizes whether the PDF degrees of freedom of X and Y are partially or fully correlated ($\cos\phi = 1$), fully anti-correlated ($\cos\phi = -1$) or uncorrelated ($\cos\phi = 0$). Such a quantity enters in the definition of the PDF uncertainty on any function of two variables, $\Delta f(X,Y)$, as shown in the formula here below (see also Ref. [49]):

$$\Delta f(X,Y) = \sqrt{(\Delta X \partial_X f)^2 + 2\Delta X \Delta Y \cos\phi \partial_X f \partial_Y f + (\Delta Y \partial_Y f)^2}. \tag{2.17}$$

In this case the two independent observables, $X = \sigma_F$ and $Y = \sigma_B$, are fully correlated for all analysed Z' models ($\cos\phi(\sigma_F, \sigma_B) = 1$) being evaluated at the same energy scale when computing A^*_{FB} as a function of the di-lepton invariant mass. Under this condition, by applying the error chain rule as in Eq. (2.17), follows:

$$\Delta A^*_{\mathrm{FB}} = \frac{1}{2}\left(1 - {A^*_{\mathrm{FB}}}^2\right)\left|\frac{\Delta\sigma_F}{\sigma_F} - \frac{\Delta\sigma_B}{\sigma_B}\right|. \tag{2.18}$$

The sign appearing in the above formula is crucial for the A_{FB}. It indeed clearly shows that there is a partial cancellation of the PDF error on the reconstructed A^*_{FB} due to the fact that this observable is a ratio of (differential) cross sections. Compared to the differential cross section, the A_{FB} is then more robust against PDF uncertainties. This is shown in Fig. 2.15 where the effect of PDF and statistical errors on the shape of the di-lepton invariant mass distribution of the cross section and A_{FB} are compared for two reference models, E6-I and E6-χ.

As one can see, the behaviours of cross section and A_{FB} are opposite. The differential cross section in the di-lepton invariant mass is dominated by the PDF error on-peak and in the low invariant mass region. In the region around the peak and for invariant masses below the TeV region, the PDF uncertainty is a factor 2 bigger than the statistical

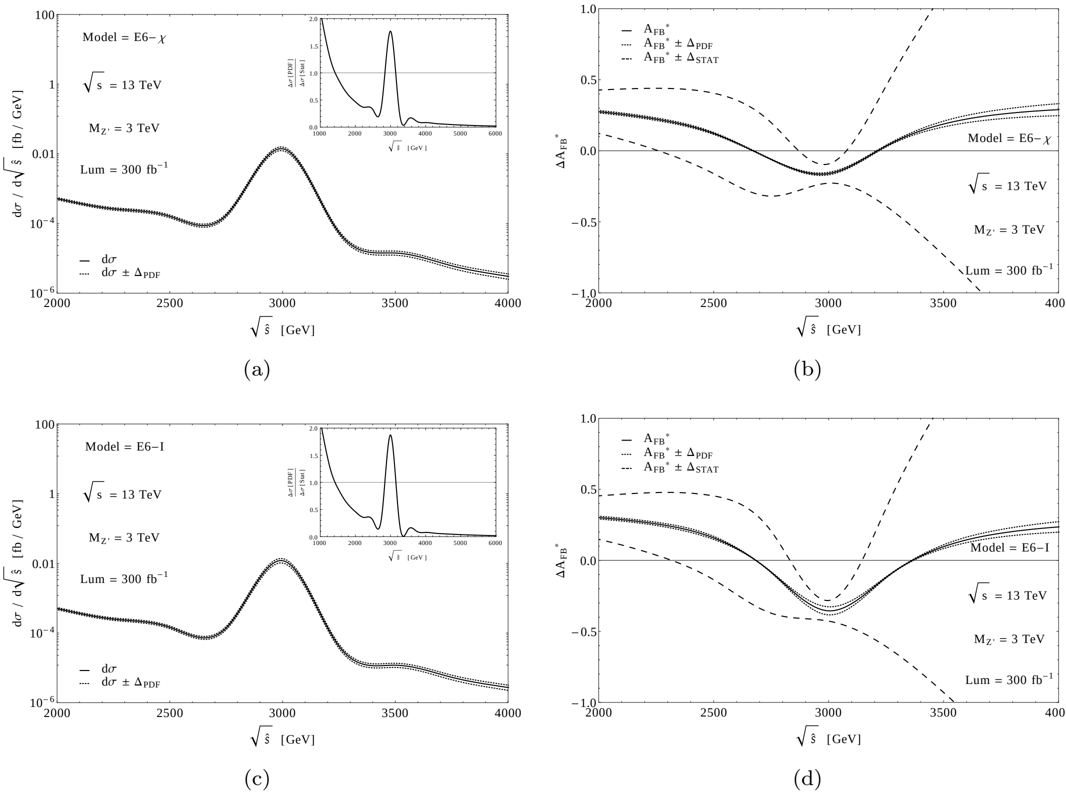

FIGURE 2.15: (a) Differential cross section as a function of the di-lepton invariant mass as predicted by the E6-χ model for a Z'-boson with mass $M_{Z'} = 3$ TeV. The results are for the LHC at $\sqrt{s} = 13$ TeV and $\mathcal{L} = 300$ fb^{-1}. The solid line shows the central value, the dotted line the PDF uncertainty. The inset plot displays the ratio between PDF and statistical errors. (b) $A^*_{\rm FB}$ as a function of the di-lepton invariant mass as predicted by the E6-χ model for a Z'-boson with mass $M_{Z'} = 3$ TeV. The results are for the LHC at $\sqrt{s} = 13$ TeV and $\mathcal{L} = 300$ fb^{-1}. The dotted lines show the PDF error band, while the dashed lines define the statistical error band. (c) Same as (a) for the E6-I model. (d) Same as (b) for the E6-I model.

error. On the contrary, the $A_{\rm FB}$ is always dominated by the statistical error: on and off-peak. Moreover, the PDF uncertainty is quite reduced owing to the minus sign in Eq. (2.18). The shape of the $A_{\rm FB}$ is thus not affected by the PDF error, so this observable is theoretically well defined.

In the light of these results, consider again Figs. 2.10 and 2.11 which compare differential cross section and $A_{\rm FB}$ for two representative E6 models and for two luminosity regimes: $\mathcal{L} = 300$ fb^{-1} and $\mathcal{L} = 30$ fb^{-1} respectively. As stated previously, in the low luminosity regime the $A_{\rm FB}$ could help interpreting the data. As illustrated in Fig. 2.11, the $A_{\rm FB}$ significance could be in fact comparable to that found using the cross section from a binned mass distribution. In case of an early discovery with a few events, the evidence of new physics from the bump search alone would be insufficient to demonstrate the presence of a new Z'. But, it could be reinforced by a further comparable evidence in the independent variable A^*_{FB}, leading to a much more robust result.

The role of $A_{\rm FB}$ in searching for new Z'-bosons is not confined to support a not fully convincing evidence in the usual bump search at low statistics. In this section, the main message is that, even after the high luminosity objective is achieved for the current LHC Run-II, the $A_{\rm FB}$ may provide additional evidence of new physics and be very useful in the interpretation of the origin of this new physics. As stated above, this time the reason is the PDF's uncertainty which will dominate the theoretical error on the prediction of a new Z'-boson appearing as a resonant peak in the di-lepton invariant mass distribution. To be more quantitative, consider Figs 2.10(a) and 2.10(c). There, owing to the decreased statistical error when compared to Figs 2.11(a) and 2.11(c), there is an a priori statistical significance $S \simeq 12$ around the peak of the binned cross section which would allow to claim for a new physics discovery. However, the total theoretical error does not improve much with $\mathcal{L}$, being dominated by PDF's uncertainties. Indeed, in this case, the PDF error would be two times the statistical one (see Fig. 2.15). The capability of interpreting the results of an experiment is thus significantly reduced by PDF's uncertainties in the bump search. This result should be compared with the outcome from an $A^*_{\rm FB}$ measurement, which is shown in Figs 2.10(b) and 2.10(d). Here, owing to the higher luminosity, the experimental significance is about $S \simeq 7$ (including only the statistical error). Such an increase with $\mathcal{L}$ would be moreover followed by a proportional reduction of the theoretical error that in this case is purely dominated by statistics. Up to a large extent, the $A_{\rm FB}$ is therefore a PDF safe observable. For these reasons, even if the large-x PDF's uncertainties are considerably improved in the future, it is likely that an $A^*_{\rm FB}$ measurement will prove to be useful evidence in any claims of Z' discoveries using the LHC data.

Of course, one needs to consider the energy scale dependence of the PDF errors, if no refitting procedure is employed. Fig. 2.16(a) shows the PDF and statistical errors on the total cross section integrated around the mass of the Z'-boson. The integration is in the window $\pm 5\%\ \ E_{\rm coll}$ around the hypothetical $M_{Z'}$ where interference and finite width effects can be neglected. The designed value for the luminosity $\mathcal{L} = 300$ fb^{-1} is assumed in the evaluation of the statistical error and the value of $M_{Z'}$ is varied to see how statistical and PDF errors change in magnitude. Four benchmarks are considered: E6-χ, E6-I, GLR-LR and GSM-SSM. The figure shows that, up to roughly a 4 TeV scale, the cross section is dominated by the PDF uncertainty. In contrast, the asymmetry integrated in the same peak region is heavily dominated by the statistics for all possible Z' masses, as shown in Fig. 2.16(b).

The strong dependence of PDF's central values and errors on the di-lepton invariant mass or energy scale also suggests that using as observable the ratio between the Z'-boson cross section and the on-peak SM Z-boson cross section R_σ, might not be entirely PDF safe. The two cross sections are indeed a few TeV a part. As a consequence,

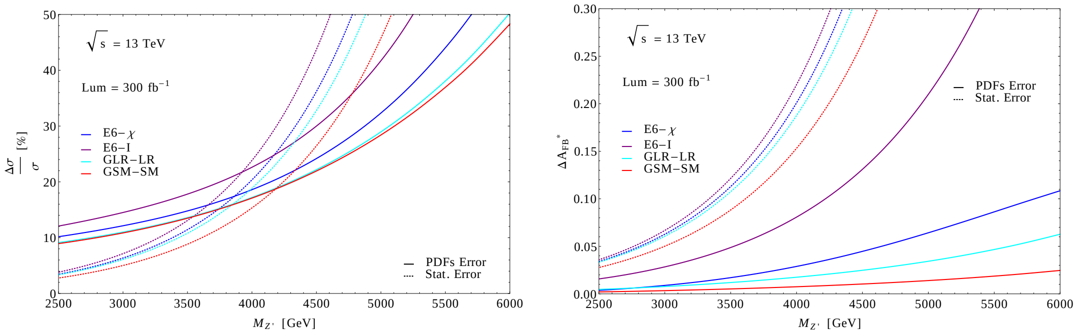

(a)

(b)

FIGURE 2.16: (Colour online) (a) Cross section integrated around the Z'-boson mass ($|M_{l\bar{l}} - M_{Z'}| \leq 0.05 \times E_{\text{coll}}$) as a function of $M_{Z'}$ as predicted by the E6-χ, E6-I, GLR-LR and GSM-SSM models. The results are for the LHC at $\sqrt{s} = 13$ TeV and $\mathcal{L} = 300$ fb^{-1}. Solid lines represent the PDF uncertainty, dashed ones the statistical error. (b) A^*_{FB} integrated around the Z'-boson mass ($|M_{l\bar{l}} - M_{Z'}| \leq 0.05 \times E_{\text{coll}}$) as a function of $M_{Z'}$ as predicted by the E6-χ, E6-I, GLR-LR and GSM-SSM models. The results are for the LHC at $\sqrt{s} = 13$ TeV and $\mathcal{L} = 300$ fb^{-1}. Solid lines represent the PDF uncertainty, dashed ones the statistical error.

the quantity $cos\phi$, measuring the correlation between the two variables, is not anymore equal to one as in the A_{FB} case. Therefore, a cancellation analogous to that one in Eq. (2.18) could not happen easily. This is another argument in favour of exploring the A_{FB} as a search variable.

2.6 The A^*_{FB} for Z' searches and diagnostics

In this Chapter it has been considered the scope of using the A^*_{FB} in the di-lepton channel for Z'-boson searches at the LHC. Such a variable has traditionally been used for diagnostic purposes in presence of a potential signal previously established through a standard resonance search via the cross section. In this respect, it has been shown that not imposing the commonly used cut on the di-lepton rapidity ($|Y_{l\bar{l}}| > 0$) would improve the A^*_{FB} discrimination between different Z' models. In addition, based on the observation that it is affected by systematics less than cross sections (being a ratio of the latter), it has been considered the possibility of using the A^*_{FB} for such a purpose for a variety of Z' models embedding either a narrow or wide resonance. In the case of narrow width Z'-bosons, it has been have proven that the statistical significance of the A^*_{FB} can be comparable with the usual bump search, for some models. In case of an early discovery at low luminosity, an A^*_{FB} measurement could indeed valuably support an evidence in the bump search which by itself could otherwise be not robust enough.

In the case of wide Z'-boson, the A^*_{FB} could have a better sensitivity than the cross section studies thanks to a more peculiar line-shape and lower systematic and PDF uncertainties. In essence the $A^*_{\rm FB}$ in specific regions of the invariant mass of the reconstructed Z'-boson could be sensitive to broad resonances much more than the cross section, wherein the broad distribution of the signal seemingly merges with the background. Further, it has been emphasised that the $A^*_{\rm FB}$ distribution mapped in di-lepton invariant mass can present features amenable to experimental investigation not only in the peak region but also significantly away from the latter.

Finally the A^*_{FB} observable benefits from the partial cancellation of the PDF's uncertainties on cross sections, being a ratio of the latter, making it much more insensitive to PDF's errors. In this sense the inclusion of the $A^*_{\rm FB}$ would definitely improve searches for wide resonances and contact interactions in the high invariant mass region where the knowledge of the predicted (differential) cross section in any particular Z' model is subject to the large-x PDF errors.

Chapter 3

Photon-Initiated production of di-lepton pairs

3.1 Photon collisions at the LHC

The upgrade in energy of the LHC to 13 TeV has opened the exploration of higher energy scales that were barred during the past Run-I. As discussed in the previous chapter, a crucial point in the search for BSM physics is the precise understanding of the behaviour of the SM background, especially in the high energy regime where one expects that new physics could appear. The LHC potential in BSM searches at the ongoing Run-II will be further boosted by the increase of the collected data sample when the luminosity will reach the project value $\mathcal{L} = 300\ \text{fb}^{-1}$. In the high luminosity phase at the LHC, the statistical errors will be greatly reduced. At the same time, the systematic effects shown in Sect. 2.5 will become more and more important. In particular PDF uncertainties are one of the major sources of theoretical systematics in hadron collisions at high energies. The errors in measured data propagate in fact into the fitted PDFs. Great improvements in this sense have been achieved recently by many PDF collaborations. The parametrisation and modelling of quarks and gluons PDFs have been significantly ameliorated by including also new high precision data from HERA and Fermilab (see Ref. [50, 51] and references therein). This has led to a reduction of the uncertainties on the d/u ratio, especially in the large-x regime ($x \geq 0.4$) closely related to the high energy scales probed in parton-parton hard scatterings.

The advantage of such an improvement easily translates into an enhanced capability of producing more accurate predictions for BSM signals and SM background at the LHC. New physics signals require an accurate determination of the SM background and uncertainties in the large-x PDFs could affect the interpretation of the LHC experiments searching for new particles at high mass scales. The bounds obtained in Chapter 2 show that the interesting invariant mass region to search for extra heavy neutral spin-1 Z'-bosons is $M_{\ell\ell} \gtrsim 3$ TeV. The simulation of events at this energy scale requires to have large values of the fraction of longitudinal proton momentum taken by the colliding quarks and antiquarks initiating the hard scattering for the Z'-boson production in the DY channel. For this reason, the improved knowledge of the quark and antiquark PDFs at large-x is extremely valuable.

With increasing the luminosity towards the LHC project value $\mathcal{L} = 300$ fb^{-1}, the statistical error will get smaller and smaller at medium-large energy scales while higher energy scales will be explored for the first time saturating the LHC potential in discovering (or excluding) new physics. For the interpretation of the experimental results that will be obtained with a very good statistical precision, it is important to have theoretical predictions with a comparable level of accuracy.

Fixed-order perturbative QCD calculations for DY production are available at NLO and NNLO accuracy, as well as EW NLO corrections for the complete di-lepton channel [52]. In order to be consistent with the partonic matrix elements, the PDF sets should have both QCD and EW corrections in the Dokshitzer-Gribov-Lipatov-Altarelli-Parisi (DGLAP) evolution kernels [53, 54]. To stay with QED effects, in addition to the corrected kernels, the QED collinear singularity leads to the need of introducing the photon distribution function which mixes with the quark (antiquark) PDFs and requires to be determined by a fit to the experimental data, like the other PDFs.

This latter element leads to a novel source of theoretical systematics, and it will be the central topic of this Chapter. One should in fact consider the Photon-Initiated (PI) lepton pair production, $pp \to \gamma\gamma + X \to l^+l^- + X$ with $l = e, \mu$. This contribution sums to the DY (differential) cross section and modifies the prediction of the SM background [3, 4, 24, 25].

The effect of PI contribution has been evaluated also in different processes, including in the context of Higgs boson measurements. In particular, it has been computed for the four-lepton final state as a background to the Higgs production where the Higgs boson decays into a Z-boson pair giving rise ultimately to four leptons in the final state [55]. Other interesting channels where the PI processes have an effects are the two-leptons and two-bosons final states [56–69]. High-energy QCD effects in the coupling of PI processes to jets, for low but finite photon virtualities, have been studied in Refs. [70–75].

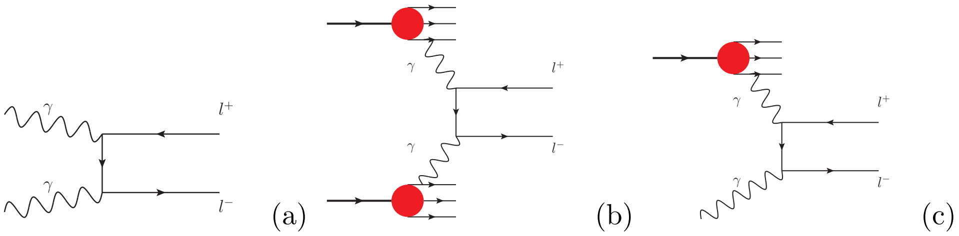

FIGURE 3.1: PI processes with (a) two real photons, (b) two virtual photons, (c) one virtual and one real photon.

3.2 Photons from QED PDFs

The PI di-lepton production mode receives contributions from three different processes, distinguished by the virtuality of the two initial photons giving rise to the $\gamma\gamma$ hard scattering. When the two photons are both considered as proton constituents, one has the so-called Double-Dissociative (DD) process. In this instance, the photon's virtuality is null so that the photon can be seen as real (resolved photon). When one photon is resolved, thus being described by a QED PDF, and the other one is emitted from a quark (antiquark) with a non-zero virtuality one has the so-called Single-Dissociative (SD) process. The last contribution represents the case when both photons are radiated off quarks (or antiquarks) and have non-zero virtuality. The Equivalent Photon Approximation (EPA), described in Ref. [76], provides a method to treat the case of non-zero virtuality. DD and SD processes require the knowledge of the QED PDFs.

Some popular sets of QED PDFs, which feature the photon as an additional parton inside the hadron, from different collaborations are: MRST2004QED [77], CT14QED [78], NNPDF3.0QED [79, 80], LUXqed [81] and xFitter_epHMDY [82], with the last three of them delivered in the LHAPDFv6 format [83]. Each PDF collaboration adopts its own procedure and assumptions in the fitting of Deep Inelastic Scattering (DIS) and possibly LHC data.

A first distinction can be made between inclusive sets, such as NNPDF3.0QED, xFitter_epHMDY, CT14QED_inc and LUXqed, where the elastic component resulting from interactions involving virtual photons is included, and inelastic sets, such as CT14QED and MRST2004QED, where the elastic component is subtracted off. A separate evaluation of the DD and SD contributions will be possible only using the latter inelastic category of QED PDFs.

Another main difference between the more recent QED PDF sets is related to the approach on the data fitting. The approach followed by the NNPDF and xFitter collaborations is based on a global fit with a large set of observables, while the approach followed

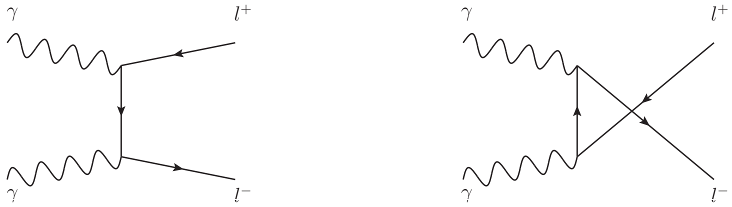

Figure 3.2: Photon Induced process contributing to the di-lepton final state.

by the LUX group consist on assuming a relation between proton structure functions and photon distributions. A more exhaustive description of each PDF collaboration procedure is available in the associated literature. It will be shown in Sec. 3.4 that the two paths lead to quite different results in terms of central values and uncertainties predicted for the PI contribution to the di-lepton channel.

Another difference on the PDF group choices concerns the delivery of the parton distribution systematic uncertainties. The LUX collaboration has implemented the Hessian procedure [48], while the NNPDF and xFitter collaborations use the replicas method [84]. The CT14QED release instead is accompanied by a table of 31 PDFs, each one obtained imposing a progressive constrain on the fraction of total momentum carried by the photon. From the analysis of the collaboration the upper bound is set to be $p_\gamma \leq 0.11\%$ at 68% CL [78]. The results obtained with this set will be extracted following this result. The MRST2004QED set does not provide any systematic uncertainty estimation.

3.3 The effect of real and virtual photons

3.3.1 Results for inelastic QED PDFs

This section discusses in more details the three PI contributions appearing in Fig. 3.1 to the di-lepton final state. The hard scattering process induced by a photon-photon collision and leading to the production of two opposite-sign leptons in the final state is mediated by the exchange of a charged lepton in the t- and u- channels. The lowest order Feynman diagrams contributing to this process are shown in Fig. 3.2. The kinematics of the photon induced scattering has been extensively studied in the literature. Its lowest order matrix element squared at parton level can easily be computed as [85]:

$$\left|\mathcal{M}(\gamma\gamma \to l^+ l^-)\right|^2 = 2e^4 \left(\frac{t}{u} + \frac{u}{t}\right), \tag{3.1}$$

where u and t are the usual Mandelstam variables and e is the electron electric charge.

Consider first the purely elastic contribution, given by two virtual photons radiated by the electro-magnetic field of the proton. Generally the EPA is used in the literature to evaluate the contribution to the di-lepton final state that comes from two initial low-virtuality photons. In the EPA, the photon flux of the proton is estimated by semi-empirical formulae built on the dipole approximation, whose parameters are fitted to the deep-inelastic electron-proton scattering data [76]. The photon induced differential cross section in the di-lepton invariant mass is obtained by multiplying the photon luminosity by the matrix element of the hard photon-photon sub-process and integrating over the phase space (for details see for example Ref. [86]):

$$\frac{d\sigma_{\text{EPA}}}{dM_{\ell\ell}} = \int dQ_1^2 \int dQ_2^2 \iint dx_1 dx_2 \frac{|\mathcal{M}(\gamma\gamma \to l^+l^-)|^2}{32\pi M_{ll}} N(x_1, Q_1^2) N(x_2, Q_2^2) \tag{3.2}$$

The integration over the virtuality of the photon Q^2 is performed between a Q^2_{min} which is determined by the kinematics, and a Q^2_{max} which is arbitrary. This is the main source of uncertainty [87]. In order to estimate this error on the EPA predictions, the Q^2_{max} parameter is spanned the interval $0.5\ \text{GeV}^2 < Q^2_{\text{max}} < 8\ \text{GeV}^2$. This implementation has been found to agree with that in Ref. [88]. The bulk of the effect comes from photons with low virtuality, while photons with a virtuality greater than 2 GeV^2 do not give an appreciable contribution.

Now consider the contribution to the di-lepton spectrum induced by two incoming real photons (DD), which can be written as:

$$\frac{d\sigma_{\text{DD}}}{dM_{\ell\ell}} = \iint dx_1 dx_2 \frac{1}{32\pi M_{\ell\ell}} \left|\mathcal{M}(\gamma\gamma \to l^+l^-)\right|^2 f_\gamma(x_1, Q) f_\gamma(x_2, Q) \tag{3.3}$$

where the function $f_\gamma(x, Q)$ is the photon PDF, the variables $x_{1,2}$ are the fraction of proton energies taken away by the two photons, Q is the factorisation scale and the observable $M_{\ell\ell}$ is the di-lepton invariant mass. The results for the DD for two choices of the factorisation scale ($Q^2 = \hat{s}$ and $Q^2 = p_T^2$) for the two inelastic PDF sets are visible in Fig. 3.3(a), in comparison with the pure DY predictions (the latter is obtained with the CTEQ6 package [34]).

Real photons extracted from the QED PDFs of one proton can interact with the low-virtuality photons of the other proton, producing a real-virtual photon hybrid interaction that is referred to as the SD contribution to the di-lepton final state. In order to estimate this term one must integrate over one EPA flux and one photon PDF:

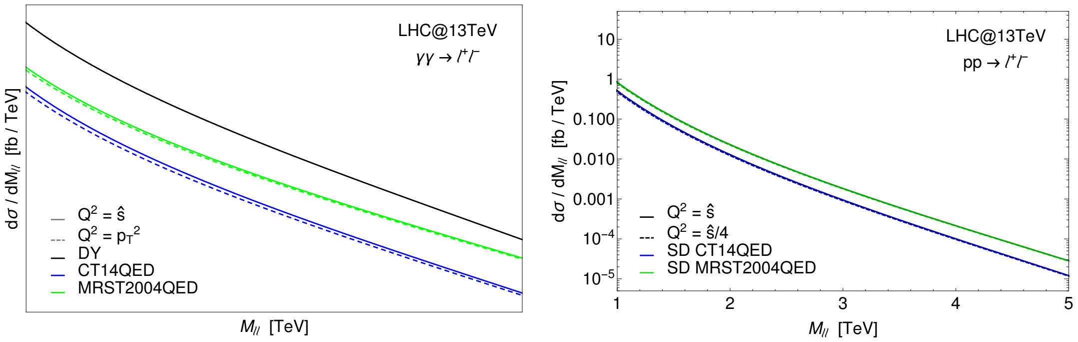

(a) (b)

Figure 3.3: (Colour online) (a) Predictions for the DD term obtained using the inelastic QED PDF sets (CT14QED, blue lines and MRST2004QED, green lines) for two choices of the factorisation scale ($Q^2 = \hat{s}$, solid lines and $Q^2 = p_T^2$, dashed lines), in comparison with the pure DY predictions (black solid line). (b) Same as (a) for the SD term and for two choices of the factorisation scale ($Q^2 = \hat{s}$, solid lines and $Q^2 = \hat{s}/4$, dashed lines).

$$\frac{d\sigma_{\mathrm{SD}}}{dM_{\ell\ell}} = \int dQ_1^2 \iint dx_1 dx_2 \frac{|\mathcal{M}(\gamma\gamma \to l^+l^-)|^2}{32\pi M_{ll}} N(x_1, Q_1^2) f_\gamma(x_2, Q) + (x_1 \leftrightarrow x_2) \qquad (3.4)$$

where Q is the factorisation scale appearing in the resolved photon PDFs, and the Q_1^2 integration is to be performed similarly to 3.2. The last sum accounts for the multiplicity of the process (virtual-real + real-virtual). The predictions for this term are of course PDF dependent and the results for the two inelastic QED PDF sets are visible in Fig. 3.3(b), for two choices of the factorisation scale ($Q^2 = \hat{s}$ and $Q^2 = \hat{s}/4$).

A more clear picture of the hierarchy of the three DD, SD and pure elastic contribution is visible in Fig. 3.4, were the shaded areas represent a first example of the PDF error bands associated with these predictions. The shaded area around the EPA curve represent the error obtained varying the $Q^2_{\max}$ in the integration of the photon spectra, as discussed above and summarised in the legend. In order to estimate the systematic error on the SD term, both the variation of $Q^2_{1,\max}$ on the contribution from the virtual photon, and the PDF error on the resolved photon are considered.

Generally the largest effect comes from the DD term, however the SD term appears not negligible in large part of the invariant mass spectrum. As visible in the inset plots in Fig. 3.4 its relative size compared with the respective DD prediction varies between 30% and 45% in the MRST2004QED set, and between 75% and 90% in the CT14QED set.

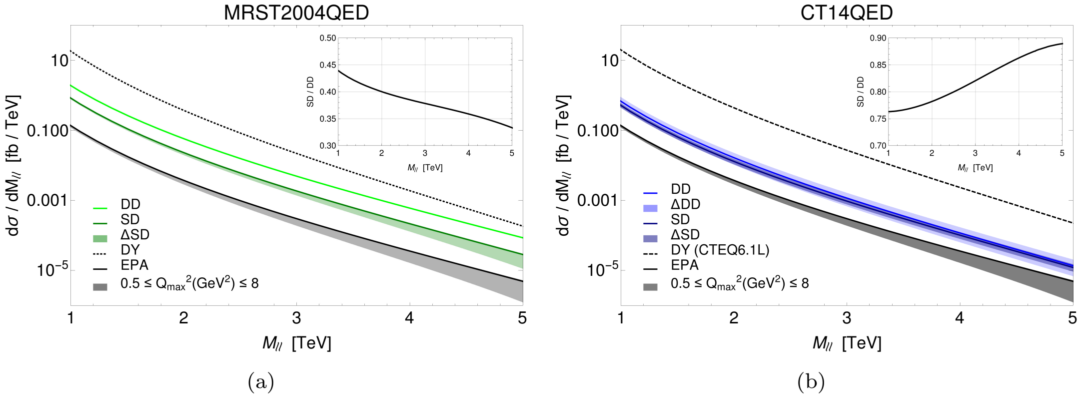

(a)

(b)

FIGURE 3.4: (a) Individual PI contributions to the di-lepton spectrum for the LHC at $\sqrt{s} = 13$ TeV, computed with the MRST2004QED PDF set. From bottom to top, are shown the contribution from two virtual photons in EPA (black solid line and shaded area), from one real and one virtual photon (SD) (darker coloured line and shaded area), and from two real photons described by QED PDFs (DD) (light coloured line and shaded area). The top black dashed line is the reference DY spectrum. The top-right inset plot shows the ratio between the SD and DD contributions as a function of the di-lepton invariant mass. (b) Same as (a) with the CT14QED PDF set. The shaded areas represent the error coming from photon PDFs and/or from the Q^2_{max} choice in EPA.

3.3.2 Results for inclusive QED PDFs

The sum of the EPA, SD and DD terms can be directly compared with the result obtained by evaluating the DD integration of Eq. (3.3) using inclusive sets, since they already combine both the elastic and inelastic components.

As first cross-check that the separation of the various terms has been done correctly, the sum of the DD, SD and EPA results obtained with the CT14QED set is compared with the inclusive result from the CT14QED_inc set. In Fig. 3.5(a) is plotted the ratio between those two results (blue line), showing that their differences are $\leq 3\%$. This ensures that double counting effects are well under control. In the same plot there is also a first comparison between two predictions for the inclusive PI results obtained with the LUXqed and the CT14QED_inc sets. The two central values are in good agreement, as their difference is always $\leq 7\%$.

In Fig. 3.5(b) the inclusive results for the PI predictions are given for the various PDF sets (coloured lines) in comparison with the DY expectations (black line). The shaded areas represent the systematic uncertainties on the PI predictions, that will be discussed more in depth in Sect. 3.4.

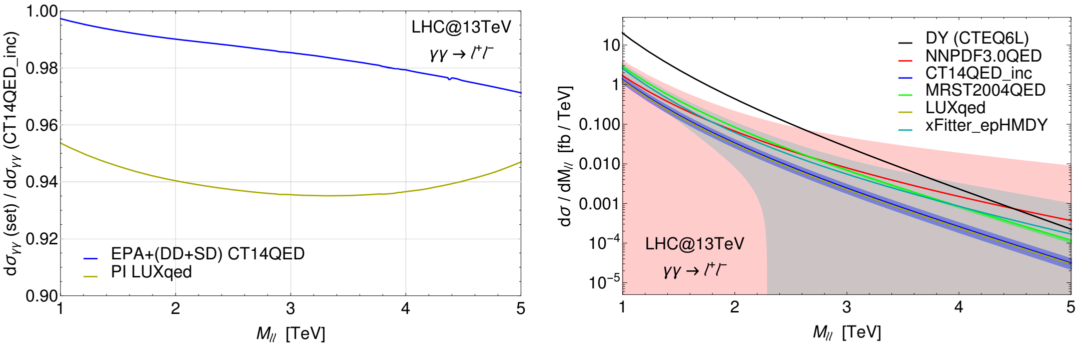

(a) (b)

FIGURE 3.5: (a) Comparison between the full PI prediction from the CT14QED_inc set and the LUXqed, and between the CT14QED_inc result and the sum of the EPA, DD and SD terms obtained with the CT14QED set. (b) Full PI prediction for different PDF sets (both inelastic and inclusive) in comparison with the pure DY term.

3.3.3 Factorisation scale and kinematical cuts

As discussed in the previous sections, when invoking the parton PDFs one has the freedom to chose an appropriate factorisation scale. Same happens when using QED PDFs and treating the resolved photon as a parton. The QCD factorisation theorem applies also to QED corrections, thus collinear PI divergences (potentially dangerous when probing high Q^2 scales) appearing as logarithms of the form $\alpha \log(Q^2/m^2)$ can be absorbed into the parton distributions functions, similarly to what happens with the collinear logarithms of perturbative QCD [77].

The choice of the factorisation scale can affect the PI predictions. This is visible in Fig. 3.6(a) where the DD result of MRST2004QED and the fully inclusive results of NNPDF3.0QED and of CT14QED_inc, are plotted for two different choices of the factorisation scale. This can be considered as a first indication of the systematic uncertainties affecting the photon PDFs. The ratio between the cross sections computed within the two factorisation frameworks is plotted in Fig. 3.6(b), revealing a first degree of uncertainty which varies between 7% and 20% along the spectrum, depending on the chosen QED PDF set.

Differently from the usual DY channel where the lepton pairs are generated by the exchange of the SM γ and Z-boson produced in s-channel, the PI processes instead involve a t, u-channel exchanges of a light lepton. The consequent collinear divergence can be regulated by introducing a cut-off. This problem is naturally solved once when considering the detector physical acceptance. Imposing the fiducial cuts as specific for the CMS detector, $|\eta_l| < 2.5$ and $p_T^l > 20$ GeV, the collinear divergence is controlled adequately.

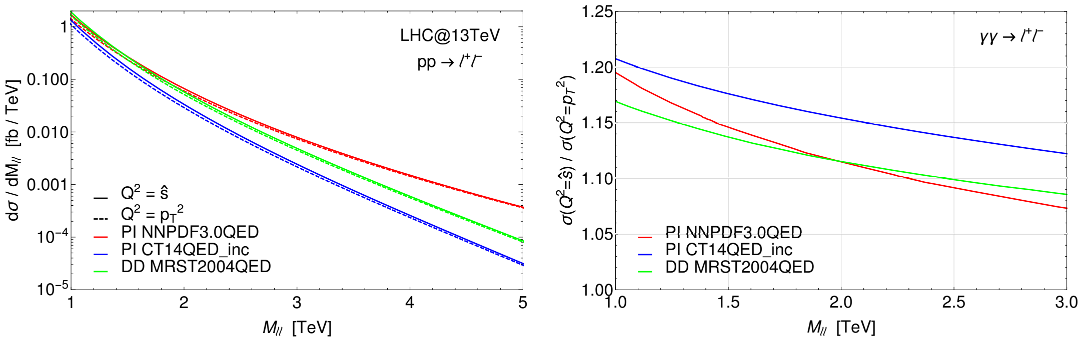

(a) (b)

Figure 3.6: (a) DD term computed with the MRST2004QED set and the fully inclusive PI result computed with the NNPDF3.0QED and CT14QED_inc sets for two different choices of the factorisation scale (solid and dashed lines). (b) Ratio between the curves in (a) for each PDF set.

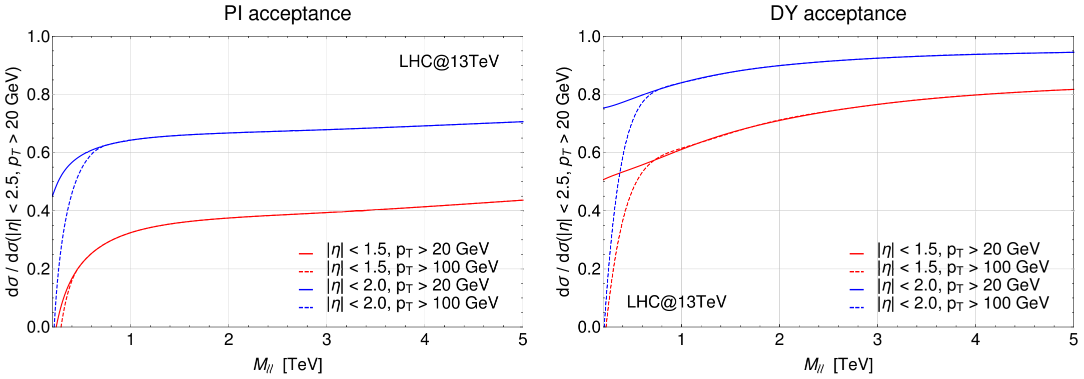

(a) (b)

Figure 3.7: (a) Acceptance of the PI contribution to the di-lepton spectrum for different cuts in η_l and p_T^l with respect to the differential cross section obtained with the standard acceptance cuts: $|\eta_l| < 2.5$ and $p_T^l > 20$ GeV. (b) Same as (a) for the DY processes.

One way to suppress the expected PI background, which can pollute BSM searches at high invariant masses, is to apply specific kinematical cuts. In particular angular and transverse momentum cuts are going to be considered here, as one expects the PI events to be produced in a more collinear region.

The effect of the η_l and p_T^l cuts are shown in Figs. 3.7(a) and 3.7(b) for the PI and DY contributions, respectively. The first one appears more sensitive to the pure angular cuts encoded in the η_l constraint. For $M_{ll} > 2$ TeV, the cut on the lepton transverse momentum is practically ineffective. Imposing an angular cut of $|\eta_l| < 1.5$ can reduce the PI effect by about 60%. The same cut decreases also the DY differential cross section by roughly 25% in the region of interest, say, $M_{ll} > 2.5$ TeV. So, despite the increasing virtuality of the fermion exchanged in the t- and u- channels, the PI process does not get suppressed much by the η_l cut with respect to the DY process.

In essence, the number of PI events can be reduced imposing stronger angular cuts, but the benefits of this might not justify the consequent loss of statistics in the DY channel as this could contain BSM physics. An alternative strategy to adopt would be to include the PI and its theoretical error in the SM background estimate.

3.4 The photon PDF uncertainty

In the previous section the variation of the factorisation scale has provided an indication of the intrinsic uncertainty on the photon PDFs. However the PDF collaborations now provide with more sophisticated procedures to estimate the uncertainty on their fits. There are two common procedures to deliver the PDF errors.

The first one is based on the Symmetric Hessian method [89]. In this case the procedure to estimate the error is slightly different compared with what shown in Sect. 2.5 for the CTEQ6 package. In this Symmetric Hessian approach the PDF error of a generic observable is estimated through a table of eigenvectors using:

$$\Delta X = \sqrt{\sum_{i=1}^{N}(X_i - X_0)^2} \tag{3.5}$$

The second common delivery of the PDF uncertainties is through the “replicas” method [84]. Once again the PDF error is provided through a large set of PDF tables, and for any observable can be estimated using:

$$\Delta X = \sqrt{\frac{1}{N}\sum_{i=1}^{N}(X_i - X_0)^2} \tag{3.6}$$

An updated revision of the PDF4LHC format with the authors recommendations for the PDF uncertainties delivery is available in [89].

The LUXqed set is delivered with a table of 100 Symmetric Hessian eigenvectors and their predictions are visible in Fig. 3.8(a). The NNPDF3.0QED and the xFitter_epHMDY sets instead are provided with a set of 100 and 600 replicas respectively and their PI spectra are plotted in Figs. 3.8(b) and 3.8(c).

The CT14QED set adopts a different approach for the estimation of the photon PDF error. The package is provided with a table of 31 PDFs, each one obtained imposing a progressive constrain on the fraction of total momentum carried by the photon. From their analysis the upper bound is set to be $p_\gamma \leq 0.11\%$ at 68% CL [78]. The error bands

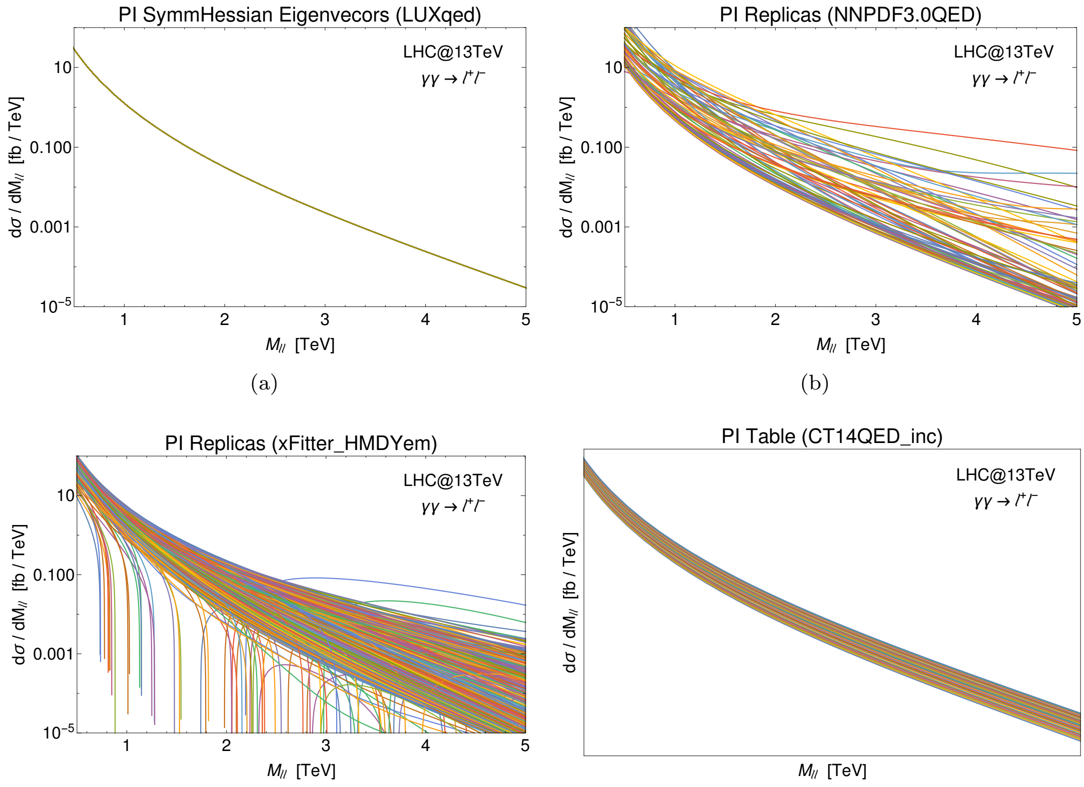

(a) (b)

(c) (d)

FIGURE 3.8: Di-lepton spectrum from PI inclusive PDF sets, respectively (a) 100 Symmetric Hessian eigenvectors of LUXqed, (b) 100 replicas of NNPDF3.0QED, (c) 600 replicas of xFitter_epHMDY, (d) 31 tables of CT14QED_inc.

showed in the previous sections for the CT14QED set have been obtained following this prescription. The predictions for the inclusive results obtained with the 31 PDFs of the CT14QED_inc set are plotted in Fig. 3.8(d).

The results obtained for the inclusive results of PI contributions is visible in Fig. 3.5(b). The central values and the photon PDF errors of each QED PDF sets, represented by the shaded areas, present various differences. The QED PDF sets obtained through a global fit approach (as NNPDF3.0QED and xFitter_epHMDY) predict a central value for the PI effects that is up to one order of magnitude above the results obtained using the QED PDF sets where more stringent constrains on the photon emissions are assumed (as LUXqed and CT14QED).

The sum of the DY and PI central values and PDF uncertainties is given in Fig. 3.9(a). Notice that the differences between the curves representing the LUXqed and CT14QED_inc results are indistinguishable at this scale, as well as the their small PDF errors. The other QED PDF sets results, due to their differences in the PI predictions, lead to some discrepancies on the shape of the distribution at high invariant masses.

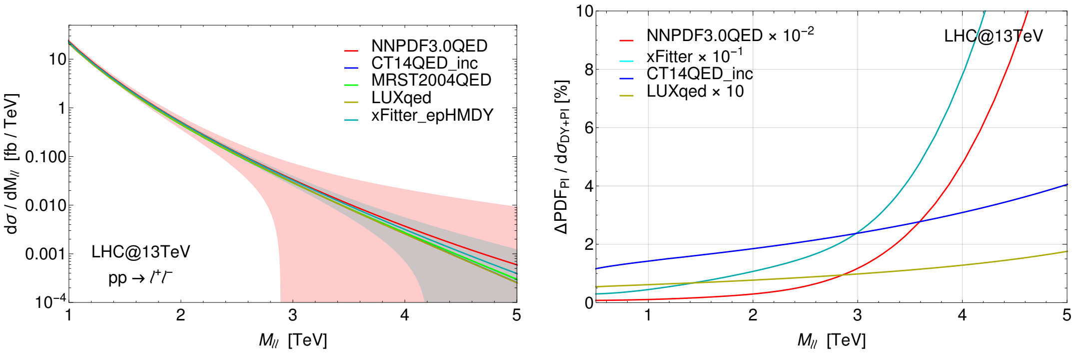

(a)

(b)

FIGURE 3.9: (a) Complete result for the di-lepton spectrum obtained summing the DY and the inclusive PI predictions for each QED PDF sets. The shaded areas represent the uncertainties coming from photon PDFs. (b) Relative size of the photon PDF error with respect to the complete di-lepton prediction for each QED PDF set. As visible in the legend an appropriate scale factor has been applied to the curves.

These discrepancies are nevertheless consistent with the predictions obtained for the systematic uncertainties. Again the results obtained with different QED PDF sets vary in a wide range. The assumptions and the constraints imposed during the fitting procedure have a strong effects in the determination of the PDF errors. In Fig. 3.9(b) is plotted the relative size of the photon PDF uncertainty with respect to the complete result, given by the sum of the DY and the inclusive PI contributions. The most optimistic results are given by the LUXqed set, where the PDF uncertainty is of the order of 0.1% along all the spectrum. On top of it there is the CT14QED_inc PDF error that is predicted to be between 1% and 4% of the complete di-lepton predictions. More conservative predictions are given by the xFitter_epHMDY set, where the photon PDF relative error is of the order of 100%, and by the NNPDF3.0QED set, where the size of the systematics reaches the dramatic value of 1000% of the central value.

Following these results, clearly the effects of the PI contribution and of its error are relevant in the cases of QED PDFs obtained following the global fit approach of the NNPDF and the xFitter collaborations. On the other hand, the assumptions and the constrains assumed in the fitting procedure adopted by the LUXqed or CT collaborations produce a lower PI central value and they also return a more precise parametrisation of the photon PDF, thus a smaller PDF uncertainty. The impressive results obtained following in particular the LUXqed approach are persuading the other PDF collaborations to adopt in their future fits the relation proposed in Ref. [81], which links the proton structure functions to the photon PDF.

3.5 Z'-boson searches and the SM background

In the previous section it has been shown that for some QED PDFs the di-lepton spectrum is dominated by systematic effects that will be mostly influential with increasing the integrated luminosity. It is evident that if one assumes the LUXqed or CT parametrisations, the PI effects would have no consequence on BSM searches. In the NNPDF and xFitter approach instead the large systematic uncertainties make the di-lepton high invariant mass region an unfriendly environment for the precise detection of new physics signals. This is the scenario that will be considered in this section, where the NNPDF3.0QED PDF set will be adopted in the analysis.

BSM searches are indeed performed simulating the SM background via a functional form whose parameters are fitted to the MC predictions. The net result is then normalized to the data in an invariant mass region, appropriately chosen, on the left-hand side of the hypothetical Z'-boson mass. The shape or slope of the DY di-lepton spectrum can be modified significantly by the PI contribution, including its error. The combined (DY + PI) background decreases less steeply with the invariant mass than the default DY, and so does the overall number of expected SM events. Once the DY and PI contributions to the di-lepton final state are added up, the overall scenario becomes more difficult to handle. The number of expected SM events and its uncertainty are shown in Fig. 3.10 before (3.10(a)) and after (3.10(b)) the inclusion of the PI process and its uncertainty. The past LHC Run-I at 8 TeV and $\mathcal{L} = 20$ fb^{-1} is considered as well as the ongoing LHC Run-II with two representative luminosities, $\mathcal{L} = 30$ fb^{-1} and $\mathcal{L} = 300$ fb^{-1}. These plots confirm that the number of SM background events is very poorly determined. For the project luminosity $\mathcal{L} = 300$ fb^{-1}, the evaluation of the pure DY contribution could lead to the conclusion that the region above $M_{ll} = 3.6$ TeV should be background free, while adding the PI contribution and its PDF error one would realize that the SM events could run over the spectrum up to $M_{ll} = 5$ TeV and beyond.

In this scenario, both the resonant search for a new heavy neutral gauge boson and the non-resonant searches for contact interactions, to cite an example, can be strongly affected by the PI contribution. In the resonant case, the incorrect estimate of the SM background events would lead to either a pre-discovery enthusiasm while in presence of a simple fluctuation or to mis-estimate the Z'-boson mass bounds.

In the non-resonant scenario one would encounter even more difficulties. The counting strategy approach described in Chapter 2, relies on the good understanding of the SM background, but as shown in the previous section, the high invariant mass region of the di-lepton spectrum is actually dominated by systematic uncertainties coming from the

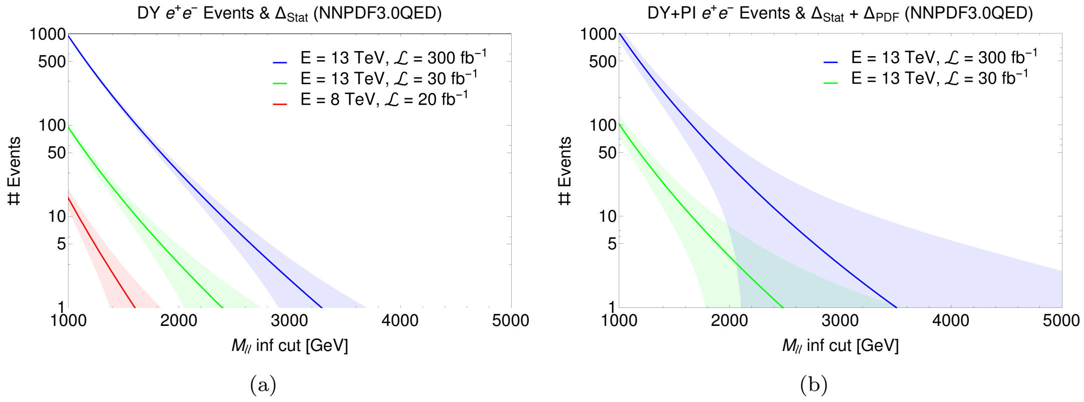

(a) (b)

FIGURE 3.10: (a) Number of SM events expected in the di-electron channel from the DY process as a function of the lower cut on the di-lepton invariant mass. The error bands include only the statistical error, as the PDF error is here sub-dominant. (b) Same result with the inclusion of the PI contribution. In the error bands is now included the overall PDF uncertainty in addiction to the statistical error. Standard acceptance cuts are applied ($|\eta_l| < 2.5$ and $p_T^l > 20$ GeV) as well as the declared efficiency of the electron channel [11]. NNLO QCD corrections are accounted for in the DY term [19].

photon PDFs. Again an excess of events can be here mis-interpreted as new physics while in presence of purely QED effects.

One can envisage two ways to keep under control this very large systematic uncertainty on the di-lepton spectrum. The first one would be implementing dedicated kinematical cuts in order to suppress the PI contribution, acting directly on the central value. This possibility has already been discussed in Sect. 3.3.3 and it has been shown that leads to a sensible reduction of the statistical sample. The second option is resorting to a different observable, more robust against systematics. A possible candidate is the A_{FB} of the final state leptons [1, 21–23, 43]. For the default DY process, initiated by quarks (antiquarks) pairs, this observable has been shown to be mildly dependent on PDF uncertainties and robust against systematic errors, in general, being a ratio of cross sections.

The following sections are focusing on how new physics signals, which might appear in these two observables, would respond to the noise coming from the PI contributions and their PDF uncertainties. Both the scenarios of narrow and wide Z'-bosons will be discussed. In particular the E6-χ model [5, 28, 90, 91] will be representative of narrow width Z'-bosons, and the GSM-SSM [44] with a large width imposed by hand will be the representative benchmark for the study of the broad resonances and contact interactions scenarios.

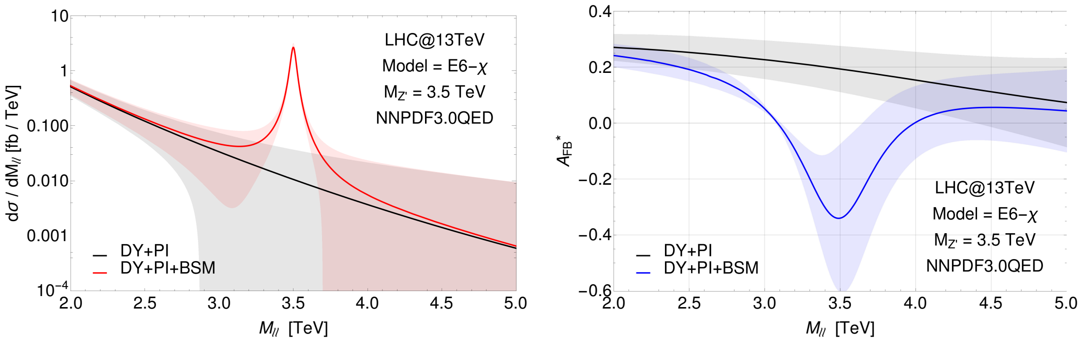

(a) (b)

FIGURE 3.11: (a) Differential cross section and (b) $A^*_{\rm FB}$ as predicted in the E6-χ model with a Z'-boson of mass $M_{Z'} = 3.5$ TeV. The black solid line represents the combined (DY + PI) background including PDFs uncertainty and the coloured lines the full contribution including the Z' signal. Standard acceptance cuts are applied ($|\eta_l| < 2.5$ and $p_T^l > 20$ GeV).

3.5.1 PI effects on narrow Z'-bosons

Consider the extra heavy Z'-boson predicted by the E6-χ model [5, 28, 90, 91], which is characterized by a narrow width. The present mass bound for this particle is $M_{Z'} \geq$ 2700 GeV [1].

The impact of the inclusion of the PI process in the SM background is shown in Fig. 3.11 where is displayed the differential cross section in the di-lepton invariant mass (3.11(a)) and the $A^*_{\rm FB}$ (3.11(b)) in the same variable for $M_{Z'} = 3.5$ TeV. The error bands in the plots represent the PDF uncertainties on the corresponding observables, dominated by the photon PDF contribution.

The sizeable uncertainty generated by the inclusion of the QED effects is evident from the plots. As expected the $A^*_{\rm FB}$ is more robust against PDF errors than the invariant mass spectrum, also in the instance of new physics. The inclusion of the PI lepton pairs and their PDF uncertainties is crucial in the estimate of the significance of the BSM signal. In Fig. 3.12 are considered the two cases where one (correctly) includes the PI contribution in the SM background, quoting its uncertainties in the overall error, (coloured lines) and where the PI events are considered as part of the new physics signal and the QED PDFs uncertainty in not included in the overall error (black lines). This comparison is shown for the the di-lepton spectrum (3.12(a)) and the $A^*_{\rm FB}$ (3.12(b)), for the luminosity $\mathcal{L} = 300$ fb^{-1} (the project luminosity that will be reached in a three years time). The significance of the observables is defined as:

$$\alpha = \frac{|S - B|}{\Delta(S + B)} \tag{3.7}$$

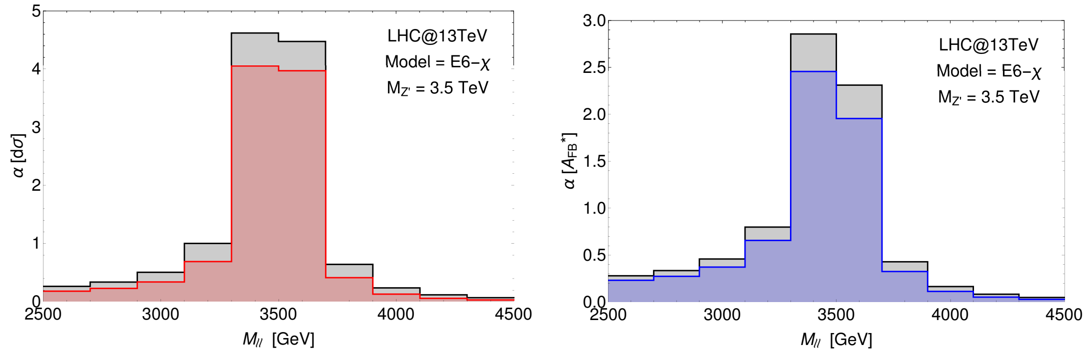

(a) (b)

FIGURE 3.12: (a) Significance of the differential cross section and (b) of the $A^*_{\rm FB}$ as predicted in the E6-χ model with a Z'-boson of mass $M_{Z'}$ = 3.5 TeV. The black line represents the case where only the default DY process is accounted for as a SM background. The coloured lines represents the case where the combined (DY + PI) process is taken into account as SM background. The integrated luminosity is $\mathcal{L} = 300$ fb^{-1}. Standard acceptance cuts are applied ($|\eta_l| < 2.5$ and $p^l_T > 20$ GeV) as well as the declared efficiencies of the electron and muon channels [11]. NNLO QCD corrections are accounted for in the DY term [19]. The overall significance is the combination of the significances in the two lepton channels. The binning has been chosen to represent an average of the two channel resolutions.

where S represents the BSM signal and B is the expected SM background. The overall uncertainty is the quadratic sum of the statistical and PDF errors, $\Delta(S+B)^2 = \Delta^2_{\rm stat} + \Delta^2_{\rm PDF}$. The PDF error has been estimated as described in Sect. 3.4, while the statistical error for the two observables is calculated as shown in Sect. 2.2.1. Even if quite basic, this estimate of the total error and consequently of the significance gives already a fair perspective of the impact of the PI contribution on the interpretation of BSM searches.

As one can see from the plots in Fig. 3.12, with increasing the luminosity the possibility of detecting a new Z'-boson at higher mass in the di-lepton spectrum would in principle grow, owing to the reduced statistical error. However, the PI contribution and its theoretical error, both increasing with the energy scale, cap this potential enhancement. In this respect, the $A^*_{\rm FB}$ has the ability to cope with the QED theoretical error much better. The PI contribution has no appreciable effect on the significance, as shown in Fig. 3.12(b). Similar results will be found in next section, where the broad resonance case will be discussed.

3.5.2 PI effects on wide Z'-bosons

As already mentioned, experimental searches for non-resonant objects in the invariant mass distribution are usually performed adopting a counting strategy approach. That means imposing a lower cut on the di-lepton invariant mass and summing over all events from there on. One thus compares the observed number of events with the theoretical

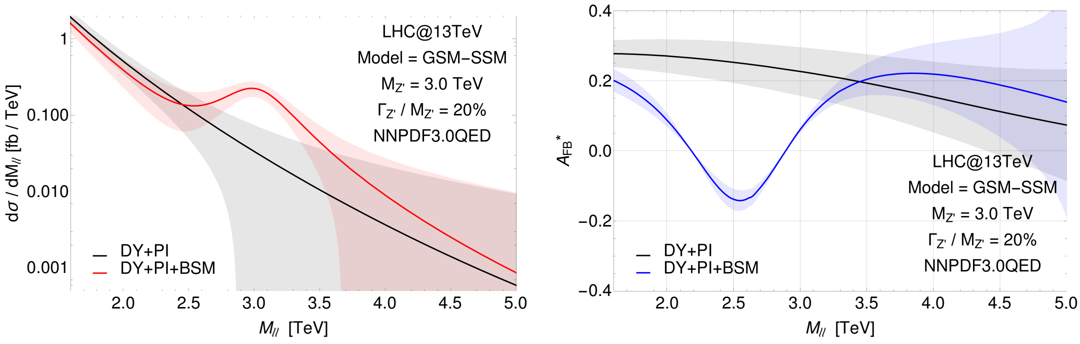

(a) (b)

FIGURE 3.13: (a) Differential cross section and (b) reconstructed Forward-Backward Asymmetry as predicted in the GSM-SSM model with a Z'-boson of mass $M_{Z'} = 3$ TeV and $\Gamma/M_{Z'} = 20\%$. The black solid line represents the combined (DY + PI) background including PDFs uncertainty and the coloured lines the full contribution including the Z' signal. Standard acceptance cuts are applied ($|\eta_l| < 2.5$ and $p_T^l > 20$ GeV).

expectation. For any meaningful interpretation of BSM searches, it is then of great importance to have a precise determination of the SM background in magnitude and shape. In this case, the photon induced di-lepton events play a major role. They indeed become relevant for $M_{ll} \geq 3$ TeV, especially when considering their PDF uncertainties.

The benchmark for the analysis of the broad Z' resonance scenario will be the wide GSM-SSM model [44] where the resonance width has been fixed at $\Gamma/M_{Z'} = 20\%$. This model indeed is often used as benchmark by the experimental collaborations.

Differential cross section and $A^*_{\rm FB}$ distribution in the di-lepton invariant mass within this model are shown in Fig. 3.13, where the error bands represent here the PDF uncertainties. In contrast to the previous narrow-width case, now the noise on the spectrum coming from the SM di-lepton production with the inclusion of QED effects is much larger. Compared to the default DY background, the full SM background coming from the combined (DY+ PI) process and depicted by the gray region around the central value (black solid line) has a sizeable different magnitude and shape. Such shape could easily fake either a broad resonance or a non-resonant type of new physics signal (like the well studied contact interactions). Once again, the $A^*_{\rm FB}$ looks much more solid in presence of QED effects and related theoretical uncertainties as shown in Fig. 3.13(b). This appears also in the estimate of the significance.

As for the previous narrow Z'-boson case, the significance of this type of BSM signal is calculated for the di-lepton spectrum and the $A^*_{\rm FB}$. The results are shown in Fig. 3.14. As before the black and the coloured lines represent the projected result of a traditional analysis and the result obtained including correctly the PI contribution in the SM background expectation and its PDF uncertainty in the total error. In Fig. 3.14(a) it is evinced that the increase in significance expected at higher luminosities for a given

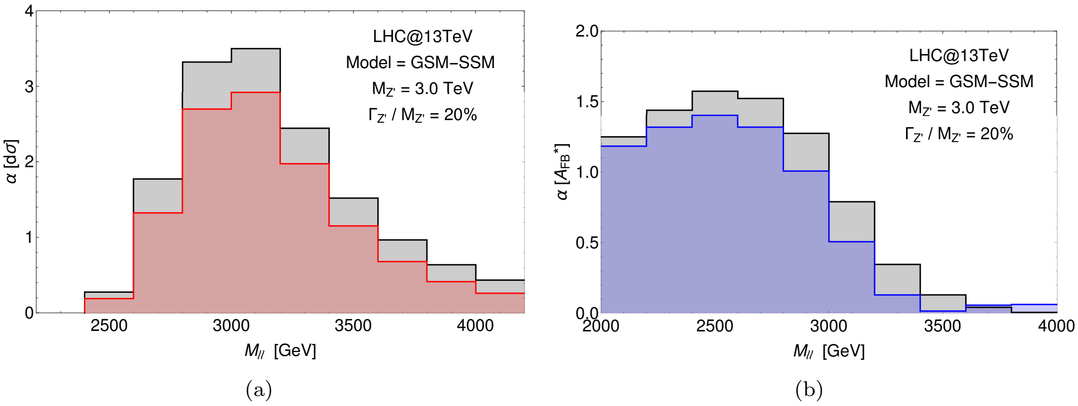

(a) (b)

FIGURE 3.14: (a) Significance of the differential cross section and (b) of the $A^*_{\rm FB}$ as predicted in the GSM-SSM model with a Z'-boson of mass $M_{Z'} = 3$ TeV and $\Gamma/M_{Z'} = 20\%$. The black line represents the case where only the default DY process is accounted for as a SM background. The coloured lines represents the case where the combined (DY + PI) process is taken into account as SM background. The integrated luminosity is $\mathcal{L} = 300$ fb^{-1}. Standard acceptance cuts are applied ($|\eta_l| < 2.5$ and $p^l_T > 20$ GeV) as well as the declared efficiencies of the electron and muon channels [11]. NNLO QCD corrections are accounted for in the DY term [19]. The overall significance is the combination of the significances in the two lepton channels. The binning has been chosen to represent an average of the two channel resolutions.

mass $M_{Z'}$ is hampered by the presence of QED effects. The situation is much cleaner for the $A^*_{\rm FB}$, which is again very mildly affected by the uncertainties on the PI contribution.

The broad resonance case shares similarities with the non-resonant case. In this instance, the theoretical interpretation of any excess of events in the di-lepton spectrum would suffer the presence of large uncertainties in the SM background estimate. The accurate knowledge of the latter is in fact limited by the QED PDF uncertainties, especially when considering the usual di-lepton spectrum as primary observable. The $A^*_{\rm FB}$ is clearly less affected by QED effects and, particularly in presence of either a broad resonance or a non-resonant type of new physics, it could help validate a possible excess of events observed in the di-lepton spectrum that would otherwise be very difficult to interpret owing to the large theoretical uncertainties.

An advisable strategy would then be working with both observables. The spectrum should be used first to detect any excess, while the $A_{\rm FB}$ should intervene in the post discovery process of interpreting the obtained experimental results.

3.6 PI effects in the LHC Run-II

The effects of PI processes to the di-lepton production channel at the LHC have been discussed in this Chapter. The contributions of the photon interactions have been obtained separating the effects of “quasi-real” and “real” photons, and they have been treated adopting the EPA and with the use of inelastic QED PDFs respectively. The central values of the PI terms has been computed using various QED PDF sets and when available the PDF uncertainties have also been estimated along following the appropriate prescriptions.

The results obtained with elastic QED PDF sets from different collaborations were compared. The central values and the PDF uncertainties obtained in the adopted scheme of each PDF release (Hessian eigenvectors, "replicas", etc.), show remarkable differences. In some cases, in particular at high invariant masses, deviations from the pure DY predictions can occur, and their size and the associated theoretical systematics, vary significantly for different photon PDFs choices.

The sensitivity of BSM searches has been investigated for both resonant and non-resonant objects, in light of the previous results, adopting the most conservative QED PDF set.

Bump searches for resonant objects that follow a peaked BW shape are not much affected by photon interactions, while counting experiments for non-resonant objects would suffer a significant loss of sensitivity. The interpretation of experimental data can be supported by introducing the $A^*_{\rm FB}$ observable, particularly because of its favourable features concerning systematic uncertainties.

Chapter 4

Constraining Z'-boson widths

4.1 The state of experimental searches

A Z' resonance can have a wide range of intrinsic widths, which depend on the scenario considered. It can be narrow, as for example, in E6, Generalised Left-Right (GLR) symmetric and Generalised Standard Model (GSM) scenarios [28], where $\Gamma_{Z'}/M_{Z'} \sim$ 0.5 - 10%. Alternatively, it can be wide, as in Technicolour [92] scenarios, Composite Higgs Models [93] or in more generic models where the Z' boson coupling to the first two fermion generations is different to that the the third generation [46, 47]. The Z' can also interact with the SM gauge bosons in presence of Z/Z' mixing [44]. In all of these cases large $\Gamma_{Z'}/M_{Z'}$ values, up to $\sim$ 50%, are induced by the additional Z' decay channels available in all such cases. As shown in Chapter 2, very wide resonances do not have a well-defined BW line-shape and appear as a broad shoulders over the SM background.

If a Z' state were to be observed at the LHC determining the intrinsic width would be an immediate objective. The width would provide information about the underlying Z' model and the coupling strength and quantum numbers of the Z' in its interactions with SM objects. The measurement of a width using the mass spectrum is limited by the detector resolution in the case of a narrow resonance and for a very wide resonance (that cannot be approximated by a BW) a model specific approach would be required.

The purpose of this chapter is to describe the role of an alternative observable to the di-lepton invariant mass (M_{ll}) that could be used to extract information on the intrinsic width of the Z'. The advantage of this approach is twofold. Firstly, one can use this new observable to determine the intrinsic width of the resonance. Secondly, the latter can potentially be used to perform a constrained fit to the cross section (or charge asymmetry) in the di-lepton invariant mass, so as to disentangle the pure signal contributions from dynamics resulting from FW and/or interference effects. This new observable is the transverse momentum distribution of an individual lepton in the final state. The corresponding (normalised) spectrum will be shown to exhibit a Focus Point (FP) that is the same for all Z' models considered, the latter thereby acting similarly to the Z' pole in the di-lepton invariant mass. One can also define asymmetries around this FP, A_{FP}s, that provide information on the underlying Z' scenario, in terms of its quantum numbers.

This is in principle analogous to the case of charge asymmetries, in practice through the FP one achieves sensitivity to a different parameter. In fact, herein, is assumed that a Z' state has already been observed and a (tentative) value of its mass has been extracted: this is a precondition for the exploitation of the FP and its asymmetries. With this mind, such FP observables provide one with an additional powerful diagnostic tool in understanding the nature of the Z', quite uncorrelated to the aforementioned cross section and charge asymmetries, as they show a strong sensitivity to its width, whichever the actual value of it. This is extremely important as, on the one hand, $\Gamma_{Z'}$ contains information about all couplings of the Z' state (hence about the underlying model) and, on the other hand, neither fits to the cross section (wherein the dependence upon $\Gamma_{Z'}$ really ought to be minimized in the search for the BW peak) nor mappings of charge asymmetries (which are primarily sensitive to the relative sign of the above couplings) offer the same scope.

4.2 The leptons transverse momentum spectra in Drell-Yan production

The analysis that will be presented in this chapter has been performed using the numerical code documented in Refs. [1, 13]. Standard acceptance cuts on the leptons have been required: $p_T > 20$ GeV and $|\eta| < 2.5$. The acceptance p_T cut is not really important since a substantial p_T^{min} cut on the leptons (> 500 GeV) will be imposed when analysing the transverse momentum distribution. In order to speed up the numerical simulation (as the focus will be on very high invariant masses, of $\mathcal{O}(1$ TeV$)$), an invariant mass cut on the simulated events is imposed ($M_{ll} > 50$ GeV).

Differential distributions for three Z' benchmark models (E6-I, GLR-LR, GSM-SSM [1]) have been generated for different Z' boson masses and widths. In computing the binned number of events, all the contributions to the same final state are included: Z' signal, SM background and their mutual interference. Higher orders corrections have not been considered in this work. Both NNLO QCD and NLO EW corrections can be large, but

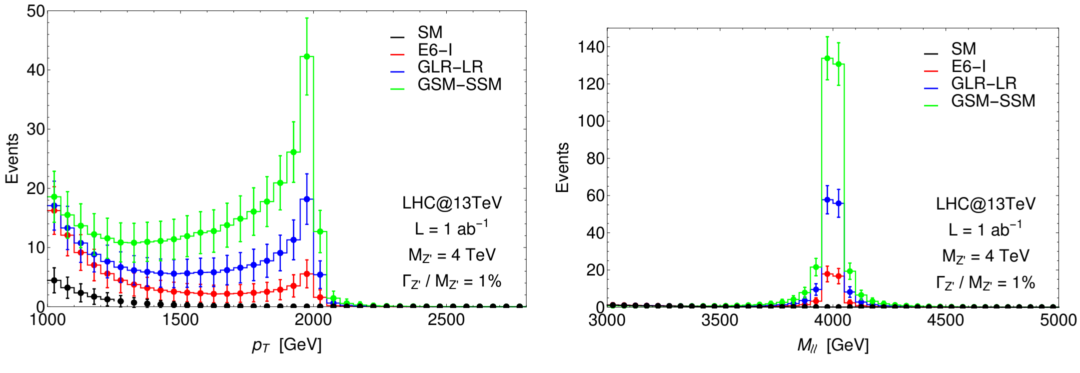

(a)

(b)

FIGURE 4.1: Distribution of number of events as function of (a) the p_T of either lepton and (b) of the di-lepton invariant mass as predicted in the SM and in three Z' benchmark models with $M_{Z'} = 4$ TeV at the 13 TeV LHC with $\mathcal{L} = 1$ ab^{-1}. For all models the width of the resonance has been fixed at 1% of its mass. Acceptance cuts are applied ($|\eta| < 2.5$), detector efficiencies are not accounted for.

they also contribute with opposite signs, leading to some cancellations [94]. However the interest is in the very high p_T region, where one can assume the NNLO QCD contribution to appear as a (roughly) constant k-factor [18]. The asymmetry observable that will be defined in the following will naturally provide a cancellation of this effect. NLO EW corrections instead are expected to grow in magnitude with the energy, and they might lead to observable effects. Yet, no public code is available at the moment for the NLO calculation of EW radiative corrections to the leptons' p_T spectra in DY production including real and virtual EW gauge boson emission, both of which are needed for an accurate estimate of the effects under analysis, owing to the fact that the di-lepton final state is treated inclusively in experimental analyses (i.e., no veto is enforced against real radiation of EW gauge bosons). Hence, for the time being, these effects will be neglected too.

In Fig. 4.1 are shown the p_T and the invariant mass distributions. The data shown have been binned by integrating in the p_T (M_{ll}) variable and multiplying by the quoted luminosity in order to obtain the number of events on the y axis. The error bars represent the statistical error on the number of events observed in each bin and are given by the square root of the number of events in each bin. As expected in the p_T distribution, a noticeable peak appears at $p_T \approx M_{Z'}/2$ for all BSM scenarios considered with the slope leading to it varying depending on the underlying Z' model. The total number of events is defined by the model cross section. The SM distribution by contrast monotonically decreases. There is no point in p_T amongst the various curves where all the differential cross sections have the same magnitude.

An interesting feature appears when the distributions are normalised. Starting from the differential distributions shown in Fig. 4.1(a) for each model in the legend, the number of

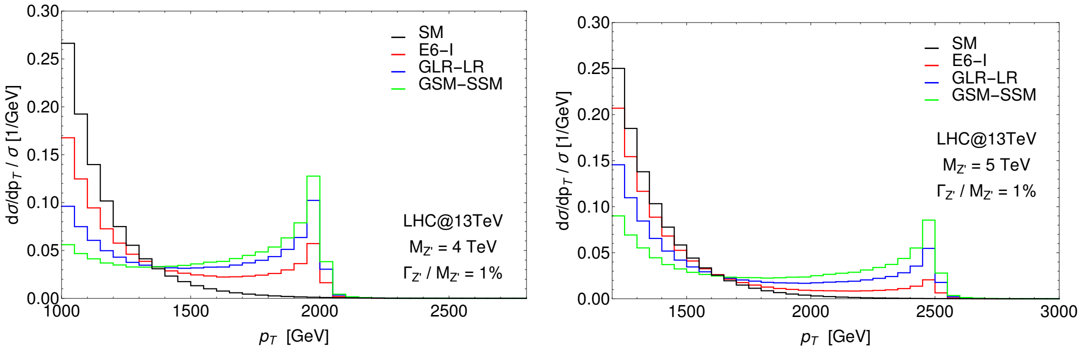

(a) (b)

FIGURE 4.2: Normalised distribution in p_T of either lepton as predicted in the SM and in three Z' benchmark models at the 13 TeV LHC. For all models the width of the resonance has been fixed at 1% of its mass. Acceptance cuts are applied ($|\eta| < 2.5$), detector efficiencies are not accounted for. (a) $p_T^{\min} = 1000$ GeV and $M_{Z'} = 4$ TeV, (b) $p_T^{\min} = 1200$ GeV and $M_{Z'} = 5$ TeV.

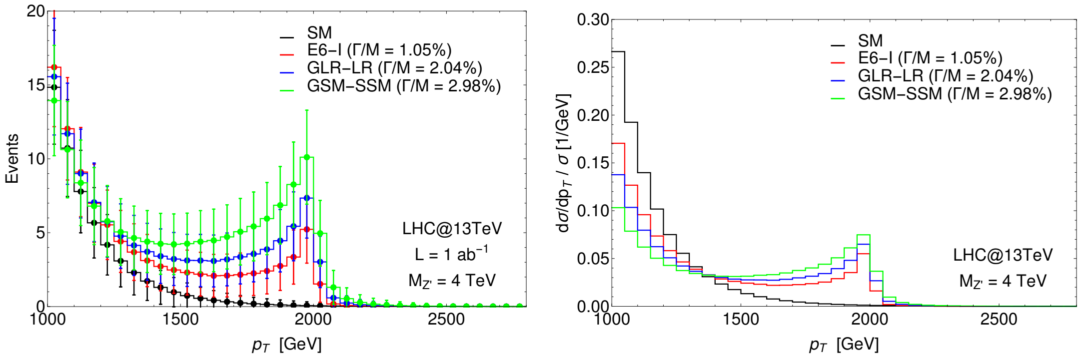

(a) (b)

FIGURE 4.3: (a) Number of events as function of p_T of either lepton as predicted in the SM and in three Z' benchmark models with $M_{Z'} = 4$ TeV at the 13 TeV LHC with $\mathcal{L} = 1\ ab^{-1}$. The width of the resonances has been fixed at their natural value as predicted by the model. Acceptance cuts are applied ($|\eta| < 2.5$), no detector efficiencies are accounted for. (b) Normalized distribution of (a) with $p_T^{\min} = 1000$ GeV.

events in each bin is divided by the total number of events that is obtained integrating the cross section from the chosen $p_T^{\min}$ on. For this specific case $p_T^{\min} = 1000$ GeV is chosen. The results of this normalisation are shown in Fig. 4.2(a). The most interesting feature in this plot is that around $p_T = 1400$ GeV all the curves have the same magnitude. This intersection point is defined as the FP. The FP position strongly depends on the lepton $p_T^{\min}$ cut that is chosen to maximise the sensitivity to the hypothetical Z' boson. This will be discussed more extensively in Sect. 4.4.2. For a Z' mass of 5 TeV the optimal choice is $p_T^{\min} = 1200$ GeV. In this case a very similar behaviour is obtained, albeit with the FP shifted to around 1.7 TeV, as plotted in Fig. 4.2(b). In these illustrations the LHC energy has been taken to be 13 TeV and the CT14NNLO PDF set [95] has been used with the factorisation scale fixed at $Q = \sqrt{\hat{s}}$.

For completeness in Fig. 4.3 are shown the distributions for the number of events and the normalized p_T for the three benchmark models with the resonance widths fixed to the natural values predicted by each model. The values for the resonance widths can be significantly modified by the presence of new physics, therefore in order to be as general as possible the Z' width will be considered to be a free parameter.

In order to understand this feature in detail, in the following section will be discussed its dependence upon the collider energy, the Z' parameters (its mass and width), the minimum p_T cut and the normalisation procedure as well as the role of the interference between the Z' diagram and SM topologies. The independence upon the choice of PDFs and Q will not be discussed, but it comes straightforward considering that the quark and antiquark behaviour inside the proton at the relevant x and Q values is well determined [3].

4.3 Properties of the Focus Point

The presence of a FP in the leptons p_T distribution after the normalisation procedure described above, appears to be a very general feature. So general that also the SM predictions, which do not feature any peaked structure, are crossing the FP, as well as any other single-Z' model. However the position of the FP is affected by other parameters, as will be discussed in this section.

First thing to notice is that the FP is found to be is sensitive to the partonic (or collider) energy. Fig. 4.4 (where again is assumed $\Gamma_{Z'}/M_{Z'} = 1\%$) illustrates that the FP also appears at 8 TeV for different models and Z' masses considered. However the position of the FP is not the same as the 13 TeV case, but still it maintains its model independence feature.

The FP position is also very marginally affected by interference effects. In Fig. 4.5(a) is plotted the same distribution as in Fig. 4.2 where, the histograms shown with a dashed line correspond to the case where the interference interaction terms (between the Z' diagram and the $\gamma + Z$ ones) have been switched off in the MC event generator. Clearly the contribution of the interference is negligible and it does not affect the position of the FP.

The same result is visible in Fig. 4.5(b) where the dashed lines now represent the Z' signal only, which has been determined by subtracting the SM background and its interference with the BSM signal. The presence and the position of the FP are once more unaffected by these changes: all the curves, representing either the full model or the pure

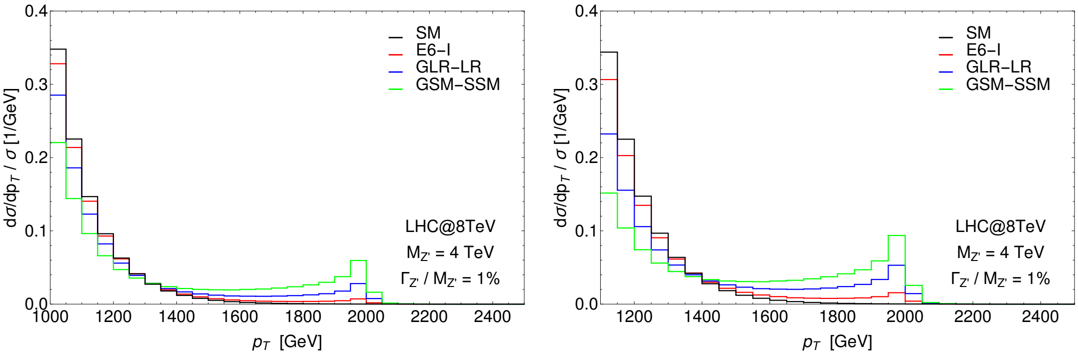

(a)

(b)

FIGURE 4.4: Normalised distribution in p_T of either lepton as predicted in the SM and in three Z' benchmark models at the 8 TeV LHC. For all models the width of the resonance has been fixed at 1% of its mass. Acceptance cuts are applied ($|\eta| < 2.5$), detector efficiencies are not accounted for. (a) $p_T^{\min} = 1000$ GeV and $M_{Z'} = 4$ TeV, (b) $p_T^{\min} = 1100$ GeV and $M_{Z'} = 4$ TeV.

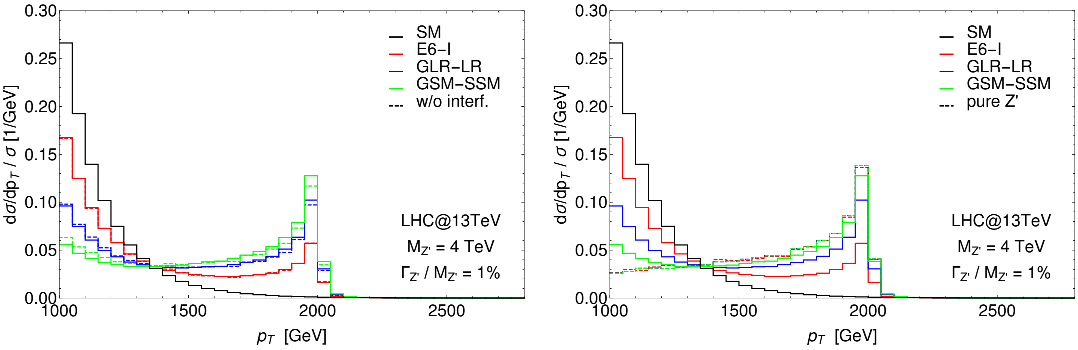

(a)

(b)

FIGURE 4.5: As in Fig. 4.2(a) with dashed lines representing (a) the case without the interference terms between the BSM and SM diagrams, and (b) the case of the pure Z' signal.

Z' contribution, cross at the same point, demonstrating the stability of the FP manifestation. In definitive, the FP position shows very little dependence on interference effects, further illustrating the model independent nature of this result.

It is clear that one of the main parameters that defines the position of the FP is the Z' resonance mass. The effect of varying the Z' mass is shown in the normalised p_T distributions of Fig. 4.6. The SSM benchmark model is used here and the width is fixed at $\Gamma_{Z'}/M_{Z'} = 1\%$. As visible, the position of the FP does depend on Z' the mass.

The other main parameter affecting the FP position is, the choice of the low p_T integration limit, which determines the curves' normalisation factor. As shown in Fig. 4.7 the FP changes depending on the chosen low p_T integration limit. The two different p_T choices in this figure can also be compared with the one in Fig. 4.4(a), where $p_T > 1000$ GeV was chosen.

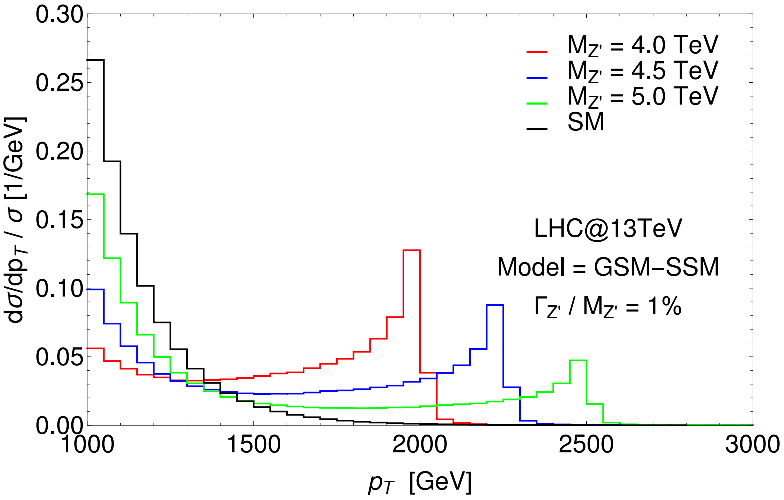

FIGURE 4.6: Normalised distribution in p_T of either lepton as predicted in the SM and in in the SSM at the 13 TeV LHC. The mass of the resonances has been fixed at three different values (4.0, 4.5 and 5.0 TeV) while its width has been fixed at 1% of its mass. Acceptance cuts are applied ($|\eta| < 2.5$), detector efficiencies are not accounted for.

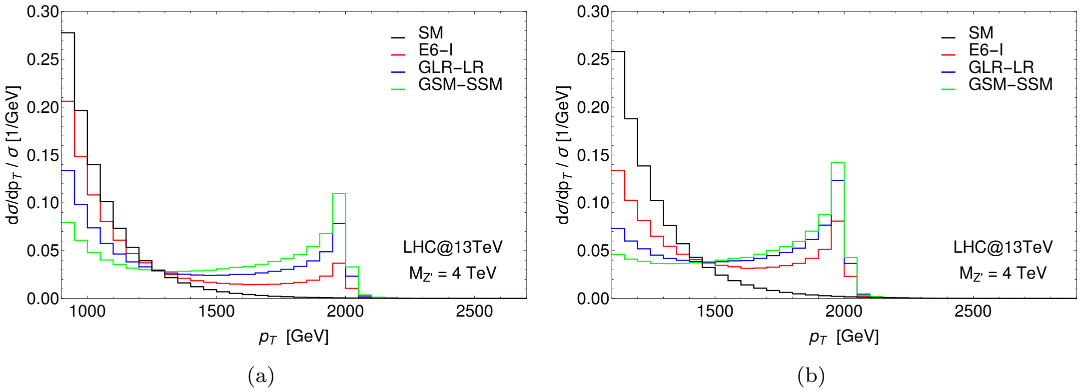

(a)

(b)

FIGURE 4.7: Normalised distribution in p_T of either lepton as predicted in the SM and in three Z' benchmark models with $M_{Z'} = 4$ TeV at the 13 TeV LHC. For all models the width of the resonance has been fixed at 1% of its mass. Acceptance cuts are applied ($|\eta| < 2.5$), detector efficiencies are not accounted for. (a) $p_T^{\text{min}} = 900$ GeV, (b) $p_T^{\text{min}} = 1100$ GeV.

A correlation can be established between the FP location (for a given Z' mass and LHC energy) and the p_T^{min} cut used for the normalisation procedure. Empirically the position of the FP follows a simple linear relation $FP = p_T^{\text{min}} + 10\% M_{Z'}$ which is valid at the 13 TeV LHC.

Lastly, the most interesting feature of the FP is represented by its behaviour under variation of the resonance width. For this purpose, one specific benchmark will be considered, since similar results can be obtained in the other models. In Fig. 4.8 is plotted the binned distributions of the number of events as function of the lepton p_T (4.8(a)) and of the di-lepton system invariant mass (4.8(b)) for the GSM-SSM model and different choices of the resonance width (1%, 5%, 10% and 20% of the mass) keeping

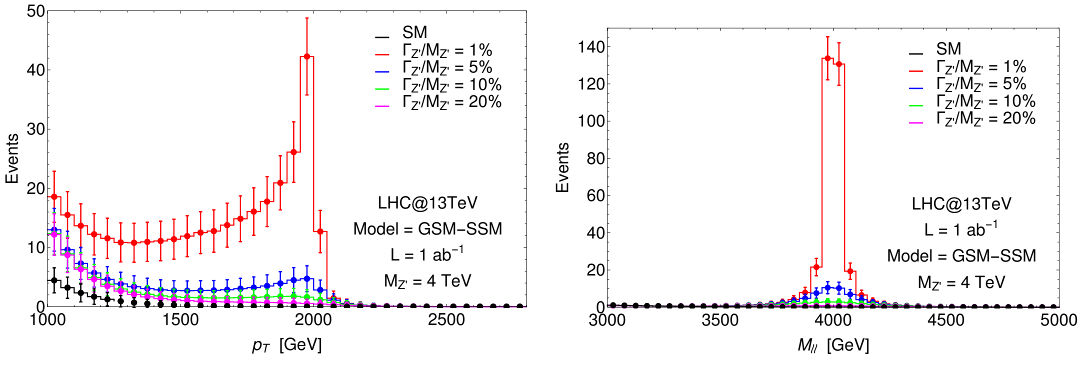

(a) (b)

FIGURE 4.8: Distribution of number of events as function of (a) the p_T of either lepton and (b) of the di-lepton invariant mass as predicted in the SM and in the GSM-SSM with $M_{Z'} = 4$ TeV at the 13 TeV LHC with $\mathcal{L} = 1$ ab^{-1}. The width of the resonances has been fixed at four different values (1%, 5%, 10% and 20% of the mass). Acceptance cuts are applied ($|\eta| < 2.5$), no detector efficiencies are accounted for.

the mass of the resonance fixed at 4 TeV. In this analysis the width of the resonance has been enhanced by hand, that is the production cross section is unchanged, as well as the partial widths into the SM final states. The branching ratios however scales inversely with the width. This is representative of a scenario where extra decay channels are accessible to the neutral resonance, which is a very common picture in many BSM realisations predicting exotic matter.

As one can notice, the invariant mass distribution in Fig. 4.8(b) the loss of sensitivity due to the width enhancement is substantial. Even for relatively low Z' masses (4 TeV in this example), it looks difficult to perform significant measurements on resonances with $\Gamma_{Z'}/M_{Z'}$ >5%. On the other hand, if one considers the p_T distribution of either lepton, the different curves in Fig. 4.8(a) are distinguishable even for $\Gamma_{Z'}/M_{Z'} > 10\%$.

After the normalisation procedure, the FP appears again as a common crossing point of all the curves, representing different choices for $\Gamma_{Z'}/M_{Z'}$. This is shown in Fig. 4.9 where the position of the FP do not depend on the resonance width. This is the key feature that is exploited to define a new observable that can be used to constrain the resonance width.

4.4 Exploiting the Focus Point features

This section will show how the value of the intrinsic Z' width can be inferred from the use of a novel asymmetry observable based upon the concept of the FP, which was discussed in the previous sections.

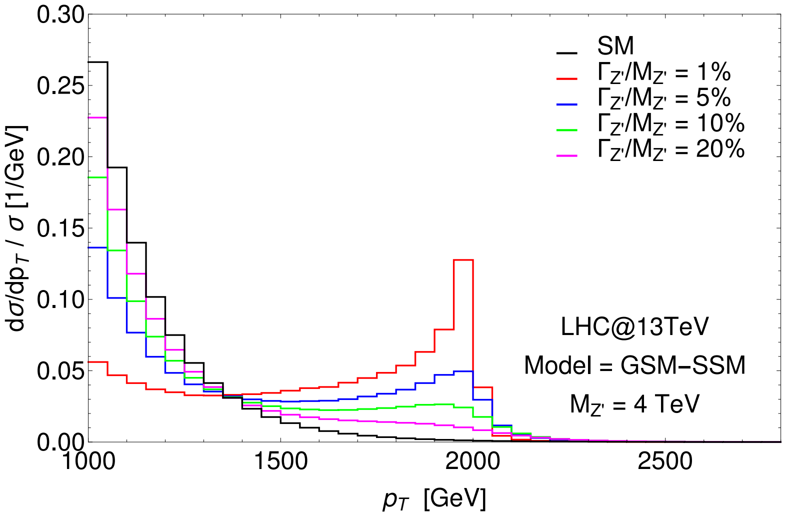

FIGURE 4.9: Normalized distribution obtained from Fig. 4.8(a) with $p_T^{\min} = 1000\ GeV$.

4.4.1 Defining a new observable: A_{FP}

For a given collider energy and Z' mass, suitably normalised single-lepton p_T distributions for various Z' models all have the same magnitude at one point in the spectrum, that is the FP. The p_T value associated with it has been shown to not depend upon the intrinsic Z' width, in any of the models. For a fixed collider energy and a given Z' mass therefore, it is possible to define a unique FP that is common to a large class of models.

In order to define an observable based on the FP feature that can provide information about the width of the resonance, let's define two separate regions in the normalised p_T distribution. The "Left" (L) region going from the fixed $p_T^{\min}$ (the low p_T limit referred to above) up to the FP and the "Right" (R) region going from the FP up to the last point in the distribution, which is assumed to be $p_T^{\max} > M_{Z'}/2$.

The Asymmetry around the Focus Point (A_{FP}) is defined as the difference between the integrated normalised distribution in the two regions, divided by the sum of the two integrations. This can be written

$$A_{\text{FP}} = \frac{L - R}{L + R} \tag{4.1}$$

with

$$L = \frac{1}{N}\int_L \frac{d\sigma}{dp_T} dp_T, \qquad R = \frac{1}{N}\int_R \frac{d\sigma}{dp_T} dp_T, \tag{4.2}$$

where the two domains L and R are chosen as described above, i.e., $L = \left[p_T^{\min}, \text{FP}\right]$, $R = [\text{FP}, p_T^{\max}]$, FP is the FP position in the p_T axis, and N is the total number of events in the $(L + R)$ region that has been used in the normalization. The expression derived for the new observable is notionally very similar to the Forward-Backward Asymmetry

($A_{\rm FB}$) [1, 21, 23]. In this sense, the formula for the statistical error on the $A_{\rm FP}$ observable is analogous to the one for the $A_{\rm FB}$:

$$\Delta A_{\rm FP} = \sqrt{\frac{1 - A_{\rm FP}^2}{N}}, \tag{4.3}$$

This $A_{\rm FP}$ observable can be used to estimate the width of the Z' resonance, with the positive feature of being unbiased by systematics and assumptions intrinsic to shape dependent fitting procedures (such as assuming a BW resonance structure in the di-lepton invariant mass spectrum).

In the following, the $A_{\rm FP}$ values for different Z' model and width choices will be estimated in the 13 TeV LHC setup and for various Z' masses. At this point, it is important to mention that the definition of the L and R regions is crucial for a correct analysis of the results. The precise steps to follow are: (i) extraction of the mass of the resonance from the di-lepton invariant mass, possibly combined with the location of the maximum of the p_T distribution (which roughly coincides with $M_{Z'}/2$); (ii) definition of the FP according to:

$$FP = p_T^{\rm min} + 10\% M_{Z'}. \tag{4.4}$$

While $p_T^{\rm max}$ is essentially defined to be any point in transverse momentum past $M_{Z'}/2$ (as seen in the p_T distributions the drop beyond this point is dramatic), there is some freedom in the choice of $p_T^{\rm min}$. For example, a high $p_T^{\rm min}$ would maximise the sensitivity to any BSM physics while a low $p_T^{\rm min}$ would maximise the sensitivity to different BSM scenarios. As discovery of some BSM physics is assumed to have already occurred from the analysis of the M_{ll} spectrum, for our purposes a low $p_T^{\rm min}$ is indeed more appropriate.

In Tabs. 4.1–4.2 the calculated $A_{\rm FP}$ observable for the SM background and for the usual benchmark models is calculated for different widths assumptions. Two values for the Z' mass are considered ($M_{Z'} = 4$ TeV and $M_{Z'} = 5$ TeV) and three possible choices for the $p_T^{\rm min}$ for each mass. As expected, moving up the $p_T^{\rm min}$ (and consequently the FP location), the sensitivity to the presence of BSM physics increases, while going in the opposite direction leads to an enhancement of the sensitivity on the Z' boson width.

The statistical errors are also reported in the two tables and they are obtained for an integrated luminosity of 1 and 3 ab^{-1} respectively. The statistical error represents the dominant uncertainty in the $A_{\rm FP}$ observable. Being a ratio of cross sections systematic uncertainties are indeed expected to cancel partially. Below are given two examples of the expected size of the PDF uncertainty, to compare with the central value and the statistical error taken from Tab. 4.2.

$$M_{Z'} = 5 \text{ TeV}, \ \Gamma_{Z'}/M_{Z'} = 5\%, \ p_T^{\min} = 1.2 \text{ TeV}, \tag{4.5}$$

$$(A_{\text{FP}} \pm \Delta_{\text{stat}} \pm \Delta_{\text{PDF}})_{\text{SM}} = 0.87 \pm 0.07 \pm 0.01, \tag{4.6}$$

$$(A_{\text{FP}} \pm \Delta_{\text{stat}} \pm \Delta_{\text{PDF}})_{\text{SSM}} = 0.44 \pm 0.12 \pm 0.06. \tag{4.7}$$

$M_{Z'} = 4$ TeV				
Model	$\Gamma_{Z'}/M_{Z'} = 1\%$	$\Gamma_{Z'}/M_{Z'} = 5\%$	$\Gamma_{Z'}/M_{Z'} = 10\%$	$\Gamma_{Z'}/M_{Z'} = 20\%$
$p_T^{\min} = 900$ GeV				
SM	0.82±0.05			
E6-I	0.44±0.07	0.72±0.06	0.77±0.06	0.80±0.06
LR	0.02±0.07	0.55±0.07	0.68±0.07	0.76±0.06
SSM	-0.29±0.05	0.26±0.08	0.50±0.08	0.67±0.07
$p_T^{\min} = 1000$ GeV				
SM	0.81±0.08			
E6-I	0.27±0.10	0.65±0.09	0.72±0.09	0.77±0.08
LR	-0.14±0.07	0.40±0.10	0.58±0.10	0.70±0.09
SSM	-0.37±0.05	0.06±0.10	0.33±0.12	0.56±0.11
$p_T^{\min} = 1100$ GeV				
SM	0.79±0.11			
E6-I	0.12±0.12	0.57±0.13	0.68±0.12	0.74±0.12
LR	-0.22±0.08	0.25±0.14	0.47±0.14	0.64±0.13
SSM	-0.38±0.05	-0.08±0.12	0.16±0.15	0.43±0.16

TABLE 4.1: A_{FP} and its statistical error for the SM and three benchmark models with $M_{Z'} = 4$ TeV and four different widths repeated for three choices of $p_T^{\min}$, for the LHC at 13 TeV and $\mathcal{L} = 1$ ab^{-1}. The FP position is obtained following Eq. 4.4.

4.4.2 Sensitivity of the A_{FP} observable

In this section will be explored in more detail the potential of the new A_{FP} observable in discriminating amongst different Z' models and amongst different widths. First consider BSM scenarios within the same class, as shown in Fig. 4.10, where the usual normalised p_T distributions are plotted.

The distributions of the models in the E6 class present clear similarities and the same behaviour is shown in the models belonging to the GLR class. In this sense the A_{FP} can potentially discriminate between the main classes of models, but cannot disentangle the specific model within each class. In Fig. 4.11, the A_{FP} and its statistical error (as

$M_{Z'} = 5$ TeV				
Model	$\Gamma_{Z'}/M_{Z'} = 1\%$	$\Gamma_{Z'}/M_{Z'} = 5\%$	$\Gamma_{Z'}/M_{Z'} = 10\%$	$\Gamma_{Z'}/M_{Z'} = 20\%$
$p_T^{\rm min} = 1100$ GeV				
SM	0.88±0.05			
E6-I	0.71±0.07	0.84±0.06	0.85±0.05	0.87±0.05
LR	0.40±0.08	0.76±0.07	0.82±0.06	0.85±0.06
SSM	0.04±0.08	0.60±0.08	0.74±0.07	0.82±0.06
$p_T^{\rm min} = 1200$ GeV				
SM	0.87±0.07			
E6-I	0.62±0.10	0.81±0.08	0.84±0.07	0.85±0.07
LR	0.22±0.10	0.68± 0.10	0.77±0.09	0.83±0.08
SSM	-0.14±0.09	0.44±0.12	0.64±0.11	0.77±0.10
$p_T^{\rm min} = 1300$ GeV				
SM	0.86±0.09			
E6-I	0.50±0.14	0.77±0.11	0.81±0.10	0.84±0.10
LR	0.06±0.12	0.58±0.14	0.72±0.13	0.80±0.11
SSM	-0.24±0.09	0.27±0.16	0.52±0.16	0.70±0.14

TABLE 4.2: $A_{\rm FP}$ and its statistical error for the SM and three benchmark models with $M_{Z'} = 5$ TeV and four different widths repeated for three choices of $p_T^{\rm min}$, for the LHC at 13 TeV and $\mathcal{L} = 3$ ab^{-1}. The FP position is obtained following Eq. 4.4.

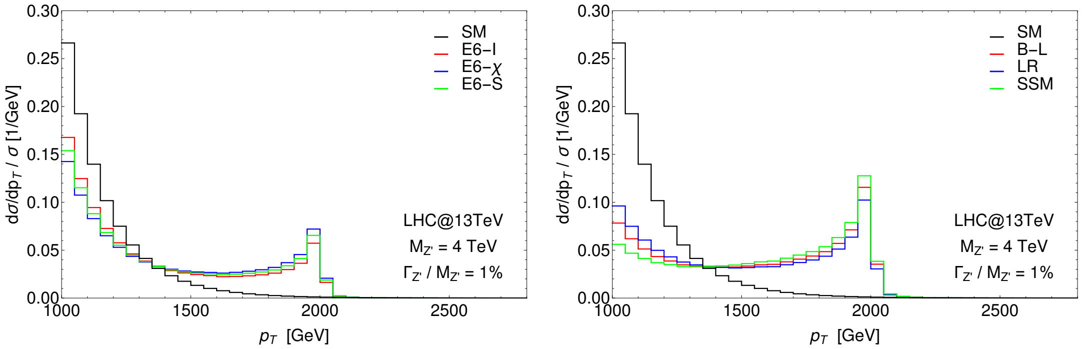

(a) (b)

FIGURE 4.10: Normalised distribution in p_T of either lepton as predicted in the SM (black) and in three Z' benchmark models (coloured) within the E6 class ((a)) and GLR and GSM classes ((b)) with $M_{Z'} = 4$ TeV and $p_T^{\rm min} = 1000$ GeV. The width of the resonances has been fixed at 1% of their mass. Acceptance cuts are applied ($|\eta| < 2.5$), no detector efficiencies are accounted for. Here, $\sqrt{s} = 13$ TeV.

predicted for an integrated luminosity $\mathcal{L} = 1$ ab^{-1}) are shown as function of the $p_T^{\rm min}$ cut for different models within each class.

As expected, Z' models in the same class have similar values for $A_{\rm FP}$, all falling within the error bars already for Z' masses of 4 TeV and narrow resonances. This is definitely true for benchmarks in the E6 class and a similar behaviour is shown for two GLR benchmarks as well (GLR-LR and GLR-B-L). However, as the resonance mass or width increases, the differences between models tend to disappear. This, in essence, suggests

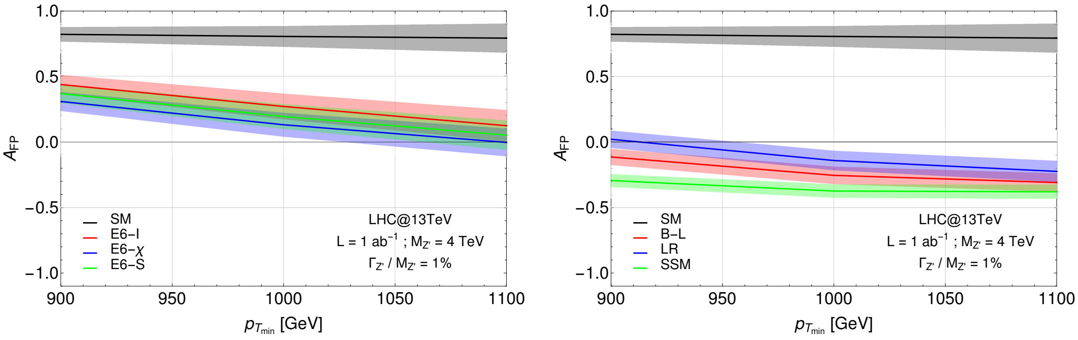

(a) (b)

FIGURE 4.11: A_{FP} central value and statistical 1σ error band as function of p_T^{min} for the LHC at 13 TeV and $\mathcal{L} = 1$ ab^{-1}. The black line represents the SM while the coloured lines represent three benchmark in the E6 class (a) and GLR and GSM classes (b). The mass of the Z' boson is fixed at 4 TeV and its width has been fixed $\Gamma/M = 1\%$. The values for the FPs are chosen in accordance to Tab. 4.1.

that this observable cannot be used to discriminate between models within the same class.

Still, the discriminative power of A_{FP} against the SM background and amongst classes of models can be exploited, ultimately extracting constraints that can be imposed on the resonance width. In Figs. 4.12–4.13 the predictions for the A_{FP} and its statistical error as a function of p_T^{min} are shown for the SM and for the three Z' benchmarks representative of each class of models. The results are shown fixing different widths, as visible in the legends, and for two values of the Z' mass ($M_{Z'} = 4$ - 5 TeV). As visible in Fig. 4.12, for a Z' boson mass around 4 TeV, the A_{FP} observable can distinguish between different models having $\Gamma_{Z'}/M_{Z'} \sim 10\%$ and in some cases up to 20% too. For a resonance mass around 5 TeV (Fig. 4.13) instead, the sensitivity upon the different classes of models holds up to $\Gamma_{Z'}/M_{Z'} \sim 5\%$.

Coming back to the original purpose, the sensitivity of A_{FP} upon the resonance width is now discussed. In Figs. 4.14 the A_{FP} discriminative power is shown against the resonance width within each class for two choices of the Z' boson mass. The A_{FP} observable seems to fulfil the task: within each class of models it is possible to set important constraints on the resonance width. In the case of resonances of the order of 4 TeV, exploiting 1 ab^{-1} of integrated luminosity, one would be able to constrain Z' widths up to $\Gamma_{Z'}/M_{Z'} \sim 10\%$ within the E6 class of models and up to $\Gamma_{Z'}/M_{Z'} \sim 20\%$ within the other classes. For resonances of the order of 5 TeV similar results are obtained, assuming an integrated luminosity of 3 ab^{-1}.

In summary, the new kinematic asymmetry A_{FP}, based around the FP appearing in the normalised transverse momentum distribution of either lepton in DY processes, has quite remarkable features, as it is sensitive on the width of the Z'-boson in a wide range.

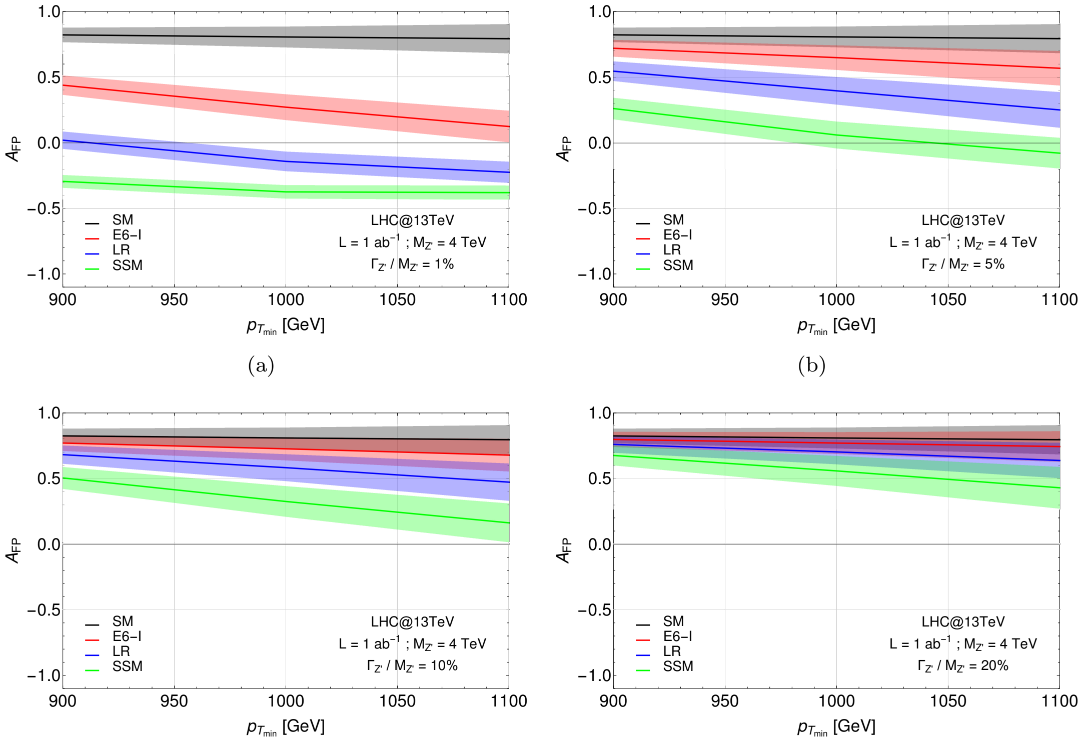

(a) (b)

(c) (d)

FIGURE 4.12: A_{FP} central value and statistical 1σ error band as function of p_T^{min} cut for the LHC at 13 TeV and $\mathcal{L} = 1$ ab^{-1}. The black line represents the SM while the coloured lines represent the three benchmark models. The mass of the Z' boson is fixed at 4 TeV while its width over mass ratio $\Gamma_{Z'}/M_{Z'}$ has been fixed to 1% (a), 5% (b), 10% (c) and 20% (d). The values for the FP are chosen in accordance to Tab. 4.1.

This makes the A_{FP} a suitable observable for the analysis of any Z' resonance which may be discovered at the LHC. Furthermore it could also be used to put constrains in the possible range of widths of a Z' signal. This information can be imported in experimental analysis to significantly improve the fit of a resonance peak in the invariant mass spectrum.

4.5 The A_{FP} for Z' searches and diagnostics

In this Chapter is has been shown how the analysis of the transverse momentum distribution of either lepton in DY processes can be used in BSM searches for the detection and the diagnosis of resonant Z' decays. In particular, after a simple normalisation procedure, the appearance of a FP can be exploited together with the model independent features of the latter, such that a new kinematic asymmetry, the A_{FP}, is defined.

The most remarkable features of the FP are its insensitivity to the underlying Z' model as well as quantities which carry (theoretical) systematic errors such as PDFs and their

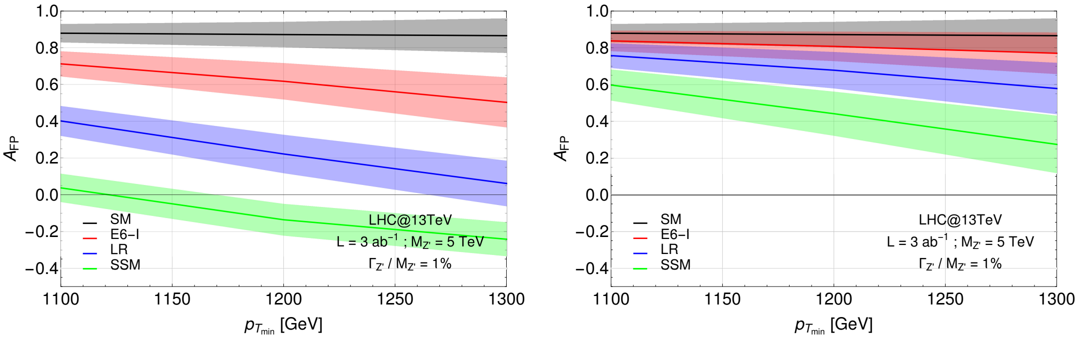

(a) (b)

FIGURE 4.13: A_{FP} central value and statistical 1σ error band as function of p_T^{min} cut for the LHC at 13 TeV and $\mathcal{L} = 3\ \text{ab}^{-1}$. The black line represents the SM while the coloured lines represent the three benchmark models. The mass of the Z' boson is fixed at 5 TeV while its width over mass ratio $\Gamma_{Z'}/M_{Z'}$ has been fixed to 1% (a) and 5% (b). The values for the FP are chosen in accordance to Tab. 4.2.

factorisation and renormalisation scales. Hence, this FP displays model-independent characteristics, as it is only sensitive to the collider energy (which is known) and the mass of the intervening Z' (which is expected to be extracted from the di-lepton invariant mass).

In fact, while the FP location is stable against variations of the Z' boson width, the A_{FP} strongly dependent upon the width. The combination of these features makes of A_{FP} a suitable observable to determine the characteristics of any Z' which may be discovered at the LHC. In addiction, the A_{FP} shows a good sensitivity to wide resonances which are generally beyond the sensitivity of the usual "bump" searches, and furthermore the its measurement can be used effectively to constrain the width parameter in the fit of a resonance peak of a Z' signal.

The effectiveness of the new variable is also expected to grow with the increase of the LHC luminosity, such that its importance will be appreciated after a few years of Run-II (i.e., after some 300 fb^{-1} of data) or else rather immediately at a future High-Luminosity LHC (HL-LHC) stage (i.e., starting from 1 ab^{-1} of data), depending on the Z' mass, width and couplings.

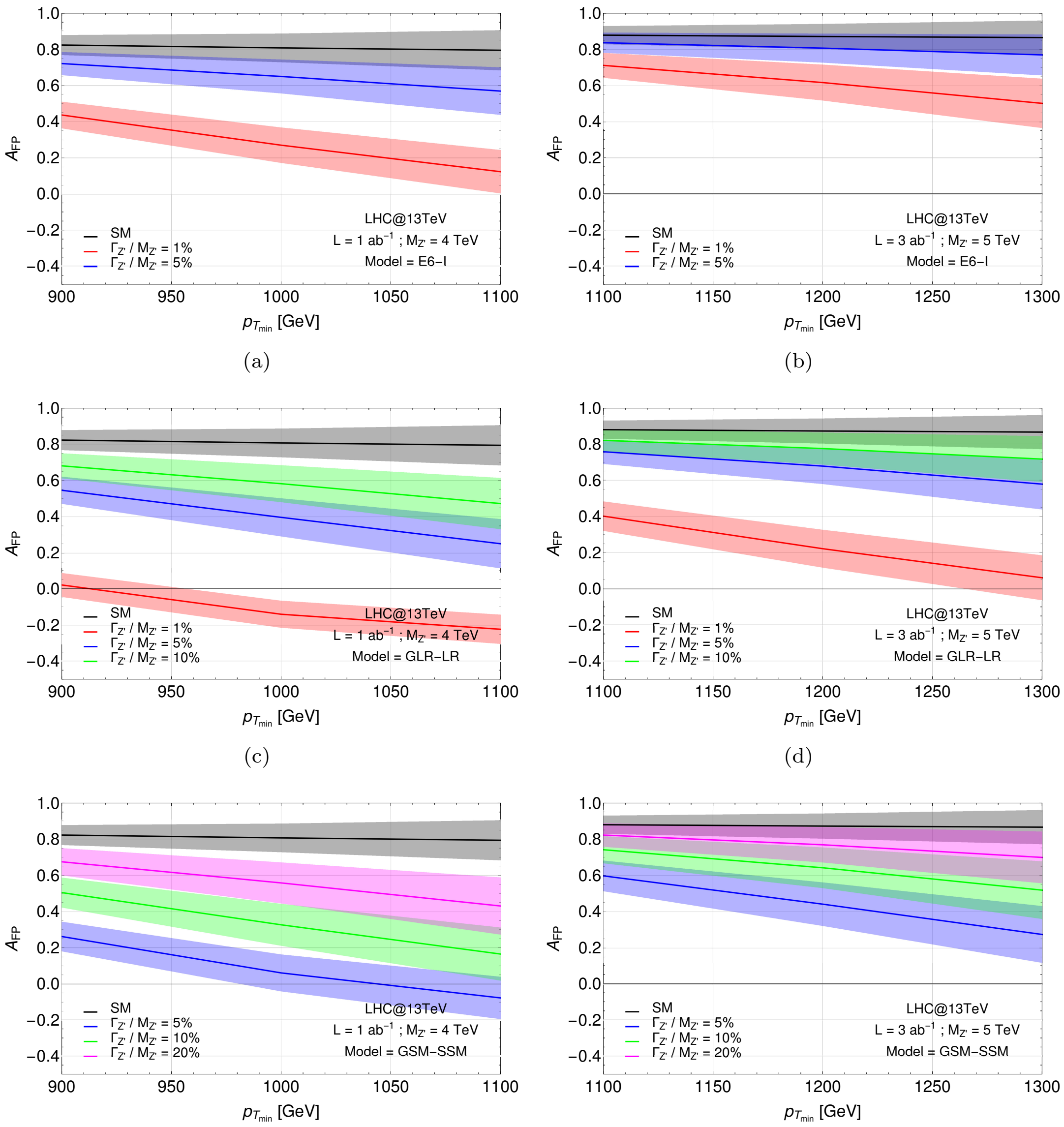

(a) (b)

(c) (d)

(e) (f)

FIGURE 4.14: $A_{\rm FP}$ central value and statistical 1σ error band as function of $p_T^{\rm min}$ cut for the LHC at 13 TeV and $\mathcal{L} = 1$ ab^{-1}. The black line represents the SM while the coloured lines represent four different widths (1%, 5%, 10% and 20%) of the Z' resonance in the E6-I (a), GLR-LR (c) and GSM-SSM (e) model with a mass of the Z' boson fixed at 4 TeV. The values for the FP are chosen in accordance to Tab. 4.1. Similarly the same exercise is repeated for the E6-I (b), GLR-LR (d) and GSM-SSM (f) model with a mass of the Z' boson fixed at 5 TeV and and $\mathcal{L} = 3$ ab^{-1}. The values for the FP are chosen in accordance to Tab. 4.2.

Chapter 5

Multiple Z'-bosons

5.1 Introduction

The experimental analyses have been designed to address the Z'-boson search in the single-resonance scenario and prescriptions to bridge the data analysis results and the theoretical interpretation within explicit Z'-boson theories. In this chapter is discussed the case of spectra with multiple Z'-bosons [2, 27]. Herein, further challenges appear as, in several well-motivated theoretical models, such Z' states can be quite close in mass and mix with each other so that different scenarios might emerge. Two such resonances may be wide and close enough in mass so as to appear as a single broad resonance in the di-lepton invariant mass spectrum. These resonances may interfere strongly with each other and/or with the SM background, thereby further blurring the usual procedures adopted in profiling a possible excess.

These features are illustrated here within two classes of popular models: the Non-Universal Extra Dimensional (NUED) scenario and the 4-Dimensional Composite Higgs Model (4DCHM). The first belongs to the multi-Z' weakly coupled class of theories while the second is an example of a strongly interacting theory. It will be shown that NUED extra gauge bosons can be searched for and theoretically interpreted using the traditional techniques currently employed by the CMS experiment. In contrast, the 4DCHM requires a modified approach for setting limits on masses and/or couplings of the extra heavy gauge bosons.

5.2 The NUED model

One of the flawed parts of the SM concerns the understanding of the gravitational interactions. Such interactions in fact destroy the renormalisability of the theory and give rise to the hierarchy problem. As these quantum gravity effects seem to imply the existence of extended objects living in more than four dimensions, a possible solution to these problems is provided by a scenario of large Extra Dimensions (EDs) and a low scale quantum gravity in the TeV region [6, 7]. Within this scenario, a natural question is how to detect the EDs. The answer can only be given for specific classes of models, as it depends on the details of the realisation of the EDs and the way known particles emerge inside them. The theoretical scenario analysed here is based on the model of Refs. [96–100], when embedded in the framework described in Refs. [6, 7]. This setup is called the NUED model. Here, all SM fermions are totally localised on the brane whereas all SM gauge bosons are fully propagating into the bulk. One of its simplified versions, called NUED(EW), predicts that only the EW SM gauge bosons are allowed to propagate in the EDs as proposed in Ref. [101]. Our study is representative of both models, the original and the simplified one.

In these two scenarios, two fundamental energy scales play a major role. The first one, $M_s = l_s^{-1}$, is related to the inner structure of the basic objects of the theory, that are assumed to be elementary strings. Their point-like behaviour is viewed as a low-energy phenomenon: above M_s the string oscillation modes get excited making their true extended nature manifest. The second important scale, R^{-1}, is associated with the existence of a higher dimensional space: above R^{-1} new dimensions open up and particles, called KK excitations, can propagate in them. The number of EDs, D, which are compactified on a D-dimensional torus, can be as large as six [6] or seven [7]. Here, the NUED model in 5 dimensions will be discussed. The particle content of this model can be described as follows. The gravitons, represented as closed strings, can propagate in the whole higher-dimensional space, $3+d_{\parallel}+d_{\perp}$. Here, $3+d_{\parallel}$ defines the longitudinal dimension of the big brane, which contains the small 3D brane where the observed SM particles live. The symbol $d_{\perp}$ indicates the EDs transverse to the big brane, which are felt only by gravity. The SM gauge bosons, represented as open strings, can propagate only on the $(3+d_{\parallel})$-brane. The SM fermions are localised on the 3D brane, which intersects the $(3+d_{\parallel})$-dimensional one. They do not propagate in EDs (neither $d_{\parallel}$ nor $d_{\perp}$), hence they do not have KK-excitations.

From this picture it is clear that in the scenario considered here $D = d_{\parallel} = 1$. Assuming periodic conditions on the wave functions along each compact direction, the states propagating in the $(4 + D)$-dimensional space are seen from the 4D point of view as a tower of states having a squared mass:

$$M_{KK}^2 \equiv M_{\bar{n}}^2 = m_0^2 + \frac{n^2}{R^2} \tag{5.1}$$

with m_0 the 4D mass and n a non-negative integer. The states with $n \neq 0$ are called KK states. Since, in the class of NUED models in 5D, KK modes exist only for the gauge bosons, while fermions have no KK states, obviously, the particle content is very different from the ordinary SM inventory. The fermionic sector remains practically unchanged, but for each gauge boson it is present a zero mode, together with a tower of complementary particles of higher mass, M_{KK}. The usual interpretation in terms of 4D particles is that the zero modes are the known SM gauge bosons, while the KK states are their heavier copies. Hence, more explicitly, in the NUED model all $SU(3)\times SU(2)\times U(1)$ SM gauge bosons propagate into the bulk 5D space and therefore have KK-excitations. In the more recent NUED(EW) construct, only the $SU(2)\times U(1)$ EW gauge bosons can propagate in the compactified ED and acquire KK excitations [101]. In both models the fermionic content is totally confined on the 3D brane. These two scenarios share most part of their features and just differ for the gluon contribution to fully hadronic or semileptonic processes at the LHC which are not addressed in this analysis. This means that the results presented here are valid in both scenarios.

Assuming that leptons and quarks are localised on the brane is quite a distinctive feature of the class of NUED models, giving rise to well defined predictions. An immediate consequence of the localisation is that fermion interactions preserve the momenta in the four-dimensional world but violate the energy-momentum conservation along the additional fifth dimension. One can thus produce single KK excitations, for example, via $f\bar{f}' \to V_{KK}^{(n)}$ where f, f' are fermions and $V_{KK}^{(n)}$ represents a massive KK excitation of W, Z, γ, g gauge bosons. Conversely, gauge boson interactions conserve the momenta along all 4+1 dimensions, making the self-interactions of the kind $VV \to V_{KK}^{(n)}$ forbidden. Owing to these interactions, KK states or their indirect effects could have been detected at LEP and/or LHC in principle. An updated review on both indirect and direct exclusion limits on KK-particles, predicted within the class of NUED models, can be found in Ref. [102]. The indirect limits come from the EWPTs at LEP, as the presence of KK excitations can in principle affect the computation of the low-energy precision observables through the (re-)definition of the Fermi constant, G_F, weak mixing angle and masses of the SM vector bosons.

The constraints on M_{KK} extracted from the EWPTs have a strong dependence on the realisation of the scalar sector in the 5D NUED model(s). There are no physical considerations dictating that the Higgs boson should be a brane field or the zero mode of a bulk field. It is very common in the literature to consider a scenario where both these options are realised, the discovered Higgs being a mixture of these. The relative

Model	$\sin\beta$	EWPT	LHC ($pp \to l^+l^-$)	LHC ($pp \to jj$)
NUED	0.45	3.8 TeV	3.8 TeV	-
NUED	1.0	5.4 TeV	3.8 TeV	-
NUED(EW)	0.45	3.8 TeV	3.8 TeV	3.25 TeV
NUED(EW)	1.0	5.4 TeV	3.8 TeV	3.25 TeV

TABLE 5.1: Summary of EWPTs and LHC (8 TeV and $\mathcal{L} = 20$ fb^{-1}) 95% CL exclusion bounds on the mass of KK excitations of SM gauge bosons within the NUED model and its simplified version NUED(EW) as described in the text.

contribution of the two fields is parametrised by $\tan\beta = \frac{<\phi_2>}{<\phi_1>}$ or, equivalently, $\sin\beta$. Here, ϕ_1 is the bulk field, so for $\sin\beta = 0$ only a bulk Higgs state exist. The important point here is that, for $\sin\beta \neq 0$, the Vacuum Expectation Value (VEV) of the brane field can cause mixing between the different modes of the gauge bosons and the weak eigenstates are no longer mass eigenstates. The ensuing diagonalisation to determine the mass eigenvalues leads to a model dependent redefinition of gauge boson masses and couplings, which receive additional corrections from the KK states due to the rotation in state space. The strength of these corrections depends on the contribution of the brane Higgs field, being proportional to powers of $\sin\beta$. These effects induce additional corrections to the EWPT observables measured at LEP. Depending on the Higgs sector realisation, the indirect limit from LEP is therefore $R^{-1} \geq 3.8$–5.4 TeV. This has left very little room for KK states discovery at the 7, 8 TeV LHC. During the past run, direct searches performed with total integrated luminosity $\mathcal{L} = 20$ fb^{-1} have been able to set exclusion bounds comparable to those coming from EWPTs. The analysed processes are the DY $Z^{(1)}_{KK}, \gamma^{(1)}_{KK}$ production in both di-lepton and di-jet channels. Tab. 5.1 summarises the present indirect and direct bounds on the mass of the KK states within the two considered frameworks. In the table, the blank entries in the first two rows indicate that the corresponding bounds have not been extracted yet. From Tab. 5.1, one can deduce that the search window in the ongoing Run-II at the upgraded LHC is $R^{-1} \geq 3.8$ TeV for NUED model(s) in 5D.

In the following subsections is considered the case of the DY channel mediated by the KK excitations of the SM neutral gauge bosons, $Z^{(n)}_{KK}$ and $\gamma^{(n)}_{KK}$, where n defines the excitation number of the resonance in the tower. For each level of the ED tower of states, the two resonances are very close in mass so their spectrum would appear degenerate in any experimental search. In order to validate the numerical procedures in view of our LHC Run-II studies, first some of the experimental limits quoted in Tab. 5.1 will be re-obtained independently. In Sect. 5.2.1, the scope of the LHC upgrade will be assessed in excluding or discovering the NUED models. In particular in this analysis FW and interference effects are taken into account, as they play a crucial role.

5.2.1 DY Process: present bounds and "bump" searches

In this section, discovery prospects and exclusion limits are derived for the LHC with the 13 TeV energy of the Run-II and for luminosity ranging from $\mathcal{L} = 30$ fb^{-1} and $\mathcal{L} = 300$ fb^{-1}. The DY process giving rise to electron and muon pairs in the final states is considered. In the ED scenario, this process can be mediated by the KK excitations of the SM neutral gauge bosons:

$$pp \to \gamma, Z, \gamma^n_{KK}, Z^n_{KK} \to l^+l^- \tag{5.2}$$

with $l = e, \mu$. As the mass bounds on the KK modes coming from the LHC Run-I are pretty high, only the first level of the ED tower of KK states has some chance to be detected (or excluded) at the ongoing LHC Run-II. For this reason this analysis is limited to the production and decay of the extra γ^1_{KK}, Z^1_{KK} from now on called simply γ_{KK}, Z_{KK}.

Before entering the details of the analysis, some preliminary exercises will be carried out in order to illustrate the phenomenology induced by the possible existence of EDs. In particular, the effects coming from FW and interference of the extra gauge bosons with the SM ones will be underlined with their consequences on the signal shape. The FW effects are what typically one expects for (rather) narrow resonances, as the width of the NUED and NUED(EW) extra gauge bosons is below $\sim 6\%$ of their mass: $\Gamma_{\gamma_{KK}}/M_{\gamma_{KK}}$ $= 4.2\%$ and $\Gamma_{Z_{KK}}/M_{Z_{KK}} = 6\%$. In contrast, in Fig. 5.1(a), is clearly visible the effect of the interference between the KK modes (first level of the ED tower) and the SM gauge bosons on the signal line-shape is quite distinctive of NUED models. The presence of a pronounced dip (a sort of inverted peak) appearing before the resonant structure around the pole mass of the new gauge bosons is indeed quite characteristic. The contributions of the different components to the total differential cross section are visible in Fig. 5.1(b). One feature of this model is here explicit: there is no individual contribution shaping the inverse peak (positioned at around 2.2 TeV for this benchmark point), rather the latter emerges as a global dynamics due to a cumulative effect driven by the various negative contributions coming from the interferences between the SM neutral bosons with their associated KK excitations. This happens because this is the case of maximal interference since the chiral couplings of the heavy excitations are the same as those of their SM counterpart, up to a rescaling factor of $\sqrt{2}$.

Despite the large interferences that could happen before the appearance of the resonant peak, whose position and magnitude strongly depend on the specific model, the extraction of mass bounds on the KK resonances can still be performed in a model independent

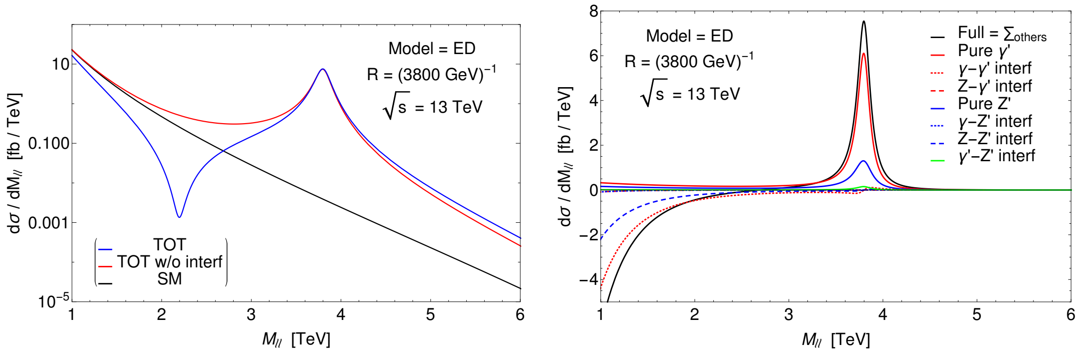

(a) (b)

FIGURE 5.1: (a) Differential cross section as a function of the di-lepton invariant mass for the NUED model with $R^{-1} = 3.8$ TeV. The blue line represents the full result while the red line does not include interference effects. (b) Same as in plot (a) for each individual contribution to the total differential cross section. The colour code is described in the legend.

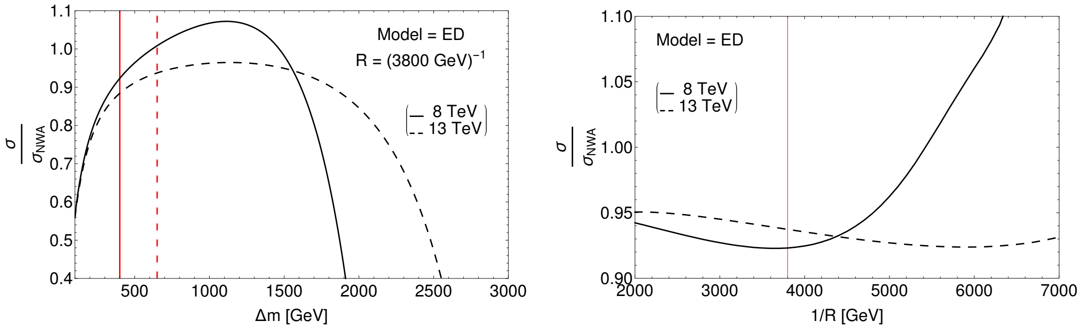

(a) (b)

FIGURE 5.2: (a) Ratio of the complete cross section over the NWA result as a function of the symmetric integration interval taken around the Z' pole mass, $|M_{ll} - M_{Z'}| \leq \Delta m$, for the NUED model with $R^{-1} = 3.8$ TeV. LHC at 8 TeV (solid line) and 14 TeV (dashed line) energies are considered. The red vertical lines represent the integration interval $|M_{ll} - M_{Z'}| \leq 5\% E_{\text{coll}}$ adopted by CMS at the 8 TeV LHC (solid) and 14 TeV LHC (dashed), when extracting the Z' mass limits within a given model by crossing the computed theoretical cross section with the 95% CL upper bound on the BSM cross section derived from the data analysis. (b) Ratio of the complete cross section integrated over the mass interval $|M_{ll} - M_{Z'}| \leq 5\% E_{\text{coll}}$ over the NWA result as a function of the inverse of the compactified extra dimension length R. The red vertical line represents the actual limit on R^{-1} according to Ref. [102].

way up to a large extent. Altogether, in fact, the model dependent FW and interference effects can be kept below $O(10\%)$ of the total cross section when integrating the di-lepton spectrum in the invariant mass interval $|M_{ll} - M_{Z'}| \leq 5\%\ E_{\text{coll}}$ around the hypothetical pole mass, $M_{Z'}$, of the two (almost) degenerate KK excitations belonging to the first level of the ED tower of states. Here, E_{coll} is the collider energy. The integration interval is the one proposed in Ref. [13] for computing the total theoretical cross section within a large class of single Z'-boson models and adopted by the CMS collaboration [11].

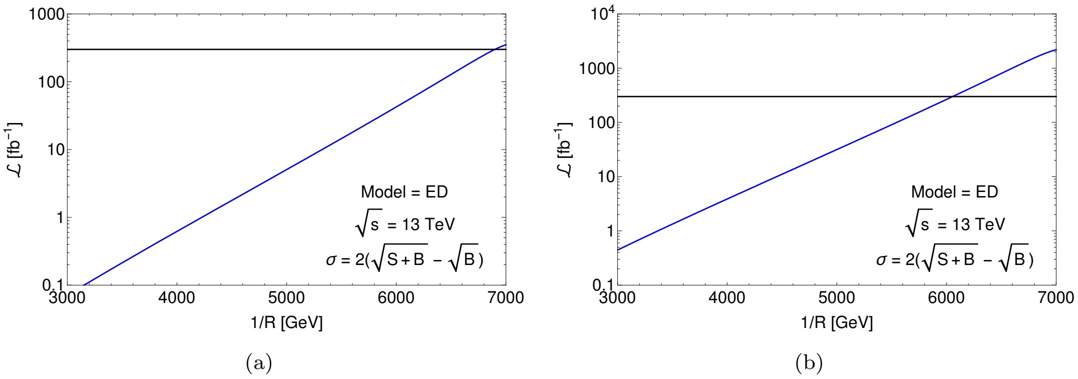

FIGURE 5.3: Required luminosity for the exclusion (plot (a) $\sigma = 2$) and discovery (plot (b) $\sigma = 5$) limits in the NUED model as a function of the inverse length of the compactified extra dimension. The horizontal lines are fixed to be $\mathcal{L} = 300$ fb^{-1}, which is the design luminosity that will be achieved at the end of Run-II. They intercepts the curve of the model giving an exclusion (discovery) limit $R^{-1} > 6.9$ (6) TeV.

It should be noted that if a sizeable interference dip appears at rather low di-lepton invariant masses, as in NUED models, it could affect the estimate of the SM background shape, a priori, and its normalization. This would suggest to modify the present selection of the mass region where the SM background is normalized to data and shift it away from the peak.

With respect to the experimental analysis for single narrow resonances described in Chapter 2, the multi-resonant NUED models behave exactly in the same way as the singly resonant E6, GLR and GSM classes. By virtue of this feature, limits on the degenerate multi-resonant KK modes can thus be extracted from the CMS data analysis of the di-lepton spectra, directly and unambiguously. To support this statement, in Fig. 5.2(a) is plotted the ratio of the full cross section over the NWA result as a function of the symmetric integration region around the pole mass of the degenerate KK excitations belonging to the first level of the ED tower of states. The vertical red line represents the di-lepton invariant mass interval proposed in Ref. [13] for computing the total theoretical cross section. This shows that, if one restricts the integration region, the difference between complete cross section and NWA result, normalized to the NWA cross section, is indeed below $O(10\%)$. The NWA cross section shown in Fig. 5.2 is the sum of the two NWA cross sections corresponding to the two KK excitations of the SM photon and Z boson. It has been checked that the latter result does not change with respect to the length scale R of the extra dimension. In Fig. 5.2(b) is plotted the deviation of the full result from the one computed under the NWA as a function of the parameter R^{-1}. Here the red vertical line represents the actual limit on R^{-1} according to Ref. [102]. Again the deviations are below $O(10\%)$ in the full range of R values which can be explored at the LHC Run-II. This is due to the fact that the interference pattern is such that the interference effects become sizeable at low invariant masses, away enough from the resonant peak. This feature is extremely model dependent. The composite Higgs models case will be presented in the next section where the position of the interference with respect to the resonant peak will be indeed completely different, motivating different approaches for the multi-Z' hunt at the LHC and leading to different conclusions.

Remaining within ED models, the prescription of [13] works perfectly. The current bounds on the mass of the KK excitation of SM photon and Z boson have been re-obtained. As previously mentioned, the most recent bound from the LHC data at 7, 8 TeV gives $R^{-1} > 3.8$ TeV [102]. This limit has been closely reproduced using the CMS setup (for details see Ref. [11]), hence validating the adopted procedure. In the calculation NNLO corrections are included and the two channels $(e^+e^-, \mu^+\mu^-)$ significance have been combined with their individual acceptances and efficiencies as quoted in [11].

Applying the same setup, the prospects of discovery and exclusion of KK excitations can be projected for the 13 TeV LHC Run-II. The results of this analysis are presented in Fig. 5.3, where the left panel (5.3(a)) shows the projected exclusion bounds and the right one (5.3(b)) the projected discovery potential as a function of the collected luminosity at the ongoing 13 TeV run of the LHC. The horizontal lines are fixed to be $\mathcal{L} = 300$ fb^{-1}, which is the design luminosity that will be achieved at the end of Run-II. In absence of any signal, one will be able to push the exclusion limit on the mass of the KK excitations of the photon and Z boson up to $R^{-1} > 6.9$ TeV. In the positive case of a signal, the sensitivity of the LHC will allow the discovery of the first EW neutral states of the ED tower up to around 6 TeV. This analysis has been performed in the traditional way valid for narrow resonances. Such an approach would not be appropriate in two cases: if the branching of the Z'-boson(s) into electron and muon pairs were not high enough to generate a cross section much bigger than the SM background and/or if the new resonance(s) were rather wide.

Assuming a new resonance has been discovered in the described bump hunt during the LHC Run-II at low luminosity, the next step would be tracking the underlying theory predicting such a particle. The next sub-section focuses on profiling the new resonance(s) during a successive LHC run at higher luminosities. In particular is considered the case where a (degenerate) peak is clearly seen at large di-lepton invariant masses in the standard bump search. Under this circumstance, the dip at low invariant masses could be used to characterise the signal in such a way to confirm EDs as the underlying BSM scenario.

5.2.2 DY Process: profiling KK modes

Here is addressed the question of how to profile the KK excitations in the case of their discovery in the standard bump search. A distinctive features of NUED models is the appearance of a sizeable dip before the resonant structure, as already pointed out in Refs. [101, 103, 104]. This characteristic is common to multi-Z'-boson models, even if the distance between dip and peak is highly model dependent, and helps disentangling them from singly resonant Z'-boson scenarios. This behaviour is quantified in Fig. 5.4 where is shown a comparison between the signal shape predicted by the NUED models and the SSM, which is used as the primary benchmark by the LHC experimental collaborations. In the multi-Z' boson case the depletion of events is much more pronounced and concentrated in a smaller region before the peak. The statistical significance of the dip is indeed much bigger in the NUED models, as shown in Figs. 5.4(b) and 5.4(d). Of course, the significance scales with the luminosity. In Fig. 5.5 is shown the integrated luminosity that is required to exclude the SM background hypothesis at 95% CL, owing to the depletion of events caused by the destructive interference between the new Z_{KK} and γ_{KK} bosons and their SM counterparts, as a function of the KK mode mass. These contours have been evaluated by integrating the differential cross section in a symmetric invariant mass window around the dip, taken between the point where the new resonance peak(s) crosses the SM background and the symmetric counterpart. For the design luminosity $\mathcal{L} = 300$ fb^{-1}, the dip could be detectable for all KK-mode masses that can be possibly discovered at the LHC Run-II thus allowing to interpret the data accordingly and pin down the existence of EDs.

Another way of profiling a resonance(s), very known in the literature, is to introduce the A_{FB}. Unfortunately in the ED case, the shape of the A_{FB} distribution as a function of the di-lepton invariant mass is in fact not statistically significant for the designed luminosities achievable at the LHC in the near future. Different types of asymmetry, measured in a different channel, could however play that role. In Ref. [105] it has been shown that, combining the charge and spin polarization asymmetries in the $t\bar{t}$ channel, it is possible to identify the presence of the two quasi-degenerate states γ_{KK} and Z_{KK} in a resonant signal at the LHC. The measurement of such asymmetries would then allow one to distinguish the quasi-degenerate double resonant spectrum, predicted by the NUED model(s), from a “standard” single Z'-boson that could present a similar signal in a bump hunt analysis.

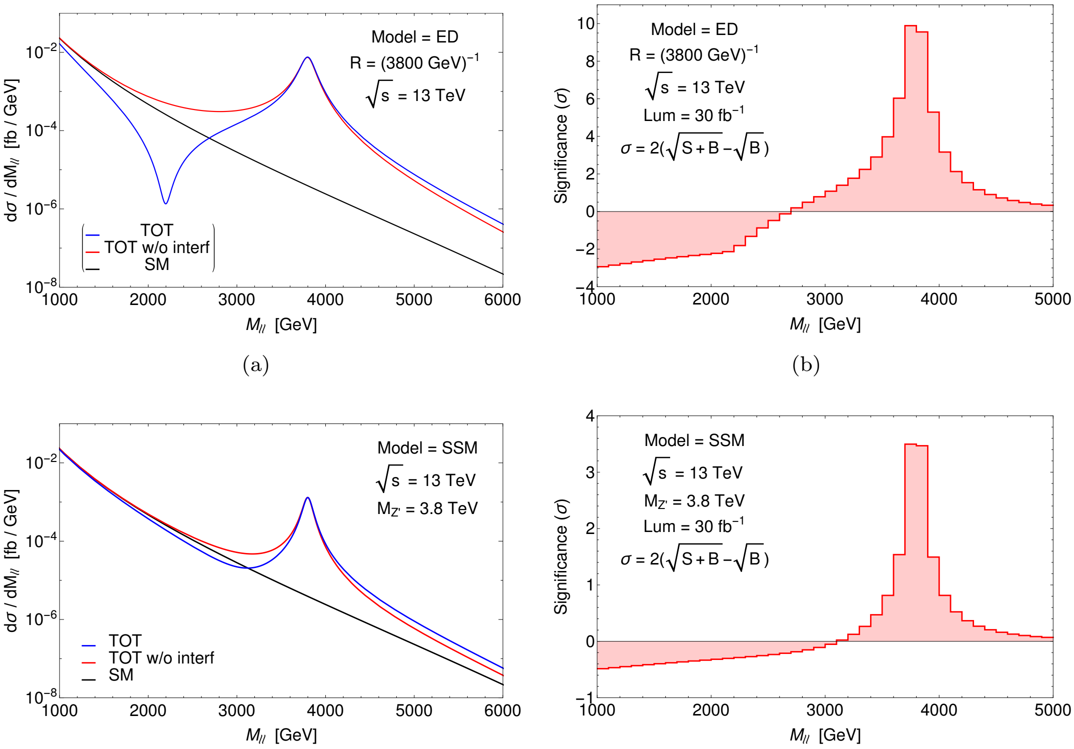

(a) (b) (c) (d)

FIGURE 5.4: (a) Signal shape within the NUED models for $R^{-1} = 3.8$ TeV and (b) its significance for an integrated luminosity $\mathcal{L} = 30$ fb^{-1}. (c) Signal shape within the SSM with $M_{Z'} = 3.8$ TeV and and (d) its significance for an integrated luminosity $\mathcal{L} = 30$ fb^{-1}.

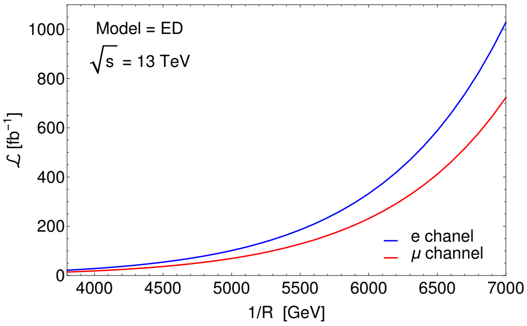

(a)

FIGURE 5.5: Required luminosity for excluding the background hypothesis at 95% CL owing to the depletion of events caused by new physics. The blue (red) line represents the di-electron (di-muon) final state for which the corresponding experimental acceptance and efficiency have been implemented.

5.3 The CHM scenario

One way to alleviate the hierarchy problem present in the SM, which manifests itself through the appearance of quadratically divergent radiative corrections to the Higgs mass, therefore implying a huge degree of fine tuning if the SM is extrapolated up to the Planck scale, is to protect the mass of the scalar with a symmetry. This is in fact the same mechanism through which in the SM the fermion and gauge boson masses are shielded from these virtual corrections, that is, by means of a chiral and gauge symmetry, respectively, while the scalar mass is left unprotected. Supersymmetry (SUSY) is the most common manifestation of this paradigm. The boson-fermion symmetry present in the theory guarantees the stability of the Higgs mass via cancellations between the top and the stop loop contributions to the two point function of the Higgs (pole) mass. However, this is not the only solution. An alternative proposal is to assume that the Higgs boson is a composite state, arising from some unspecified strong dynamics at a scale higher than the EW one. In order to realise the Higgs boson as a spinless light state (that is, lighter than other resonances that might be present in the strong sector), it can be postulated to be a Nambu-Goldstone Boson (NGB) arising from the spontaneous breaking of a global symmetry in the strong sector. The NGB will eventually acquire a (small) mass through an explicit, but weak, breaking of the global symmetry, becoming a Pseudo-NGB (PNGB). This automatically solves the hierarchy problem since all the radiative corrections affecting the Higgs mass will be saturated at the composite scale, that is, its mass will not be sensitive to virtual effects above it, and also it agrees with the historical pattern that has so far seen all the (pseudo)scalar particles known in Nature to be composite states. This idea goes back to the '80s [8] and strongly resembles the dynamics with which it is possible to explain the lightness of the pions with respect to other mesons like the ρ's, that is, by postulating the former to be a PNGB of the spontaneous breaking of the QCD chiral symmetry.

One of the most economical breaking patterns that can be imagined is the one that develops just four PNGBs, that is, the minimum number to be identified with the SM Higgs doublet. Together with the requirement of a custodial symmetry to protect the EW ρ parameter from large deviations, this automatically leads to the choice of $SO(5)/SO(4)$ as the most simple realisation of the PNGB paradigm. This coset choice was introduced and discussed in [9]. Beside a theoretical appeal, the importance of such a theory is that it is testable at the LHC. If the hierarchy problem is in fact solved by a new strong dynamics, this will manifest itself also through new resonances that should be, for a reason of fine tuning, around the TeV scale. This is in fact the case for the copies of the SM quarks (especially of the top quark, given the dominant role it plays in the virtual corrections to the Higgs mass), that are called *top partners*, which are expected to be at an energy scale which is actually presently being tested at the LHC. In general, also copies of the SM gauge bosons might be present, although at a mass higher that the spin 1/2 states, due to their contribution to the EW oblique observables, which push these states to a somewhat higher, nevertheless accessible, mass scale.

Despite the assumptions made in the experimental searches, that usually allow for the presence of just one extra particle in order to derive limits which are as model-independent as possible, it is important to stress that in realistic CHM realisations these states are present with a higher multiplicity and this is valid both for spin 1/2 and for spin 1 resonances. This feature might cause model-dependent behaviour from the pure sum of the various signal contributions, up to more involved interference effects between these states and the SM, or between themselves. In order to quantify these effects a specific composite Higgs realisation is chosen. This section focuses on the so called 4DCHM proposed in [10]. The 4DCHM can be described as two non-linear σ-models, one for the $SO(5)/SO(4)$ breaking pattern while the other for the $SO(5)_L \otimes SO(5)_R/SO(5)_{L+R}$ one. This construction develops 10+4 NGBs, 10 of which will be absorbed adding a complete $SO(5)$ multiplet of resonances living in the $Adj[SO(5)]$, giving therefore rise to 10 massive degrees of freedom, identified with 4 neutral and 6 charged (conjugated) spin 1 physical states. The remaining 4 play the role of the Higgs fields.

Let us briefly describe the characteristics of the 4 neutral spin-1 states, which are the subject of this section [1]. The group $SO(4)$ is isomorphic to $SU(2)_L \otimes SU(2)_R$ and two resonances do correspond to the neutral component of the (**3,1**) and (**1,3**) triplets, degenerate in mass before the explicit breaking of the $SO(4)$ global symmetry. The other two neutral resonances arise from the neutral component of the $SO(5)/SO(4)$ coset, with a mass $\sqrt{2}$ times higher than the ones just described. However, just one of these states will couple to the light fermions, reducing therefore the number of resonances playing a role in this analysis to 3. For a complete description of the models see Ref. [10] (see also [93] for additional Z' studies in DY channels). Neglecting the $SO(4)$ explicit breaking, the masses of the $SO(4)$ and $SO(5)/SO(4)$ resonances are given by fg_ρ and $\sqrt{2}fg_\rho$, respectively, where f is the (compositeness) scale of the spontaneous strong symmetry breaking and g_ρ the gauge coupling of the extra $SO(5)$ group. The explicit breaking of the $SO(4)$ symmetry will occur by introducing the SM $SU(2)_L \otimes U(1)_Y$ interactions, with coupling strength g_0 and g_{0Y}, respectively. This will cause a linear mixing between the SM W^3_L, Y and the neutral component of the (**3,1**) and (**1,3**) triplet of $SU(2)_L \otimes SU(2)_R$, generating therefore a positive shift of the masses of these extra states. The mixing angles between the SM and extra states will be approximately $\theta \sim g_0/g_\rho$ and $\psi \sim g_{0Y}/g_\rho$. This will make these two states to acquire a mass $fg_\rho/\cos\theta$ and $fg_\rho/\cos\psi$, while further corrections of the order of $\xi = v^2/f^2$ will appear after EWSB, being v the SM Higgs

---

[1] Actually, in order to guarantee a correct hypercharge assignment to the SM fermions, an extra $U(1)_X$ group needs to be added, bringing to 5 the number of neutral resonances. Under the assumption of equal couplings for the $SO(5)$ and $U(1)_X$ groups (adopted in [93] as a specific parameter choice of the model described in [10]), two of the mass eigenstates can be redefined to be the ones aligned with the hypercharge direction, $T^Y = T^{3R} + T^X$, and the orthogonal combination respectively. Under this assumption, the latter will not couple to the constituents of the proton and it will be neglected throughout this analysis (this happens in the minimal realisation where just the third generation of fermions mixes with the extended sector).

VEV. These EWSB effects will be the only source of corrections to the mass of the coset resonances, which will retain therefore a mass of $\sqrt{2}fg_\rho$, modulo corrections of order ξ. The squared masses of the interested gauge bosons at $\mathcal{O}(\xi)$ are given by [93]:

$$\begin{aligned}
M^2_{Z'_2} &\simeq \frac{m^2_\rho}{c^2_\psi}(1-\frac{s^2_\psi c^4_\psi}{4c_{2\psi}}\xi),\\
M^2_{Z'_3} &\simeq \frac{m^2_\rho}{c^2_\theta}(1-\frac{s^2_\theta c^4_\theta}{4c_{2\theta}}\xi),\\
M^2_{Z'_5} &\simeq 2m^2_\rho\left[1+\frac{1}{16}(\frac{1}{c_{2\theta}}+\frac{1}{2c_{2\psi}})\xi\right],
\end{aligned} \tag{5.3}$$

with $\tan\theta = g_0/g_\rho$ and $\tan\psi = \sqrt{2}g_{0Y}/g_\rho$ (The numbering is due to the fact that $Z'_{1,4}$ are the states which are inert for the purpose of this work). With similar considerations it is possible to derive the couplings of these resonances to the light quarks and leptons. These expressions, derived at $\mathcal{O}(\xi)$, are available in Appendix B. Note, however, that in all the following results both the masses and relevant couplings have been derived in a numerical way, without relying on any expansion approximation.

Beside masses and couplings to SM fermions, of great relevance for this analysis are the widths of the extra gauge boson resonances. They can easily vary from a few percent of the masses of the Z's up to values comparable with the masses themselves. Recall in fact that, generally in CHMs, extra fermions (*top partners*) are present. They are coupled to the extra vector bosons, with a coupling strength $\propto g_\rho$, where the proportionality factor will be given by a combination of mixing angles, which will rotate the gauge states into the physical ones. It is therefore easy to understand that, if the new gauge bosons can decay into a pair of heavy fermions, the partial width in these final states can indeed be larger than the one into SM fermions, since $g_0, g_{0Y} \ll g_\rho$. This has been studied in, *e.g.*, [93], where it is shown that the width of the extra resonances can be considered as a free parameter, depending essentially only on the mass scale of the top partners.

In order to present our results for this multi Z' model, it is necessary to assess what are the current constraints on the mass spectrum of the 4DCHM arising from LEP, SLC, Tevatron and LHC data. As it is well known, extra gauge bosons give a positive contribution to the Peskin-Takeuchi S parameter, which will set a limit on the masses of these extra states and hence on the compositeness scale f. Following the guidance of [106] the choice of $f > 750$ GeV and $m_{Z'} > 2$ TeV would prevent large corrections to the S parameter. Corrections to the T parameter are slightly more involved, since they strongly depend on the extra fermionic content of the model but it can be estimated that a value of the *top partners* masses bigger than 800 GeV can be a choice compatible with the EWPTs. The ~ 2 TeV bound on the Z's mass is somewhat comparable with the one that can be obtained recasting LHC searches for narrow high mass di-lepton and WZ resonances. These searches set in fact a limit for a Z' with SM couplings to the light quarks and leptons around 2.5 TeV [107, 108]. After rescaling the signal rates, taking into account different couplings and Branching Rations (BRs) to the di-lepton final states, as well as summing over the possible contributions of the $Z'_{2,3,5}$, these searches set a mass limit of ~ 2 TeV for the masses of the (quasi) degenerate narrow $Z'_{2,3}$ (the bound weakens for large width resonances, see later). This the value that will be considered as a limit on the Z' masses.

Direct searches for extra quarks are also relevant in constraining the 4DCHM parameter space. For example, the CMS limits on pair produced *top partners*, decaying into third generation quarks plus a SM boson, varies from 800 GeV [109] in the case of an exotic fermion with electric charge 5/3 to 782 GeV [110] and 785 GeV [111] in the case of extra fermions with the top and bottom quark electric charge, respectively [2] [3]. While, in principle, different extra fermions can feed the same final states giving rise to higher exclusion bounds, as lower limits on their masses, the limits just mentioned will be adopted. This is motivated by the fact that, for a Z' with a mass larger than 2 TeV, it is enough to have a *top partner* not lighter than 1 TeV in order to have the aforementioned effects of the extra fermions onto the Z's widths. For this reason, in presenting the following results, beside fixing the Z' masses above the 2 TeV value, the Γ/M ratio of each state will be arbitrarily taken.

5.3.1 The 4DCHM phenomenology

The phenomenology of the 4DCHM in the DY channel at the LHC is presented in this subsection. This channel could contain, a priori, the production and decay of all five extra heavy vector bosons predicted by the 4DCHM. However, the lightest BSM neutral resonance, Z'_1, is inert and the Z'_4 is not coupled to first and second generation fermions. In the following therefore these extra states will be neglected and the focus will be on the three remaining ones: Z'_2, Z'_3 and Z'_5. The mediators of the leptonic DY channel, which give rise to di-eletron and di-muon final states, are depicted as follows:

$$pp \to \gamma, Z, Z'_2, Z'_3, Z'_5 \to l^+l^- \tag{5.4}$$

---

[2] Note that in the latter two cases the extra quarks can decay either via charged or neutral currents. The reported bounds are the most stringent ones considering all possible BR combinations.

[3] While this work was in its completion phase, CMS released new limits on the mass of the 5/3 charged quark obtained with early 13 TeV data. These limits, depending on the chiral structure of the *top partner*, span from 940 to 960 GeV [112]

Benchmark	f [GeV]	g_ρ	M_{Z_2} [GeV]	M_{Z_3} [GeV]	M_{Z_5} [GeV]
F	1200	1.75	2192	2258	2972
G	2900	1.00	3356	3806	4107
H	700	3.00	2129	2148	2971

TABLE 5.2: 4DCHM parameter space points associated to the benchmarks F, G and H mentioned in the text.

with $l = e, \mu$. For the experimental setup, will be taken as a reference the last analysis of di-lepton spectra performed by the CMS collaboration in its search for exotic signatures given in Ref. [11]. The values of the acceptance-times-efficiency factor for electrons and muons are based on that publication. In order to illustrate the phenomenology of the 4DCHM, the three benchmark points shown in Tab. 5.2 are selected.

To begin with, note that the lightest relevant vector boson, Z'_2, is less coupled to all the fermions than the Z'_3 (see [93] for the analytical expressions of the relevant couplings). Moreover, the heaviest resonance Z'_5 is both too heavy and weakly coupled to the proton constituents to be produced at a significant rate. For these reasons, to a first approximation, one can consider a scenario where just one extra heavy Z' is produced, that is, the Z'_3. This framework could not be fully representative of a general CHM as it is missing the possible multi-resonant structure of such theories with the corresponding interference effects. Nonetheless, it is adopted in the literature (see for instance Ref. [113]) as a first stage towards the complete picture. The framework where only the Z'_3 might be observed at the LHC is a part of the parameter space which already contains some notable features of CHMs. In the next sub-section, this reductive but already explicative scenario will be studied.

5.3.1.1 4DCHM: the singly resonant Z'_3 reduction and the NWA

In this sub-section a simplified version of the 4DCHM is considered, where only one extra gauge boson can be detected at the LHC. Taking the Z'_3 boson as the new heavy spin-1 resonance is the most natural choice for this setup, as previously explained, and exploiting its features represents a useful term of comparison with the literature (see Ref. [113–115]) and a valid warming up in view of the study of the full picture. First of all is important to check if in this singly resonant framework the commonly used NWA could be a viable method for computing the theoretical cross section. The benchmark F of Tab. 5.2 will be considered here (which is essentially the (f) point corresponding to Fig. 12 of Ref. [93]: see Tabs. 19 and 22 therein for its features). The ratio $x = \Gamma_{Z'_3}/M_{Z'_3}$ is now fixed to be 5%. This quantity is a free parameter in this model. It can range from

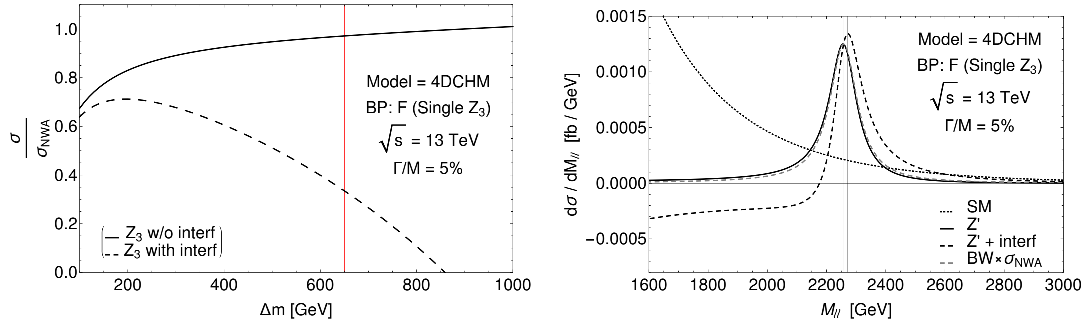

(a) (b)

FIGURE 5.6: 4DCHM benchmark F of Tab. 5.2 considering only the Z_3' boson as active with $M_{Z_3'} = 2258$ GeV and $\Gamma_{Z_3'}/M_{Z_3'} = 5\%$. (a) Differential cross section integrated in a di-lepton invariant mass window Δm around the Z_3' pole mass and normalized to the result computed in NWA. The solid line represents the ratio between the signal cross section, computed by taking into account only FW effects, and its NWA. The dashed line displays the ratio between the signal cross section, computed by accounting for both FW and interference effects, and its NWA. The vertical red line flags up the optimal mass interval which keeps the interference and FW effects below $O(10\%)$ in the case of narrow single-Z' models belonging to the E6, GLR and GSM classes of models [13]. (b) Differential cross section in the di-lepton invariant mass M_{ll}. The solid line represents the signal in FWA. The dashed line is the complete signal, including both FW and interference effects. The grey dashed line shows the BW line shape normalized to the total cross section in NWA. The dotted line is the SM background. The two vertical dashed lines represent the position of the maximum in the first two cases.

very low values ($x \simeq 1\%$) to much higher values ($x \simeq 20\%$) depending on the opening of some decay channels for the Z_3' boson, such as a decay into new heavy fermions.

First consider the effects of the variation of the di-lepton invariant mass window around the Z_3' pole mass, $|M_{ll} - M_{Z_3'}| \leq \Delta m$, and compare three quantities: the complete cross section, the cross section without the interference term between the new Z_3' boson and the SM Z and γ and the pure Z_3' signal computed in NWA.

As shown in Fig. 5.6(a), integrating the differential cross section over a di-lepton invariant mass region equivalent to three widths ($\Delta m \simeq 340$ GeV) would be enough to reproduce the NWA in absence of interference effects (solid line). These latter terms completely change this picture. The dashed line shows that in presence of interference one can never reproduce the NWA result within a few percent accuracy. The minimum difference between the complete result and the NWA is around 30% in this representative case and happens for a rather narrow integration window, i.e., $|M_{ll} - M_{Z_3'}| \leq 200$ GeV. Unfortunately, not even the more sophisticated approach of Ref. [13], indeed designed for narrow single-Z' models and working rather well for the multi-resonant NUED model(s) (see Sec. 5.2.1), seems to be applicable in the present context. As exemplified by the red vertical line, the difference here between the NWA and the full result is of $\mathcal{O}(70\%)$.

The wider the integration window, the bigger the discrepancy. This means that the interference contribution is overall destructive when one computes the total cross section. This feature is displayed in Fig. 5.6(b) where is shown the di-lepton invariant mass distribution with and without interference. The purpose of this plot is to illustrate the change in the shape of the signal that one obtains when considering the contribution of the Z'_3 alone (with its finite width) and when adding the interference with the SM background. The latter produces a typically negative(positive) correction below(above) the Z'_3 pole. Also notice the ≈ 15 GeV shift of the maximum between the two curves. The main message here is that the interference *eats* part of the "bump" at lower masses and shifts the maximum of the curve to higher values of the di-lepton spectrum. The resonant structure is thus no longer symmetric but has a sharp edge on the left-hand side of the peak. No matter what the selected mass window around the pole mass is, the signal depletion will persists and the complete result will never match the NWA.

In conclusion, the crude NWA is not the correct mathematical tool to be used within the 4DCHM. This has two immediate consequences. First of all, the theoretical cross section for the signal cannot be computed in NWA when crossing it with the 95% CL upper bound on the BSM cross section derived by the experimental collaborations in order to extract bounds on the mass and/or couplings of the extra heavy gauge bosons. If doing so, the mass limits would be in fact overestimated. For this particular case, already a theoretical error of +30% on the cross section evaluated via NWA would imply a positive shift in the Z'_3 mass bound of around 160 GeV. If one adopted the mass interval $|M_{ll} - M_{Z'_3}| \leq 5\% E_{\rm coll}$, presently used by the CMS collaboration when interpreting the results of the data analysis within narrow single Z'-boson models (see red line in Fig. 5.6(a)), the shift would increase to 450 GeV. Hence, some caution shall be used against simplistic approaches exploiting the NWA, thereby implicitly assuming that FW and interference effects are negligible. These are indeed not appropriate for CHMs in general. Neither the cross section nor the peak position coincide in the two cases. Consequently, neither the exclusion limit nor the discovery estimate in mass would be accurate.

The additional consequence of the non-applicability of the NWA is that the signal shape assumed by the CMS experimental collaboration, that is a BW convoluted with a Gaussian resolution function, is not always appropriate for this model. The interference indeed may distort this symmetrical function around the hypothetical Z'-boson pole mass. This effect might have consequences in the shape analysis of the di-lepton invariant mass spectrum which is performed via the likelihood approach as already mentioned in Sect. 5.2.1. For Z'-boson that are not very narrow, characterized for example by a ratio $\Gamma_{Z'_3}/M_{Z'_3} = 5\%$ as in Fig. 5.6(b), the line-shape distortion of the signal would be observable if the invariant mass resolution in the di-electron channel is smaller/comparable to that. In this circumstance, such an alteration of the signal compared to the BW hypothesis would affect the limit setting procedure, in presence of data points.

Aiming to be as general as possible, in the following sections the full (differential) cross section is evaluated including both FW and interference when discussing the 4DCHM phenomenology. As a final remark, is important to point out that the single Z' boson reduction of CHMs can be partial, as it is for the 4DCHM. Being applicable only to restricted regions of the parameter space, it cannot be representative of the full dynamics of a CHM. In the next sub-section, the complete version of the 4DCHM which gives rise to a multi-resonant peaking structure is analysed.

5.3.1.2 Multi-Z' 4DCHM: direct limits

In this subsection is analysed the complete 4DCHM and the impact of its multi-resonant structure for Z' searches at the LHC is addressed. First consider the direct limits on mass and couplings of the new $Z'_{2,3}$ bosons at the past LHC Run-I with 7, 8 TeV energy and integrated luminosity $\mathcal{L} = 20$ fb^{-1}. In a CHM with low mass spectra, like the 4DCHM considered here, the FW and interference effects discussed in the previous section are potentially even more complicated, owing to the presence of multi-resonant spin-1 states. In this section, the complete 4DCHM is considered here where both the Z'_2 and Z'_3 bosons are produced in DY. The third active resonance, Z'_5, is much heavier and thus difficult to produce, ultimately giving a very negligible contribution to the di-lepton invariant mass spectrum which can be explored at the LHC Run-II. For these reasons and ease of computation, the Z'_5 resonance will be neglected.

The inclusion of the Z'_2 boson does not alter the conclusions drawn for the simplified singly-resonant scenario, not qualitatively at least, only quantitatively. In Fig. 5.7(a) is plotted the di-lepton invariant mass spectrum as predicted in the complete double-resonant $Z'_{2,3}$ 4DCHM. The main feature of the complete 4DCHM spectrum is the amplification of the dip before the resonant peak(s), with respect to what has been found in the singly-resonant reduction. Incidentally, one may notice that none of the individual terms representing the interference between the various gauge bosons (SM and beyond) is responsible for the full effect. They all contribute equally and this feature is general to the 4DCHM parameter space. As previously stated, the negative contributions before the resonant peak(s) coming from interference spoil again the result in NWA (or in the FW approach, for that matter). This can be seen in Fig. 5.7(b) where the previous exercise is repeated plotting the ratio between the full signal cross section and its NWA

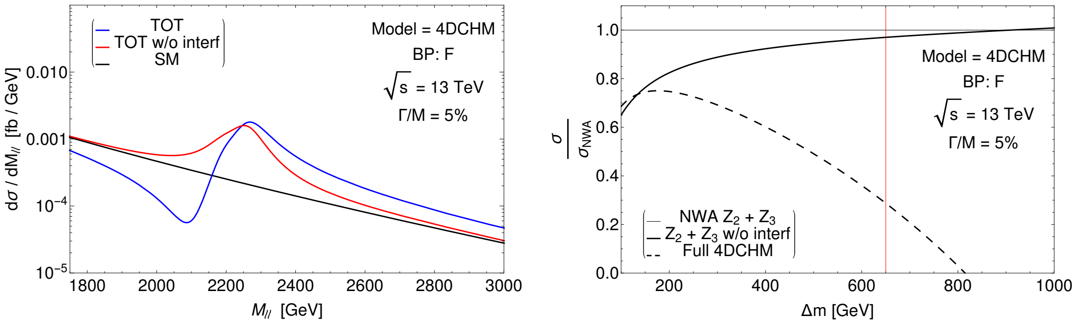

(a) (b)

FIGURE 5.7: (a) Differential cross section in the di-lepton invariant mass for the benchmark point F in Tab. 5.2 within the complete 4DCHM i.e. double-resonant $Z'_{2,3}$ scenario. (b) Ratio of the full signal cross section for the $Z'_{2,3}$ bosons corresponding to benchmark F within the complete 4DCHM scenario (dashed line) and the two resonances FWA (solid line) over the NWA result as a function of the symmetric integration interval around the peak. The vertical red line represents the CMS adopted optimal cut which keeps the interference and FW effects below 10% in the case of narrow single Z' models [13].

as a function of the integration interval, Δm, around the Z' pole mass. In the double-resonant case the NWA is defined as the sum of the two individual NWAs for the two $Z'_{2,3}$ bosons. Again there are appreciable differences between full and NWA cross sections, which are comparable to or larger than those appearing in the single-resonant Z'_3 scenario. Hence, the conclusions are same as before. One should avoid using the NWA within the 4DCHM (and similar CHMs) when computing the theoretical cross section to derive limits on the mass of the new gauge bosons. The FWA could be used pretty safely, but only for very narrow Z'-bosons. These two approximations would however be not applicable in the analysis of the signal shape for profiling the new resonances in case of discovery. In the following will be performed a complete calculation of (differential) cross sections.

Before illustrating the type of signatures that could appear at the LHC Run-II, the direct bounds on the 4DCHM parameter space coming from the data analysis performed at the past LHC Run-I with 7, 8 TeV energy and $\mathcal{L} = 20$ fb^{-1} are to be extracted. Applying the acceptance-times-efficiency factor for electrons and muons as defined in the last CMS analysis of di-lepton final states [11], the theoretical cross section is computed by integrating over the invariant mass region whose extremes are the crossing point between signal and SM background on the left and three natural widths beyond the heavier resonance on the right. Also a mass scale dependent NNLO QCD correction is included. This prescription maximises the signal and is consistent with the experimental analyses, as previously discussed. Using Poisson statistics, the statistical significance of the 4DCHM signal can be computed and constrains on the parameter space can be derived specified by the plane (g_ρ, f) where g_ρ is the gauge coupling of the $SO(5)$ group

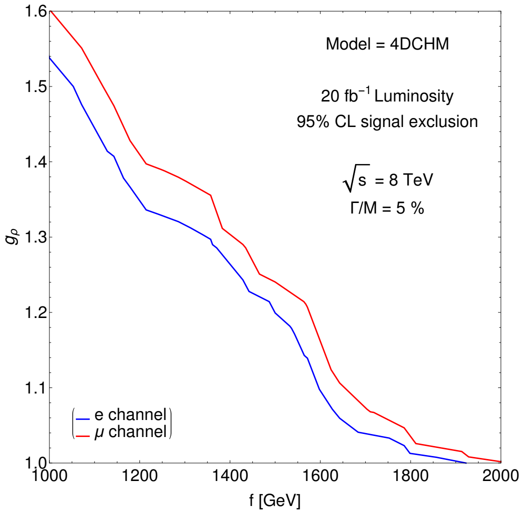

(a)

FIGURE 5.8: 95% CL contour plot in the 4DCHM parameter space generated for the past LHC Run-I with 8 TeV energy and luminosity $\mathcal{L} = 20$ fb^{-1}. The region above the solid lines is excluded by the di-electron channel (blue line) and the di-muon channel (red line). NNLO QCD corrections and the appropriate acceptance-times-efficiency factor are included.

and f is the scale of the spontaneous strong symmetry breaking. Their relation to the $Z'_{2,3}$-boson masses is given in Eq. 5.3. The results are summarized in Fig. 5.8 where the blue(red) curve refers to the electron(muon) channel (muons have a worse mass resolution than electrons.) While the di-electron invariant mass resolution is $R_e \simeq 1.2\%$, rather constant over the entire mass spectrum, for muons the resolution depends sizeably on the mass scale and reaches the value $R_\mu \simeq 9\%$ for a di-muon invariant mass of the order of 3 TeV. This feature is however compensated by a better acceptance-times-efficiency factor with respect to electrons. The global result favours the muon channel which can then set the strongest limits, as shown in Fig. 5.8.

In the next section, the better mass resolution favours the electron channel in profiling the new resonances. The two channels are thus highly complementary within the 4DCHM.

There is an important issue which concerns the future search for spin-1 resonances at the ongoing LHC Run-II. A key point to note is that the limits in Fig. 5.8 have been computed in-house, taking as external input only the CMS acceptance-times-efficiency factor for electrons and muons as a function of the di-lepton invariant mass scale. This is because the limit setting procedure implemented by the experimental collaborations does not provide at the moment a multi-resonant signal hypothesis. Oppositely to what happens within the NUED models, where the first level KK-states of the extra dimensional tower are (almost) degenerate so that the multi-resonant structure collapses into a single "bump" standing far away from the dip induced by interference effects thus allowing a direct comparison with the experimental limits on the BSM cross section, within the 4DCHM one cannot extract mass/coupling bounds from present direct searches. The spectrum is in fact not degenerate, in general, and the peaking/dip structure can be quite compressed. In the next subsection this will be discussed in more details, while projecting discovery and exclusion potential at the LHC Run-II. For now the direct limits shown in Fig. 5.8 will be assumed. In the allowed region of the parameter space, the three benchmark points listed in Tab. 5.2 are selected in order to illustrate the type of signatures one could expect at the ongoing LHC Run-II.

5.3.1.3 Multi-Z' 4DCHM: signal shapes at the LHC RunII

In this section is illustrated the 4DCHM multi-Z' boson phenomenology at the ongoing LHC Run-II with 13 TeV. In order to analyse the double resonant production of the new $Z'_{2,3}$ bosons, a key variable is the distance between the two resonances. Consider first the benchmark point H of Tab. 5.2, representing the situation in which the two resonances are (almost) degenerate, quite like in the NUED models. Fig. 5.9(a) displays the corresponding di-lepton invariant mass spectrum for the ratio $\Gamma_{Z'_{2,3}}/M_{Z'_{2,3}} = 1\%$. Here, the two Z's are separated by a distance $d \simeq 0.4\% M_{Z'_{2,3}}$ and, clearly, it is not possible to disentangle the two peaks in the differential cross section, even if quite narrow, because the difference between the two resonant masses is much smaller than the natural width. Furthermore, also the separation between the dip and the two degenerate peaks is of the same order. The peaking structure of the di-lepton invariant mass spectrum can be therefore quite compressed. This is a distinctive feature of the 4DCHM as compared to the multi-resonant NUED model where the dip is far apart. This characteristics poses an even greater challenge insofar that the di-lepton mass resolution which intervenes in sampling the mass spectrum may actually also include the negative dip, thereby blurring what sensible assumptions should be made in order to carry out an adequate statistical analysis. Even an integration around what would appear as a single peak might indeed paradoxically not produce any difference with respect to the SM background expectation, if accidentally one comes to capture also the dip, owing to experimental limitations in the mass resolution of the di-lepton pairs. The resonance(s) will then appear totally invisible. (Obviously, this peculiar behaviour is not contemplated at all in the NWA and FWA prescription.)

The quasi-natural degeneracy of the two Z' bosons, discussed above, happens in a part of the parameter space characterised by large values of g_ρ and small values of f (top of Fig. 5.8). However, owing to the Gaussian smearing, also configurations in which the two resonances are separated by a distance bigger than the natural width but comparable to

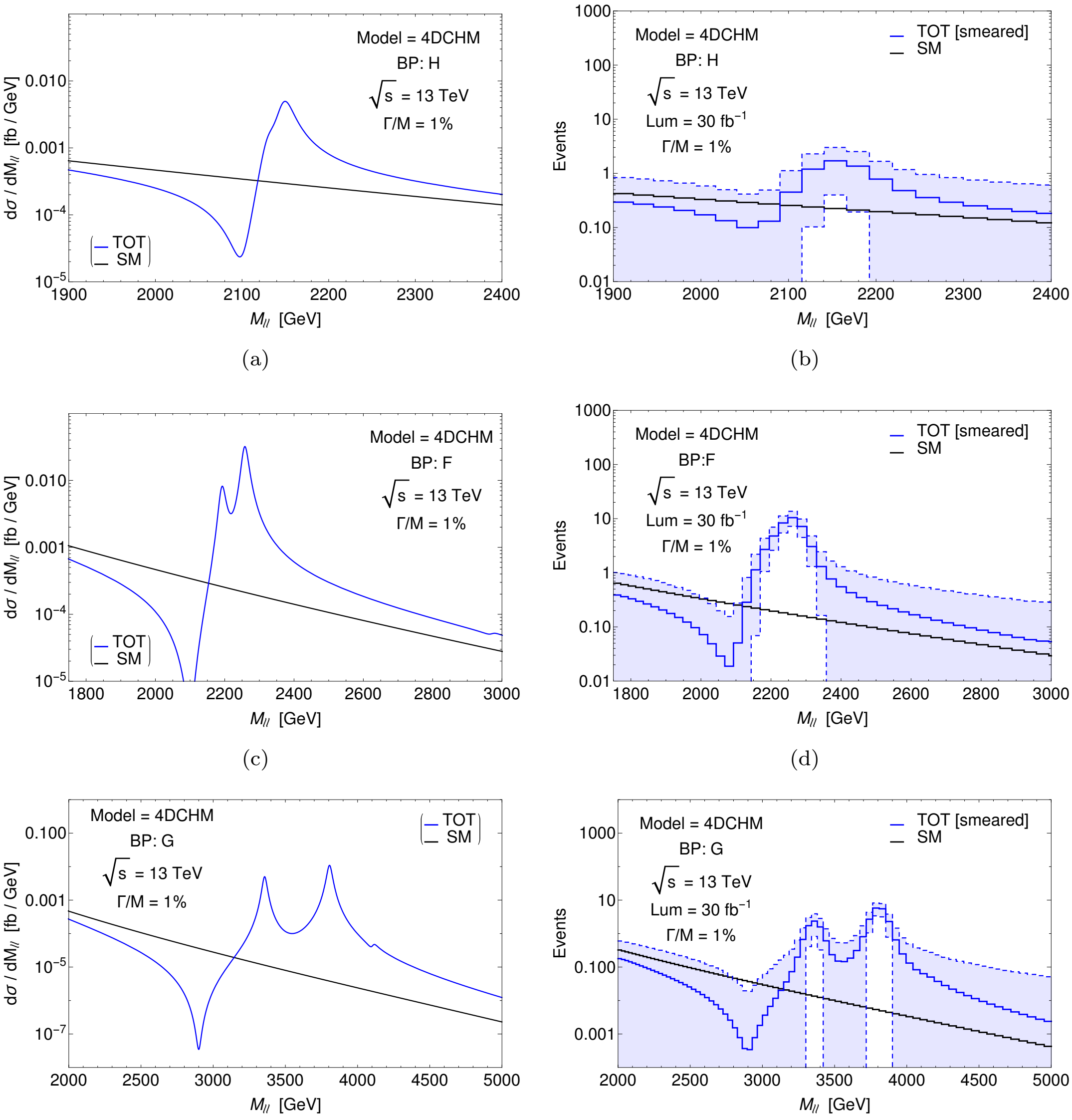

(a) (b) (c) (d) (e) (f)

FIGURE 5.9: (a) Differential cross section in the di-lepton invariant mass for the H benchmark point in Tab. 5.2 at the 13 TeV LHC Run-II. (b) The same distribution after the smearing due to the finite detector resolution. The width of the Gaussian is fixed at $w = 25$ GeV. The statistical error included in the blue error bands is evaluated for an integrated luminosity $\mathcal{L} = 30$ fb^{-1}. (c) same as (a) for benchmark F. (d) same as (b) for benchmark F with $w = 26$ GeV. (e) same as (a) for benchmark G. (b) same as (b) for benchmark G with $w = 38$ GeV.

the di-lepton mass resolution can actually appear as a single "bump". This is actually the most common scenario one can find in the 4DCHM. To illustrate this effect, it is instructive to re-create here a more realistic setup. To render the merging or otherwise of the two nearby Z'_2 and Z'_3 peaks quantitatively manifest, the finite resolution of the detector is here modelled by convolving the signal with a Gaussian distribution chosen to reproduce the experimental environment. The width of the Gaussian shape thus has been fixed according to the CMS detector resolution for electron pairs, which is roughly

1.2% of the di-electron invariant mass and is almost constant with the mass scale. The purpose of this exercise is to see whether the smearing can change the multi-Z' resonant structure qualitatively and, at the same time, whether the dip before such a peaking structure could be washed out or not. The crossing point where the differential cross section in the di-electron invariant mass intersects the SM background expectation, i.e. after the dip and before the peak(s), is taken as the effective mass to compute the Gaussian width. Anyway, the result is not very sensitive to the precise choice of the mass scale. The effect of the smearing on the (quasi) degenerate scenario represented by the benchmark point H is displayed in Fig. 5.9(b). The statistical error, evaluated for an integrated luminosity $\mathcal{L} = 30$ fb^{-1}, is included in the blue band. During the low luminosity run, the dip will not be statistically significant. However, the "bump" could be detected.

Next, consider the benchmark point F in Tab. 5.2, with the $Z'_{2,3}$ width fixed at $\Gamma_{Z'_{2,3}}/M_{Z'_{2,3}} = 1\%$. Oppositely to the case shown in Fig. 5.7(a), where the same benchmark F was pictures but with $\Gamma_{Z'_{2,3}}/M_{Z'_{2,3}} = 5\%$, now the two resonances are a priori clearly visible as displayed in Fig. 5.9(c). The distance between the two peaks, $d \simeq 75$ GeV, is in fact bigger than the natural width. However, when applying the smearing, the double resonant peaking structure of the signal is washed out, as shown in Fig. 5.9(d). In a realistic setup, this scenario is effectively brought back to the single resonant case. This circumstance happens for all the points in the parameter space where the distance between the two peaks is smaller than about three times the Gaussian width.

The parameter space of the model is large enough to find distribution profiles where the detector smearing is not sufficient to wash away the double resonant structure. This happens especially for points characterised by large f and small g_ρ values. An example is given in Figs. 5.9(e) and 5.9(f) which correspond to the benchmark G in Tab. 5.2. What is remarkable though, for both benchmarks F and G, is that the dip is substantially unaffected by the detector smearing, no matter whether the Z'_2 and Z'_3 peaks are resolved or otherwise.

Up to now, the smearing has been applied to the di-electron channel, whose mass resolution is $R_e \simeq 0.012 M_{ee}$. The resolution is a key ingredient in detecting a 4DCHM signal, especially because the peaking structure can be quite complicated and compressed. As already mentioned the muon channel is characterised by a resolution which is roughly 8 times the electron one at large mass scales: $R_\mu \simeq 0.09 M_{\mu\mu}$ for invariant masses above 2 TeV. Oppositely to the electron channel, where R_e is almost constant with the mass range, the resolution R_μ increases with $M_{\mu\mu}$. For the considered spectrum, the situation then drastically changes compared to the electron case.

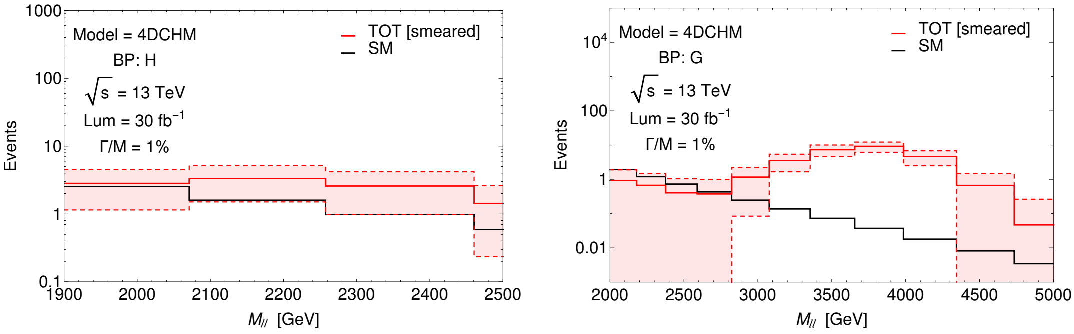

(a) (b)

FIGURE 5.10: (a) Differential cross section in the di-muon invariant mass after the smearing due to detector resolution for the benchmark point H in Tab. 5.2 at the LHC Run-II at 13 TeV energy. The width of the Gaussian is fixed at w = 191 GeV. The statistical error included in the blue error bands is evaluated for an integrated luminosity $\mathcal{L} = 30$ fb^{-1}. (b) same as (a) for benchmark G. In this case, the width of the Gaussian is fixed at w = 283 GeV.

In Fig. 5.10 is plotted the result of the smearing for the muon channel on the benchmark points H and G. As visible, owing to the larger resolution, the signal for benchmark H in Fig. 5.10(a) is completely washed out. The wider resolution merges in fact dip and peak, averaging over them. The global number of events thus lays, evenly spread over the SM background, with no defined shape. As the depletion of events in the dip region, compared to the SM background, compensates for the excess of events under the resonant peak, the net result is not statistically distinguishable from a fluctuation of SM background. For the benchmark point G, in Fig. 5.10(b), the muon channel cannot disentangle the double resonant structure. The signal would appear as an effective single broad “bump”. Again, this is due to the worse resolution in the invariant mass of the muon pairs, as compared to the electron ones. The final message here is that for characterizing the 4DCHM signal shape, the muon channel is not efficient as it does not allow to resolve resonances and dips adequately.

Also, in the interpretation of the data analysis results, a word of caution should be spent. In this situation, a signal is observed in the electron channel without its counterpart in the muon channel. The interpretation of a signal of non-universality of the couplings between the different families would be misleading, as in this case the effect is driven by a complicated peaking structure of the observed signal. This will be revealed in a successive run at higher luminosity, where the signal shape could be more likely fully reconstructed.

In both Figs. 5.9 and 5.10, the statistical error expected at the ongoing LHC Run-II with 13 TeV energy is shown. The statistical analysis shows that when the collected luminosity will be $\mathcal{L} = 30$ fb^{-1}, the LHC would acquire sensitivity to all these benchmarks. In order to have a complete projection of discovery or exclusion potential at the ongoing

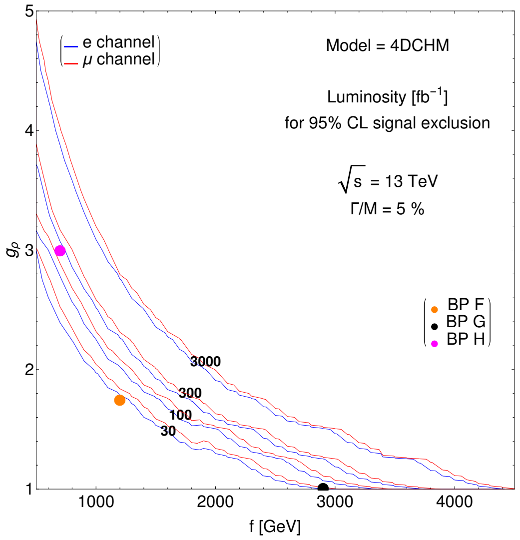

(a)

FIGURE 5.11: Projected 95% CL exclusion limits at the LHC Run-II with 13 TeV energy for different values of the integrated luminosity. The blue(red) contours refer to the electron (muon) channel. The dots represent the three benchmark points in Tab. 5.2.

LHC Run-II with 13 TeV energy, in Fig. 5.11 the exclusion limits is shown as contour plots in the parameter space defined by (g_ρ, f) for different values of the integrated luminosity, ranging from $\mathcal{L} = 30$ fb^{-1} to $\mathcal{L} = 3$ ab^{-1}. The same acceptance-times-efficiency factor for electrons and muons as for the past LHC RunI at 7, 8 TeV is here assumed to hold also at the 13 TeV Run-II. Also, mass scale dependent NNLO QCD corrections have been included.

Contrary to the ED case discussed before, the CHMs need an experimental analysis based on a modified approach. The present experimental setup is indeed designed for single (or effectively single) Z's, and it would not be efficient in the limit setting procedure in presence of multi-Z's. The key variable is the distance between the two expected peaks. If the distance is bigger than the invariant mass range selected to normalize the SM background to the data, the default procedure could be applied twice and the results of the two likelihood fits could be combined. If the two resonances are rather separated but both lie within this mass interval, the standard likelihood function would interpret one of them as SM background, thus biasing the fitting procedure. A modified signal shape could then be inserted in the likelihood function in order to optimize the search for multi-Z'-bosons. A novel and dedicated analysis is advisable for general CHMs. Moreover, the dip before the peaks could become detectable as a (negative) deviation from the SM predictions for points in the parameter space similar to the F and G configurations shown in Fig. 5.9. Again, an adequate statistical analysis would be necessary in order to classify this depletion of events happening before the "bump(s)" as evidence of a (rather

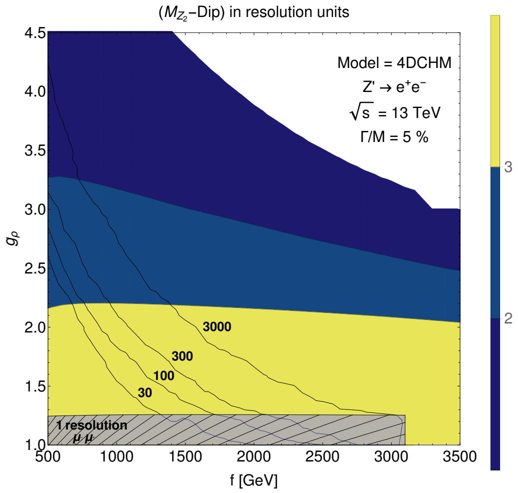

(a)

Figure 5.12: Separation between dip and first resonant peak of the 4DCHM in mass resolution units for the electron channel. From top to bottom, the coloured areas represent regions in the parameter space with increasing separation. The resonance width over mass ratio is assumed to be 5%. The labelled black contours indicate the luminosity needed to discard the SM background hypothesis at the 95% CL. The light grey shaded area in the bottom represents the region where the separation between the dip and the Z'_2 peak match one resolution unit in the muon channel.

complicated) signal, as opposed to a (downward) background fluctuation. This is the topic discussed in the next subsection.

5.3.1.4 Multi-Z' 4DCHM: profiling the new resonances

In the lucky event of a discovery in the usual "bump" hunt, the next question to be addressed would be the theoretical interpretation of the found resonance(s). In a successive run at higher integrated luminosities, one should then exploit all features of the observed events in the attempt to reach as a complete as possible reconstruction of the signal shape. A striking characteristic of multi-resonant models is the appearance of a sizeable depletion of events, compared to the SM background expectation, in the invariant mass region before the peaking structure. As done for NUED models in Sect. 5.2.1, also within the 4DCHM one should thus figure out in which region of the parameter space it is possible to successfully implement an optimised strategy, able to properly account for both the excess and depletion of events in order to reveal the presence of resonances likely induced by a CHM.

For instance, one could define the following variable:

$$\epsilon = \frac{M_{Z'_2} - M_{\rm dip}}{M_{Z'_2}}, \tag{5.5}$$

where M_{dip} is the value of the di-lepton invariant mass corresponding to the minimum of the dip. The variable ϵ would quantify the relative distance between the (degenerate or otherwise) peaks, exemplified by the position of $M_{Z'_2}$, and the dip (or inverse peak). The role of ϵ is to discriminate a depletion from an excess of events. If this variable is smaller than the detector resolution, it would not be possible to disentangle the negative contribution of the interference from the excess on the peak(s). Under these circumstances, no experimental measurement would be able to underpin the CHM nature of the discovered resonance(s). In Fig. 5.12 is shown the contour plot representing the condition $\epsilon = c \times R_e$, with R_e the di-electron invariant mass resolution and c a coefficient whose value can be read from the colour legend on the right hand side of the plot. The coloured parts of the parameter space represent the regions where $\epsilon \geq c \times R_e$. The entire coloured region collapses to a narrow stripe, sitting at very low values of g_ρ, for the muon channel as the di-muon invariant mass resolution is much larger than the electron one.

The electron DY channel is thus particularly useful for profiling the discovered resonance(s), oppositely to the muon channel which is favoured for the actual search. For values of the CHM free parameters where $\epsilon \geq R_e$, there is indeed the possibility of observing the peak(s) at some large di-electron invariant mass, simultaneously accompanied by a depletion of the SM background events expected at lower invariant mass values. This depletion should not be interpreted as a statistical fluctuation, nor as a negative correction (e.g., induced by large Sudakov logarithms ensuing from EW loop effects), rather it should be taken as an additional signal manifestation that a suitable statistical analysis would aim at extracting as such.

Finally, following again the suggestion given in Ref. [1], the possibility of using the Forward-Backward Asymmetry to profile the resonances within this Composite Higgs scenario has been explored. Unfortunately, as for the NUED(s) model, the statistical significance of the A_{FB} distribution in the di-lepton invariant mass is sub-dominant with respect to the invariant mass peak evidence in all the explored parameter space of the model.

5.4 Searches and diagnostics of a multi-Z' signal

In this Chapter it has been analysed the phenomenology of the NUED and 4DCHM which are representative of two generic classes of multi-Z' scenarios, weakly and strongly interacting respectively. The consequences of both FW and interference effects on the signal shape and rate have been examined.

Both contributions manifest themselves through a peculiar interplay which generically produces a large dip (almost an inverted peak, significantly deeper than those seen in the case of narrow single Z'-boson scenarios) in the di-lepton invariant mass spectrum that precedes the appearance of either a single degenerate peak (always for the NUED scenario and over certain combinations of the 4DCHM parameters) or a double resonant peaking structure (in the complementary parts of the 4DCHM parameter space). In the NUED case, such a dip appears in a mass region which is always resolvable from the peak one, for standard detector resolutions in the di-lepton invariant mass. In contrast, for the 4DCHM, also the opposite situation can occur, when the dip and the peak interplay over the mass interval where a possible signal is sampled.

Current statistical approaches implemented by the LHC collaborations do not allow one to model the signal as a composition of a dipping and peaking structure, so the analysis has focused on describing the phenomenology emerging from treating the dip and the peak(s) separately. As the latter normally emerge(s) before the former as luminosity accrues, once can use the kinematic features related to the dip region as a characterising element of a possible discovery following the extraction of the peak(s), with a twofold purpose. On the one hand, when the multiple Z' peaks (two generally, in fact) merge into one (which can happen in both the NUED and 4DCHM scenarios), to make evident that the underlying BSM structure is not the standard single-Z' one. On the other hand, when the two peaks are separable (as it can happen in the 4DCHM), to help one profiling the multiple Z'-boson signal in terms of masses, widths and quantum numbers of the new discovered resonances.

Further challenges arise in some regions of the 4DCHM parameter space, where the predicted spectrum of multiple resonances is compressed. In this scenario generally the dip that is caused by the interference between the new resonance(s) and the SM photon and Z-boson could appear in the close proximity of the first resonance, thus affecting the expected BW shape of the signal. In this circumstances, the peaking structure of the spectrum can be difficult to observe, rendering the analysis challenging because of the detector resolution and other factors.

For instance, the presence of a dip in the close proximity of the first resonance could affect the normalization of the SM background, which is presently done in a selected invariant mass window around the hypothetical pole mass of the new vector boson(s). Concerning the issue with the specific channel resolutions, it has been shown that in the electron channel, it would be likely that the multi-resonant structure could be detected, as the resolution is about $R_e \simeq 1.2\%$ and is almost constant over the mass scale. In fact it has been shown that the distance between different peaks and between peaks and dip is larger than R_e over a substantial part of the parameter space. In the muon channel, such a complicated structure would be completely obscured by the much worse resolution ($R_\mu \simeq 9\%$ for $M_{\mu\mu} \geq 3$ TeV). Summarizing, in the particular instance of this type of signal, both electrons and muons are useful for direct Z'-boson searches but, in profiling the resonance(s), the electron channel would be better being characterized by a much smaller mass resolution.

Chapter 6

Conclusions

A detailed analysis of the phenomenology of BSM heavy neutral resonances and their experimental searches in the two leptons final state was presented in this work. Theoretically motivated BSM constructions have been considered as benchmark for probing the sensitivity of the analysis in realistic scenarios.

The case of a single resonant signal represents the optimal situation from the experimental point of view since the dedicated analysis are designed to maximise their sensitivity on this kind of objects. The signal would appear as a bump in the invariant mass distribution and it would be fitted using a BW functional form. The analysis for the detection of narrow resonances follows a model independent approach, adopting either the "optimal cut" or the NWA, such that the experimental exclusions, derived from the absence of a signal, are easy to reinterpret for any narrow Z' realisation. The results showed in the first part of Chapter 2, obtained following closely the described procedures, match the experimental bounds of the time of Ref. [11]. Furthermore the projections on the sensitivity of the LHC at future luminosities are in perfect agreement with the more recent mass limits released by the CMS [36] and ATLAS [37] collaborations.

The aforementioned procedure, however is not valid if the width of the resonance is large. In this context model dependent effects, like the size of the contribution from the interference, are more important and it is not possible to define a simple functional form for the signal shape. The experimental sensitivity drops considerably together with the number of di-lepton events. There are indeed many theoretical constructions that lead to an enhancement of the Z' width, like the case where extra BSM decay channels are opened to the Z' boson, or when a mixing in the neutral gauge sector occurs, to name a few. This scenario has been described by keeping the fermions' couplings fixed, thus leaving the di-lepton production cross section unchanged, while scaling fixing by hand the width of the Z' BW.

Already for resonances with $\Gamma_{Z'}/M_{Z'}$ ¿ 5% the information that can be extracted from the invariant mass distribution is limited. The introduction of other observables can improve the overall sensitivity and they can also provide additional informations. In the second part of Chapter 2, the A^{*}_{FB} observable has been introduced. This observable depends on a different combination of the fermions' chiral couplings with respect to the cross section, and its shape is much less sensible to variation of the intrinsic Z' width. It has been shown that in the context of wide resonances the A^{*}_{FB} can be a successful search tool to disentangle the presence of new physics. Another good feature of the A^{*}_{FB} is that being defined as a ratio of cross sections, part of the systematic uncertainties are cancelled, as it happens for the PDF error.

The uncertainty coming from the PDF is discussed in details for all the observable discussed in this work. This is because some concerns have been raised by the predictions for the high invariant mass di-lepton spectrum and its PDF uncertainty obtained using some recently released QED PDF sets. The situation with the QED PDFs and the effects of PI processes in the di-lepton channel are examined in Chapter 3. It has been shown that QED sets can be used to extract the distributions of the photon from inside the nucleon, as simply as for any other parton. The photons extracted from QED PDFs are real, and it is possible to calculate the effect of PI processes on the di-lepton spectrum. This SM contribution shall be included in the analysis as the precise determination of the background predictions is a key point of any BSM search. In particular, the uncertainties coming along the photon PDFs can decrease the sensitivity, especially for non-resonant objects. In this picture the A^{*}_{FB} would still provide a clean and reliable observable even in case of large PDF uncertainties.

Moving across the Run-II era and towards the HL-LHC stage, the increasing accumulated luminosity would allow more refined analysis for the detection and the interpretation of wide resonance signals. In Chapter 4 a new observable has been introduced to serve these purposes. In particular the experimental fit of a BSM signal depends on two free parameters for the BW functional form, which are the mass and the width of the resonance, and the determination of the latter in particular represents a non trivial experimental challenge. In order to improve the quality of the fit, other independent observables can be imported in the analysis. The A^{*}_{FB} do not provide much information on the resonance width. The leptons' transverse momentum (p_T) spectrum instead can be used in this sense. A Focus Point appears as a consequence of the normalisation procedure of the lepton's p_T distributions. The position of the FP being model independent, and width independent, can be used to define a new observable: the Asymmetry of the Focus Point (A_{FP}) The latter can be used either to set independent constrain on the width of a Z' boson, if the models is assumed, or give indication on the class of models the Z' belongs, if its intrinsic width is assumed. In a high luminosity diagnostic stage of a BSM signal, this observable can improve the sensitivity of the experimental analysis, especially to broad resonances.

Another possible scenario where the simple “bump” searches show weaknesses is in the presence of a spectrum with multiple Z's. The di-lepton invariant mass distribution will depart from the simple BW shape due to the interference and FW effects, which get dramatically amplified when the spectrum is compressed. The multi-Z' phenomenology is discussed in Chapter 5, where two main benchmarks have been considered for this purpose: the 4-Dimensional Composite Higgs Model (4DCHM), and the Non-Universal Extra Dimensions (NUED) model. The latter represents the framework where to study degenerate resonances, as the Z' bosons represented by the first KK excitation of the photon and of the Z boson naturally appear with very close masses. In the NUED model, the interference effects are enhanced and the overall profile of the di-lepton invariant mass distribution appear as a broad, but still peaked, resonance. It has been verified that the experimental methods that are applied for narrow single resonances are still valid in this context. The interference effects that might spoil the analysis, dominate in a region that is far away from the peak, such that they do not play a role in the integration region defined by the “optimal cut”, and as well the net result do not deviate sensibly from the outcome of the NWA. The 4DCHM environment instead is larger, as there are two main parameter that define the phenomenology of the model, which are the composite scale and the strength of the gauge coupling. The different configurations of the model and the phenomenological situations that can be realised in its context, have been considered varying these two parameters. Both narrow and wide resonance realisations are allowed in this model, as it predicts also exotic fermions that can couple to the Z'. The mutual interference effects between the various Z's, and the compressed spectrum that arises in some regions of the parameter space, lead to a very model dependent signal shape. In this context the usual model independent analysis for the singly resonant case are not valid any more. A model dependent analysis is required, which also distinguish between the signal in the di-electron and di-muon channels, since their different experimental resolution in the invariant mass distribution would lead to peculiar observations.

In conclusion, a general study of BSM searches in the di-lepton channel has been presented in this work. A large variety of phenomenological situations have been studied, spanning from the simplest singly narrow resonant case to more complex non-minimal BSM constructions, with the purpose of offering an exhaustive picture of the origin of possible deviations from the SM expectations that might be detected during the LHC Run-II and in the following HL-LHC stage. The adopted experimental procedure have been tested in the various BSM models, revealing weaknesses in some corners of their parameter space. In the attempt of addressing these possible flaws, other observables have been included in the analysis, the well known A_{FB} and the novel A_{FP}. The discovery and diagnostic potential of the two has been extensively discussed, together with a detailed analysis of their statistical and PDF uncertainties.

Appendix A

Single Z' models parametrisation

The symmetry breaking patterns and the charges and couplings assignments for the single-Z' classes of models are given below. The following passages follow closely the description given in Ref. [28].

A.1 E_6 models

This class of models assumes that E_6 is the fundamental gauge group at the GUT scale. The symmetry breaking pattern described below occurs at the GUT scale.

$$E_6 \rightarrow SO(10) \times U(1)_\psi$$

$$SO(10) \rightarrow SU(5) \times U(1)_\chi$$

$$SU(5) \rightarrow SU(3)_C \times SU(2)_L \times U(1)_Y$$

What is left is the usual SM gauge group, which has its own symmetry breaking and mixing of the gauge fields, leaving only the $SU(3)_C$ and the $U(1)_{em}$ unbroken, as described by the Higgs mechanism. The two Abelian gauge groups $U(1)_\psi$ and $U(1)_\chi$ and the respective generators T_ψ and T_χ might remain unbroken until the TeV scale. In general it is possible that a linear combination of those fields survives down to the TeV scale:

$$U(1)' = U(1)_\chi \cos\theta + U(1)_\psi \sin\theta \tag{A.1}$$

meaning that the unbroken E_6 generator can be written as:

$$Q_{E_6} = T_\chi \cos\theta + T_\psi \sin\theta \tag{A.2}$$

The gauge coupling g' of the resulting $U(1)'$ is generally assumed to be equal to the GUT normalised $U(1)_Y$ gauge coupling of the SM, $g' = (e/\cos\theta_W)\sqrt{5/3} \approx 0.462$.

A.2 Generalised Left-Right Symmetric models - GLR

This class of models is based on the left-right (LR) symmetry extension of the SM. The symmetry breaking pattern is:

$$SU(2)_L \times SU(2)_R \times U(1)_{B-L} \to SU(2)_L \times U(1)_Y$$

In particular, with respect to the neutral sector the interesting symmetry breaking occurs mixing the $U(1)$ groups:

$$U(1)_R \times U(1)_{B-L} \to U(1)_Y$$

where the $U(1)_R$ is associated to the third neutral component $SU(2)_R$ and its generator T_{3R}. Models where the Z' comes from either the $U(1)_R$ or the $U(1)_{B-L}$ are widely discussed in the literature. The generalisation to these constructions is built considering a general linear combination of the generators:

$$Q_{GLR} = T_{3R} \cos\phi + T_{B-L} \sin\phi \tag{A.3}$$

In order to match the couplings of the popular LR symmetric model, the gauge coupling g' is fixed at $g' = 0.595$.

A.3 Generalised Sequential Models - GSM

This group of models has been built in order to include the popular Sequential Standard Model (SSM) which is defined to have a Z' with the same couplings as the SM Z boson. The generalisation of this idea predicts the Z' to arise from a linear combination of the T_{3L} generator and the charge generator Q.

$$Q_{GSM} = T_{3L} \cos\alpha + Q \sin\alpha \tag{A.4}$$

In order to correctly match the couplings of the SSM, the gauge coupling g' is fixed at $g' = 0.76$.

A.4 Summary of couplings and natural widths

The specific values for the choice of the mixing angles, and the consequent chiral couplings between the Z' and the fermions are given in the table A.1 for all the single Z' models within the three classes discussed above.

Assuming that the Z'-bosons do not have any other decay channel different from SM matter, than to each model is associated a specific value for the resonance width, that will be referred as the natural width of the model. The natural widths of the benchmark models considered in this work are available is Tab. A.2.

$U(1)'$	$Parameter$	a_V^u	a_A^u	a_V^d	a_A^d	a_V^e	a_A^e	a_V^ν	a_A^ν
$E6(g'=0.462)$	θ								
χ	0	0	-0.316	-0.632	0.316	0.632	0.316	0.474	0.474
ψ	0.5π	0	0.408	0	0.408	0	0.408	0.204	0.204
η	-0.29π	0	-0.516	-0.388	-0.129	0.388	-0.129	0.129	0.129
S	0.129π	0	-0.130	-0.581	0.452	0.581	0.452	0.516	0.516
I	0.21π	0	0	-0.5	0.5	0.5	0.5	0.5	0.5
N	0.42π	0	0.317	-0.157	0.474	0.157	0.474	0.316	0.316
$GLR(g'=0.592)$	ϕ								
R	0	0.5	-0.5	-0.5	0.5	-0.5	0.5	0	0
$B-L$	0.5π	0.333	0	0.333	0	-1	0	-0.5	-0.5
LR	-0.130π	0.326	-0.459	-0.591	0.459	-0.06	0.459	0.199	0.199
Y	0.25π	0.589	-0.354	-0.118	0.354	-1.061	0.354	-0.354	-0.354
$GSM(g'=0.762)$	α								
SM	-0.072π	0.186	0.487	-0.336	-0.487	-0.035	-0.487	0.487	0.487
$T3L$	0	0.5	0.5	-0.5	-0.5	-0.5	-0.5	0.5	0.5
Q	0.5π	1.333	0	-0.667	0	-2	0	0	0

TABLE A.1: Table with the specific values for the mixing angles identifying the single Z' benchmark models. The corresponding values for Z' vector and axial couplings to fermions are given explicitly.

Model	$\Gamma_{Z'}/M_{Z'}$ [%]
E_6^{χ}	1.16
E_6^{ϕ}	0.53
E_6^{η}	0.64
E_6^{S}	1.17
E_6^{I}	1.06
E_6^{N}	0.54
$GLR-R$	2.44
$GLR-B-L$	1.51
$GLR-LR$	2.04
$GLR-Y$	2.33
$GSM-SSM$	2.98
$GSM-T_{3L}$	4.62
$GSM-Q$	12.32

TABLE A.2: Natural widths for the single Z'-boson benchmark models.

Appendix B

Light fermions couplings in the 4DCHM

The explicit expressions of the ρ couplings to light fermions in the 4DCHM are given here.

The couplings of the neutral gauge bosons to the light SM fermions can be expressed by the following Lagrangian

$$\mathcal{L} \supset \sum_f \left[e\bar{\psi}^f \gamma_\mu Q^f \psi^f A^\mu + \sum_{i=0}^{5} (\bar{\psi}^f_L g^L_{Z'_i}(f) \gamma_\mu \psi^f_L + \bar{\psi}^f_R g^R_{Z'_i}(f) \gamma_\mu \psi^f_R) Z'^{\mu}_i \right] \tag{B.1}$$

where $\psi_{L,R} = [(1 \pm \gamma_5)/2]\psi$ and where Z'_0 and A corresponds to the neutral SM gauge bosons Z and γ. The photon field is coupled to the electromagnetic current in the standard way with the electric charge which is defined as

$$e = \frac{g_L g_Y}{\sqrt{g_L^2 + g_Y^2}}, \qquad g_L = g_0 c_\theta, \qquad g_Y = g_{0Y} c_\psi, \qquad tg_\theta = \frac{g_0}{g_\rho}, \qquad tg_\psi = \frac{\sqrt{2} g_{0Y}}{g_\rho}. \tag{B.2}$$

The $g^{L,R}_{Z'_i}$ couplings have the following expression

$$g^L_{Z'_i}(f) = A_{Z'_i} T^3_L(f) + B_{Z'_i} Q^f, \qquad g^R_{Z'_i}(f) = B_{Z'_i} Q^f, \tag{B.3}$$

where, at the leading order in the expansion parameter $\xi = v^2/f^2$, $A_{Z'_i}$ and $B_{Z'_i}$ read

$$
\begin{aligned}
&A_Z \simeq \frac{e}{s_\omega c_\omega}\big[1 + (c_\omega^2 a_Z + s_\omega^2 b_Z)\xi\big], && B_Z \simeq -e\frac{s_\omega}{c_\omega}(1 + b_Z\xi),\\
&A_{Z'_1} = 0, && B_{Z'_1} = 0,\\
&A_{Z'_2} \simeq -\frac{e}{c_\omega}\frac{s_\psi}{c_\psi}\Big[1 + (\frac{c_\omega}{s_\omega}a_{Z'_2} - b_{Z'_2})\xi\Big], && B'_{Z'_2} \simeq \frac{e}{c_\omega}\frac{s_\psi}{c_\psi}\Big[1 - b_{Z'_2}\xi\Big],\\
&A_{Z'_3} \simeq -\frac{e}{s_\omega}\frac{s_\theta}{c_\theta}\big[1 + (a_{Z'_3} + \frac{s_\omega}{c_\omega}b_{Z'_3})\xi\big], && B_{Z'_3} \simeq \frac{e}{c_\omega}\frac{s_\theta}{c_\theta}b_{Z'_3}\xi,\\
&A_{Z'_4} = 0, && B_{Z'_4} = 0,\\
&A_{Z'_5} \simeq e(\frac{1}{s_\omega}a_{Z'_5} - \frac{1}{c_\omega}b_{Z'_5})\sqrt{\xi}, && B_{Z'_5} \simeq \frac{e}{c_\omega}b_{Z'_5}\sqrt{\xi},
\end{aligned}
\tag{B.4}
$$

with

$$
\tan\omega = \frac{g_Y}{g_L}, \qquad e = g_L s_\omega = g_Y c_\omega, \qquad \frac{e}{s_\omega c_\omega} = \sqrt{g_L^2 + g_Y^2}, \tag{B.5}
$$

and

$$
\begin{aligned}
&a_Z = (2s_\theta^2 + s_\psi^2)(4c_\theta^2 - 1)/32, && b_Z = (2s_\theta^2 + s_\psi^2)(4c_\psi^2 - 1)/32,\\
&a_{Z'_2} = \frac{\sqrt{2}s_\theta s_\psi c_\psi^6}{4(c_\psi^2 - c_\theta^2)(2c_\psi^2 - 1)}, && b_{Z'_2} = \frac{c_\psi^4(2 - 7c_\psi^2 + 9c_\psi^4 - 4c_\psi^6)}{8s_\psi^2(1 - 2c_\psi^2)^2},\\
&a_{Z'_3} = \frac{-2c_\theta^4 + 5c_\theta^6 - 4c_\theta^8}{4(1 - 2c_\theta^2)^2}, && b_{Z'_3} = \frac{\sqrt{2}s_\theta s_\psi c_\theta^6}{4(2c_\theta^2 - 1)(c_\theta^2 - c_\psi^2)},\\
&a_{Z'_5} = \frac{s_\theta}{2\sqrt{2}(1 - 2c_\theta^2)}, && b_{Z'_5} = -\frac{s_\psi}{4(1 - 2c_\psi^2)}.
\end{aligned}
\tag{B.6}
$$

Bibliography

[1] Elena Accomando, Alexander Belyaev, Juri Fiaschi, Ken Mimasu, Stefano Moretti, and Claire Shepherd-Themistocleous. Forward-backward asymmetry as a discovery tool for Z bosons at the LHC. *JHEP*, 01:127, 2016.

[2] Elena Accomando, Daniele Barducci, Stefania De Curtis, Juri Fiaschi, Stefano Moretti, and Claire H. Shepherd-Themistocleous. Drell-Yan production of multi Z-bosons at the LHC within Non-Universal ED and 4D Composite Higgs Models. *JHEP*, 07:068, 2016.

[3] Elena Accomando, Juri Fiaschi, Francesco Hautmann, Stefano Moretti, and Claire H. Shepherd-Themistocleous. Photon-initiated production of a dilepton final state at the LHC: Cross section versus forward-backward asymmetry studies. *Phys. Rev.*, D95(3):035014, 2017.

[4] Elena Accomando, Juri Fiaschi, Francesco Hautmann, Stefano Moretti, and Claire H. Shepherd-Themistocleous. The effect of real and virtual photons in the di-lepton channel at the LHC. *Phys. Lett.*, B770:1–7, 2017.

[5] Paul Langacker. The Physics of Heavy Z' Gauge Bosons. *Rev. Mod. Phys.*, 81: 1199–1228, 2009.

[6] Nima Arkani-Hamed, Savas Dimopoulos, and G. R. Dvali. The Hierarchy problem and new dimensions at a millimeter. *Phys. Lett.*, B429:263–272, 1998.

[7] Ignatios Antoniadis, Nima Arkani-Hamed, Savas Dimopoulos, and G. R. Dvali. New dimensions at a millimeter to a Fermi and superstrings at a TeV. *Phys. Lett.*, B436:257–263, 1998.

[8] David B. Kaplan and Howard Georgi. SU(2) x U(1) Breaking by Vacuum Misalignment. *Phys. Lett.*, 136B:183–186, 1984.

[9] Kaustubh Agashe, Roberto Contino, and Alex Pomarol. The Minimal composite Higgs model. *Nucl. Phys.*, B719:165–187, 2005.

[10] Stefania De Curtis, Michele Redi, and Andrea Tesi. The 4D Composite Higgs. *JHEP*, 04:042, 2012.

[11] Vardan Khachatryan et al. Search for physics beyond the standard model in dilepton mass spectra in proton-proton collisions at $\sqrt{s} = 8$ TeV. *JHEP*, 04:025, 2015.

[12] Vardan Khachatryan et al. Forward-backward asymmetry of Drell-Yan lepton pairs in pp collisions at $\sqrt{s} = 8$ TeV. *Eur. Phys. J.*, C76(6):325, 2016.

[13] Elena Accomando, Diego Becciolini, Alexander Belyaev, Stefano Moretti, and Claire Shepherd-Themistocleous. Z' at the LHC: Interference and Finite Width Effects in Drell-Yan. *JHEP*, 10:153, 2013.

[14] Elena Accomando, Diego Becciolini, Alexander Belyaev, Stefania De Curtis, Daniele Dominici, Steve F. King, Stefano Moretti, and Claire Shepherd-Themistocleous. W' and Z' searches at the LHC. *PoS*, DIS2013:125, 2013.

[15] Jay Orear. Notes on statistics for physicists, revised. *SLAC book*, 1982.

[16] Glen Cowan. Statistics for Searches at the LHC. In *Proceedings, 69th Scottish Universities Summer School in Physics : LHC Phenomenology (SUSSP69): St.Andrews, Scotland, August 19-September 1, 2012*, pages 321–355, 2013.

[17] Vardan Khachatryan et al. Search for narrow resonances in dilepton mass spectra in proton-proton collisions at $\sqrt{s} = 13$ TeV and combination with 8 TeV data. *Phys. Lett.*, B768:57–80, 2017.

[18] Ye Li and Frank Petriello. Combining QCD and electroweak corrections to dilepton production in FEWZ. *Phys. Rev.*, D86:094034, 2012.

[19] R. Hamberg, W. L. van Neerven, and T. Matsuura. A complete calculation of the order $\alpha - s^2$ correction to the Drell-Yan K factor. *Nucl. Phys.*, B359:343–405, 1991. [Erratum: Nucl. Phys.B644,403(2002)].

[20] Robert V. Harlander and William B. Kilgore. Next-to-next-to-leading order Higgs production at hadron colliders. *Phys. Rev. Lett.*, 88:201801, 2002.

[21] Juri Fiaschi, Elena Accomando, Alexander Belyaev, Ken Mimasu, Stefano Moretti, and Claire H. Shepherd-Themistocleous. Complementarity of Forward-Backward Asymmetry for discovery of Z' bosons at the Large Hadron Collider. *PoS*, EPS-HEP2015:176, 2015.

[22] Elena Accomando. Forward-Backward Asymmetry as a Discovery Tool for Z' Bosons at the LHC. *PoS*, DIS2015:097, 2015.

[23] Elena Accomando, Alexander Belyaev, Juri Fiaschi, Ken Mimasu, Stefano Moretti, and Claire Shepherd-Themistocleous. A_{FB} as a discovery tool for Z' bosons at the LHC. *Nuovo Cim.*, C38(4):153, 2016.

[24] Elena Accomando, Juri Fiaschi, Francesco Hautmann, Stefano Moretti, and Claire Shepherd-Themistocleous. Impact of the Photon-Initiated process on Z'-boson searches in di-lepton final states at the LHC. 2016.

[25] Elena Accomando, Juri Fiaschi, Francesco Hautmann, Stefano Moretti, and Claire H. Shepherd-Themistocleous. Real and virtual photons effects in di-lepton production at the LHC. In *21st Rencontres de Physique de La Valle d'Aoste: Rencontres de La Thuile (La Thuile) La Thuile, Aosta , Italy, March 5-11, 2017*, 2017.

[26] Elena Accomando, Juri Fiaschi, Stefano Moretti, and Claire H. Shepherd-Themistocleous. Constraining Z' widths from p_T measurements in Drell-Yan processes. 2017.

[27] Elena Accomando, Daniele Barducci, Stefania De Curtis, Juri Fiaschi, Stefano Moretti, and Claire Shepherd-Themistocleous. Exclusion and discovery via Drell-Yan in the 4DCHM. *PoS*, DIS2015:105, 2015.

[28] Elena Accomando, Alexander Belyaev, Luca Fedeli, Stephen F. King, and Claire Shepherd-Themistocleous. Z' physics with early LHC data. *Phys. Rev.*, D83: 075012, 2011.

[29] S. Schael et al. Precision electroweak measurements on the Z resonance. *Phys. Rept.*, 427:257–454, 2006.

[30] G. Altarelli. The Standard electroweak theory and its experimental tests. *Lect. Notes Phys.*, 426:323–382, 1994.

[31] Ennio Salvioni, Giovanni Villadoro, and Fabio Zwirner. Minimal Z-prime models: Present bounds and early LHC reach. *JHEP*, 11:068, 2009.

[32] Philip Bechtle, Oliver Brein, Sven Heinemeyer, Georg Weiglein, and Karina E. Williams. HiggsBounds: Confronting Arbitrary Higgs Sectors with Exclusion Bounds from LEP and the Tevatron. *Comput. Phys. Commun.*, 181:138–167, 2010.

[33] W. L. van Neerven and E. B. Zijlstra. The $O(\alpha_s^2)$ corrected Drell-Yan K factor in the DIS and MS scheme. *Nucl. Phys.*, B382:11–62, 1992. [Erratum: Nucl. Phys.B680,513(2004)].

[34] S. Kretzer, H. L. Lai, F. I. Olness, and W. K. Tung. Cteq6 parton distributions with heavy quark mass effects. *Phys. Rev.*, D69:114005, 2004.

[35] Tomas Jezo, Michael Klasen, David R. Lamprea, Florian Lyonnet, and Ingo Schienbein. NLO+NLL limits on W' and Z' gauge boson masses in general extensions of the Standard Model. *JHEP*, 12:092, 2014.

[36] CMS Collaboration. Search for a high-mass resonance decaying into a dilepton final state in 13 fb^{-1} of pp collisions at $\sqrt{s} = 13$ TeV. CMS-PAS-EXO-16-031, 2016.

[37] The ATLAS collaboration. Search for new high-mass phenomena in the dilepton final state using 36.1 fb^{-1} of proton-proton collision data at $\sqrt{s} = 13$ TeV with the ATLAS detector. ATLAS-CONF-2017-027, 2017.

[38] Marcela Carena, Alejandro Daleo, Bogdan A. Dobrescu, and Timothy M. P. Tait. Z' gauge bosons at the Tevatron. *Phys. Rev.*, D70:093009, 2004.

[39] Frank Petriello and Seth Quackenbush. Measuring Z' couplings at the CERN LHC. *Phys. Rev.*, D77:115004, 2008.

[40] Mirjam Cvetic and Stephen Godfrey. Discovery and identification of extra gauge bosons. 1995.

[41] Paul Langacker, Richard W. Robinett, and Jonathan L. Rosner. New Heavy Gauge Bosons in p p and p anti-p Collisions. *Phys. Rev.*, D30:1470, 1984.

[42] Thomas G. Rizzo. Indirect Searches for Z-prime-like Resonances at the LHC. *JHEP*, 08:082, 2009.

[43] Michael Dittmar. Neutral current interference in the TeV region: The Experimental sensitivity at the LHC. *Phys. Rev.*, D55:161–166, 1997.

[44] Guido Altarelli, B. Mele, and M. Ruiz-Altaba. Searching for New Heavy Vector Bosons in $p\bar{p}$ Colliders. *Z. Phys.*, C45:109, 1989. [Erratum: Z. Phys.C47,676(1990)].

[45] Jens Erler and Paul Langacker. Constraints on extended neutral gauge structures. *Phys. Lett.*, B456:68–76, 1999.

[46] Yeong Gyun Kim and Kang Young Lee. Direct search for heavy gauge bosons at the LHC in the nonuniversal SU(2) model. *Phys. Rev.*, D90:117702, 2014.

[47] Ehab Malkawi and C. P. Yuan. New physics in the third family and its effect on low-energy data. *Phys. Rev.*, D61:015007, 2000.

[48] Daniel Stump, Joey Huston, Jon Pumplin, Wu-Ki Tung, H. L. Lai, Steve Kuhlmann, and J. F. Owens. Inclusive jet production, parton distributions, and the search for new physics. *JHEP*, 10:046, 2003.

[49] Sergey Alekhin et al. The PDF4LHC Working Group Interim Report. 2011.

[50] A. Accardi, L. T. Brady, W. Melnitchouk, J. F. Owens, and N. Sato. Constraints on large-x parton distributions from new weak boson production and deep-inelastic scattering data. *Phys. Rev.*, D93(11):114017, 2016.

[51] A. Accardi et al. A Critical Appraisal and Evaluation of Modern PDFs. *Eur. Phys. J.*, C76(8):471, 2016.

[52] Stefan Dittmaier and Max Huber. Radiative corrections to the neutral-current Drell-Yan process in the Standard Model and its minimal supersymmetric extension. *JHEP*, 01:060, 2010.

[53] Daniel de Florian, Germn F. R. Sborlini, and Germn Rodrigo. QED corrections to the AltarelliParisi splitting functions. *Eur. Phys. J.*, C76(5):282, 2016.

[54] Daniel de Florian, Germn F. R. Sborlini, and Germn Rodrigo. Two-loop QED corrections to the Altarelli-Parisi splitting functions. *JHEP*, 10:056, 2016.

[55] Mateusz Dyndal and Laurent Schoeffel. Four-lepton production from photon-induced reactions in pp collisions at the LHC. *Acta Phys. Polon.*, B47:1645, 2016.

[56] Mamut Ababekri, Sayipjamal Dulat, Joshua Isaacson, Carl Schmidt, and C. P. Yuan. Implication of CMS data on photon PDFs. 2016.

[57] Csaba Cski, Jay Hubisz, Salvator Lombardo, and John Terning. Gluon versus photon production of a 750 GeV diphoton resonance. *Phys. Rev.*, D93(9):095020, 2016.

[58] Sylvain Fichet, Gero von Gersdorff, and Christophe Royon. Scattering light by light at 750 GeV at the LHC. *Phys. Rev.*, D93(7):075031, 2016.

[59] L. A. Harland-Lang, V. A. Khoze, and M. G. Ryskin. Sudakov effects in photon-initiated processes. *Phys. Lett.*, B761:20–24, 2016.

[60] L. A. Harland-Lang, V. A. Khoze, and M. G. Ryskin. The photon PDF in events with rapidity gaps. *Eur. Phys. J.*, C76(5):255, 2016.

[61] L. A. Harland-Lang, V. A. Khoze, and M. G. Ryskin. The production of a diphoton resonance via photon-photon fusion. *JHEP*, 03:182, 2016.

[62] C. M. Carloni Calame, G. Montagna, O. Nicrosini, and A. Vicini. Precision electroweak calculation of the production of a high transverse-momentum lepton pair at hadron colliders. *JHEP*, 10:109, 2007.

[63] S. Alioli et al. Precision studies of observables in $pp \to W \to l\nu_l$ and $pp \to \gamma, Z \to l^+l^-$ processes at the LHC. *Eur. Phys. J.*, C77(5):280, 2017.

[64] Dimitri Bourilkov. Photon-induced Background for Dilepton Searches and Measurements in pp Collisions at 13 TeV. 2016.

[65] Dimitri Bourilkov. Exploring the LHC Landscape with Dileptons. 2016.

[66] Marta uszczak, Wolfgang Schfer, and Antoni Szczurek. Two-photon dilepton production in proton-proton collisions: two alternative approaches. *Phys. Rev.*, D93 (7):074018, 2016.

[67] Gustavo Gil da Silveira, Laurent Forthomme, Krzysztof Piotrzkowski, Wolfgang Schfer, and Antoni Szczurek. Central $^+$ production via photon-photon fusion in proton-proton collisions with proton dissociation. *JHEP*, 02:159, 2015.

[68] Marta Luszczak, Antoni Szczurek, and Christophe Royon. W^+W^- pair production in proton-proton collisions: small missing terms. *JHEP*, 02:098, 2015.

[69] Davide Pagani, Ioannis Tsinikos, and Marco Zaro. The impact of the photon PDF and electroweak corrections on $t\bar{t}$ distributions. *Eur. Phys. J.*, C76(9):479, 2016.

[70] F. Hautmann. The Total cross-section for off-shell photons at high-energies. In *High energy physics: Proceedings, 28th International Conference, ICHEP'96, Warsaw, Poland, July 25-31, 1996. Vol. 1, 2*, pages 705–708, 1996.

[71] Jochen Bartels, A. De Roeck, and H. Lotter. The Gamma* gamma* total cross-section and the BFKL pomeron at e+ e- colliders. *Phys. Lett.*, B389:742–748, 1996.

[72] S. J. Brodsky, F. Hautmann, and D. E. Soper. Probing the QCD pomeron in e+ e- collisions. *Phys. Rev. Lett.*, 78:803–806, 1997. [Erratum: Phys. Rev. Lett.79,3544(1997)].

[73] S. J. Brodsky, F. Hautmann, and D. E. Soper. Virtual photon scattering at high-energies as a probe of the short distance pomeron. *Phys. Rev.*, D56:6957–6979, 1997.

[74] F. Hautmann. Effective QCD coupling and power corrections to photon-photon scattering. *Phys. Rev. Lett.*, 80:3198–3201, 1998.

[75] Maartin Boonekamp, A. De Roeck, Christophe Royon, and Samuel Wallon. Gamma* gamma* total cross-section in the dipole picture of BFKL dynamics. *Nucl. Phys.*, B555:540–564, 1999.

[76] V. M. Budnev, I. F. Ginzburg, G. V. Meledin, and V. G. Serbo. The Two photon particle production mechanism. Physical problems. Applications. Equivalent photon approximation. *Phys. Rept.*, 15:181–281, 1975.

[77] A. D. Martin, R. G. Roberts, W. J. Stirling, and R. S. Thorne. Parton distributions incorporating QED contributions. *Eur. Phys. J.*, C39:155–161, 2005.

[78] Carl Schmidt, Jon Pumplin, Daniel Stump, and C. P. Yuan. CT14QED parton distribution functions from isolated photon production in deep inelastic scattering. *Phys. Rev.*, D93(11):114015, 2016.

[79] Richard D. Ball et al. Parton distributions for the LHC Run II. *JHEP*, 04:040, 2015.

[80] Richard D. Ball, Valerio Bertone, Stefano Carrazza, Luigi Del Debbio, Stefano Forte, Alberto Guffanti, Nathan P. Hartland, and Juan Rojo. Parton distributions with QED corrections. *Nucl. Phys.*, B877:290–320, 2013.

[81] Aneesh Manohar, Paolo Nason, Gavin P. Salam, and Giulia Zanderighi. How bright is the proton? A precise determination of the photon parton distribution function. *Phys. Rev. Lett.*, 117(24):242002, 2016.

[82] F. Giuli et al. The photon PDF from high-mass DrellYan data at the LHC. *Eur. Phys. J.*, C77(6):400, 2017.

[83] Andy Buckley, James Ferrando, Stephen Lloyd, Karl Nordstrm, Ben Page, Martin Rfenacht, Marek Schnherr, and Graeme Watt. LHAPDF6: parton density access in the LHC precision era. *Eur. Phys. J.*, C75:132, 2015.

[84] Richard D. Ball, Valerio Bertone, Francesco Cerutti, Luigi Del Debbio, Stefano Forte, Alberto Guffanti, Nathan P. Hartland, Jose I. Latorre, Juan Rojo, and Maria Ubiali. Reweighting and Unweighting of Parton Distributions and the LHC W lepton asymmetry data. *Nucl. Phys.*, B855:608–638, 2012.

[85] F. Halzen and Alan D. Martin. *Quarks and leptons: an introductory course in modern particle physics.* 1984.

[86] K. Piotrzkowski. Tagging two photon production at the CERN LHC. *Phys. Rev.*, D63:071502, 2001.

[87] Paul Kessler. Photon fluxes and the EPA. In *Two-Photon Physics at LEP and HERA - Status of Data and Models Lund, Sweden, May 26-28, 1994*, pages 183–190, 1994.

[88] Nicolas Schul. *Measurements of two-photon interactions at the LHC*. PhD thesis, Louvain U., 2011.

[89] Jon Butterworth et al. PDF4LHC recommendations for LHC Run II. *J. Phys.*, G43:023001, 2016.

[90] Jens Erler, Paul Langacker, Shoaib Munir, and Eduardo Rojas. Improved Constraints on Z-prime Bosons from Electroweak Precision Data. *JHEP*, 08:017, 2009.

[91] Pran Nath et al. The Hunt for New Physics at the Large Hadron Collider. *Nucl. Phys. Proc. Suppl.*, 200-202:185–417, 2010.

[92] Alexander Belyaev, Roshan Foadi, Mads T. Frandsen, Matti Jarvinen, Fracesco Sannino, and Alexander Pukhov. Technicolor Walks at the LHC. *Phys. Rev.*, D79: 035006, 2009.

[93] Daniele Barducci, Alexander Belyaev, Stefania De Curtis, Stefano Moretti, and Giovanni Marco Pruna. Exploring Drell-Yan signals from the 4D Composite Higgs Model at the LHC. *JHEP*, 04:152, 2013.

[94] G. Balossini, G. Montagna, C. M. Carloni Calame, M. Moretti, M. Treccani, O. Nicrosini, F. Piccinini, and A. Vicini. Electroweak & QCD corrections to Drell Yan processes. *Acta Phys. Polon.*, B39:1675, 2008.

[95] Sayipjamal Dulat, Tie-Jiun Hou, Jun Gao, Marco Guzzi, Joey Huston, Pavel Nadolsky, Jon Pumplin, Carl Schmidt, Daniel Stump, and C. P. Yuan. New parton distribution functions from a global analysis of quantum chromodynamics. *Phys. Rev.*, D93(3):033006, 2016.

[96] Ignatios Antoniadis. A Possible new dimension at a few TeV. *Phys. Lett.*, B246: 377–384, 1990.

[97] Ignatios Antoniadis and K. Benakli. Limits on extra dimensions in orbifold compactifications of superstrings. *Phys. Lett.*, B326:69–78, 1994.

[98] Ignatios Antoniadis, C. Munoz, and M. Quiros. Dynamical supersymmetry breaking with a large internal dimension. *Nucl. Phys.*, B397:515–538, 1993.

[99] Ignatios Antoniadis, K. Benakli, and M. Quiros. Production of Kaluza-Klein states at future colliders. *Phys. Lett.*, B331:313–320, 1994.

[100] Karim Benakli. Perturbative supersymmetry breaking in orbifolds with Wilson line backgrounds. *Phys. Lett.*, B386:106–114, 1996.

[101] Gideon Bella, Erez Etzion, Noam Hod, Yaron Oz, Yiftah Silver, and Mark Sutton. A Search for heavy Kaluza-Klein electroweak gauge bosons at the LHC. *JHEP*, 09:025, 2010.

[102] Elena Accomando. Bounds on KaluzaKlein states from EWPT and direct searches at the LHC. *Mod. Phys. Lett.*, A30(15):1540010, 2015.

[103] E. Accomando, Ignatios Antoniadis, and K. Benakli. Looking for TeV scale strings and extra dimensions. *Nucl. Phys.*, B579:3–16, 2000.

[104] E. E. Boos, I. P. Volobuev, M. A. Perfilov, and M. N. Smolyakov. Searches for W' and Z' in Models with Large Extra Dimensions. *Theor. Math. Phys.*, 170:90–96, 2012.

[105] Elena Accomando, Ken Mimasu, and Stefano Moretti. Uncovering quasi-degenerate Kaluza-Klein Electro-Weak gauge bosons with top asymmetries at the LHC. *JHEP*, 07:154, 2013.

[106] Christophe Grojean, Oleksii Matsedonskyi, and Giuliano Panico. Light top partners and precision physics. *JHEP*, 10:160, 2013.

[107] Georges Aad et al. Search for high-mass dilepton resonances in pp collisions at $\sqrt{s} = 8$TeV with the ATLAS detector. *Phys. Rev.*, D90(5):052005, 2014.

[108] Georges Aad et al. Search for WZ resonances in the fully leptonic channel using pp collisions at $\sqrt{s} = 8$ TeV with the ATLAS detector. *Phys. Lett.*, B737:223–243, 2014.

[109] Serguei Chatrchyan et al. Search for top-quark partners with charge 5/3 in the same-sign dilepton final state. *Phys. Rev. Lett.*, 112(17):171801, 2014.

[110] Serguei Chatrchyan et al. Inclusive search for a vector-like T quark with charge $\frac{2}{3}$ in pp collisions at $\sqrt{s} = 8$ TeV. *Phys. Lett.*, B729:149–171, 2014.

[111] CMS Collaboration. Search for Vector-Like b' Pair Production with Multilepton Final States in pp collisions at sqrt(s) = 8 TeV. 2013.

[112] CMS Collaboration. Search for top quark partners with charge 5/3 at $\sqrt{s} = 13$ TeV. 2015.

[113] Duccio Pappadopulo, Andrea Thamm, Riccardo Torre, and Andrea Wulzer. Heavy Vector Triplets: Bridging Theory and Data. *JHEP*, 09:060, 2014.

[114] J. de Blas, J. M. Lizana, and M. Perez-Victoria. Combining searches of Z' and W' bosons. *JHEP*, 01:166, 2013.

[115] F. del Aguila, J. de Blas, and M. Perez-Victoria. Electroweak Limits on General New Vector Bosons. *JHEP*, 09:033, 2010.